Modelling of a Two-Phase Thermofluidic Oscillator for Low-Grade Heat Utilisation

by

Roochi Solanki

A thesis submitted in partial fulfilment of the requirements for the degree of Doctor of Philosophy
and for the Diploma of Membership of Imperial College

Department of Chemical Engineering
Imperial College London
London SW7 2AZ, United Kingdom

To my loving parents for all their encouragement, unfaltering faith and support

Acknowledgements

I would like to acknowledge the following:

1. My supervisors Dr. Christos N. Markides and Prof. Amparo Galindo for all their guidance, support and incredible patience. I would not have got through this without them.

2. The DTA studentship (Doctoral Training Award) awarded to me by the Department of Chemical Engineering, Imperial College London, and EPSRC.

3. The lunch crew: Paul, Andrew, Mark, Charles and especially Nina for distractions and dealing with my madness.

4. My friends in the penthouse room of C610, beautiful views with amazing company.

5. The Wally Girls and Wilsonites, it has been several years since we ways and we're still going strong. Thanks for all the support.

6. Finally, my incredible hero of a sister, Neha, who I could depend on implicitly and ultimately can make me laugh like no other. I couldn't have asked for a better role model in my life.

Declaration of Originality

All the work that has been presented in this thesis is my own and all else has been reference appropriately. Parts of this thesis have been published in the following international journals; Applied Energy, and Applied Thermal Engineering, and have been indicated within the thesis.

Declaration of Originality

The copyright of this thesis rests with the author and is made available under a Creative Commons Attribution Non-Commercial No Derivatives licence. Researchers are free to copy, distribute or transmit the thesis on the condition that they attribute it, that they do not use it for commercial purposes and that they do not alter, transform or build upon it. For any reuse or redistribution, researchers must make clear to others the licence terms of this work

Publications and Conferences

Parts of this thesis have been published in the following international journals:

R. Solanki, A. Galindo and, C. N. Markides, Dynamic modelling of a two-phase thermofluidic oscillator for efficient low grade heat utilization: Effect of fluid inertia, *Applied Energy*, 89:156-163, 2012.

C. N. Markides, A. Osuolale, R. Solanki, and G. V. Stan, Nonlinear heat transfer in a two-phase thermofluidic oscillator, *Applied Energy*, 104:958-977, 2013

R. Solanki, A. Galindo and, C. N. Markides, The role of heat exchange on the behaviour of an oscillatory two-phase low-grade heat engine, *Applied Thermal Engineering*, 53:177-187, 2013.

R. Solanki, R. Mathie, A. Galindo and, C. N. Markides, Modelling of a two-phase thermofluidic oscillator for low-grade heat utilisation: Accounting for irreversible thermal losses, *Applied Energy*, 106:337-354, 2013.

C. N. Markides, R. Solanki and, A. Galindo, Working fluid selection for a two-phase thermofluidic oscillator: Effect of thermodynamic properties, *Applied Energy*, 124:167-185, 2014.

and presented at the following international conferences:

SusTEM 2010: Sustainable Thermal Energy Management Conference, Newcastle upon Tyne, UK, November 2010.

SusTEM 2011: Sustainable Thermal Energy Management International Conference in the Process Industries, Newcastle upon Tyne, UK, October 2011

Abstract

The Non-Inertive-Feedback Thermofluidic Engine (NIFTE) is a two-phase thermofluidic oscillator which, by means of persistent periodic thermal-fluid oscillations when placed across a steady temperature difference, is capable of utilising low-grade (i.e., low temperature) heat to induce a fluid motion. Innovative devices which comprise no or few moving parts and that can operate utilising low-grade heat for fluid pumping and/or pressurisation are currently under development based on the NIFTE concept to: (i) understand the fundamental principle of operation of this novel technology; (ii) construct reliable, simple models that capture the first-order dominant underlying processes that govern its operation and performance for the purpose of early-stage engineering design; and (iii) to investigate the potential of this technology in specific fluid-pumping applications. Three spatially lumped linearised models of the NIFTE are developed through the use of electrical analogies. The first model (LTP) imposes a static (i.e. steady) linear temperature profile along the surface of the heat exchangers, the second model (CTD) imposes a constant-temperature difference between the surface of the heat exchanger and the working fluid, the third model (DHX) allows the solid heat exchanger blocks to store and release heat dynamically as they interact thermally with the working fluid. Through carrying out a parametric study on the LTP model, with and without inertial effects in the liquid phase it is shown that the inclusion of inertia has a significant effect on the trends and magnitudes of key performance indicators, namely the temperature gradient along the heat exchangers, oscillation frequency and exegetic efficiency. In addition, much improved predictions of the oscillation frequency and temperature gradient are possible when using the inertive LTP model. Following from this, a parametric study on the three models, all including inertia, is used to show that the CTD model predicts unrealistically high exergetic efficiencies, and as such is omitted from any further studies. A dissipative thermal loss parameter that can account for the exergetic losses due to the parasitic, cyclic phase change and heat exchange within the device is included in the LTP and DHX models in an effort to make realistic predictions of the exergetic efficiencies. A parametric study on the LTP and DHX models, including and excluding the thermal loss parameter is carried out and the results are compared to experimental data. It is found that the inclusion of the thermal loss parameter greatly improves the prediction of the exergetic efficiency in both the LTP and DHX models, both in trend and approximate magnitude. From the results

it is concluded that, on accounting for thermal losses, the DHX model achieves the best predictions of the key performance indicators of the NIFTE, that is, of the oscillation frequency and exergetic efficiency of the device. An investigation on the applicability of different working fluids for the NIFTE, based on the dynamic heat exchanger model including thermal losses, with emphasis on the effects of key thermodynamic properties on the maximum thermal efficiency of an idealised cycle and the predicted exergetic efficiency of the device is also carried out. The change in specific volume due to vaporisation and the maximum saturation pressure of the working fluid in the cycle are found to have a dominant role in determining these efficiencies. Thirty one pure working fluids are studied, under a given set of scenarios, each representing a different practical application for the NIFTE device. For the scenario where the maximum pressure of the engine is defined by the pumping application, higher efficiencies are predicted for wet and isentropic fluids. For the scenario where the hot and cold heat exchanger temperatures are set by the external heat source and sink, higher efficiencies are predicted by dry and isentropic fluids. In this work, it is estimated that, with optimised designs and well-selected working fluids, the NIFTE may be capable of thermal efficiencies in the range 1 – 5 % when operating with low-grade heat at temperatures from 50 to 100 °C, with current best performance of 1.5 % at 80 °C.

List of Figures

1.1 (a) Schematic diagram of a Carnot engine where Q_{H} is the heat at the hot temperature T_{H}, Q_{C} is the heat at the cold temperature T_{C}, and W is the work. (b) Temperature-entropy diagram of the Carnot cycle, where T_{H} and T_{C} are the temperatures of the heat source and sink, respectively. Isothermal heat addition occurs between States 1 and 2, isentropic expansion during States 2 and 3, isothermal heat rejection between States 3 and 4, and isentropic compression between States 4 and 1. 16

1.2 (a) Schematic diagram of a typical Rankine cycle and (b) temperature (T) – entropy (s) diagram of the Rankine cycle with n-pentane as there working fluid. Isentropic compression occurs between States 1 and 2, isobaric heat addition during States 2 and 3, isentropic expansion between States 3 and 4, and isobaric heat rejection between States 4 and 1. . . . 18

1.3 Prototype of the NIFTE taken from Ref. [1]. 21

1.4 Temperature (T) – entropy (S) phase diagram of the working fluid (dotted line), n-pentane, used in the NIFTE prototype [2], and T–S diagram of a typical linearised thermodynamic cycle undergone by the working fluid contained within the device (solid line). 22

1.5 (a)Schematic of the hot heat exchanger (HHX) and cold heat exchanger (CHX) in the NIFTE and (b) Heat exchangers used in the NIFTE prototype showing the fins, taken from Ref. [2], page 171. 23

1.6 Schematic diagram showing the experimental setup of the NIFTE with (a) a dynamic load, taken from Ref. [2] page 126 and (b) a hydrostatic load taken from Ref. [2] page 161. . . . 24

1.7 Schematic diagram of the NIFTE device. The hot heat exchanger (HHX) and cold heat exchanger (CHX) blocks are found within the combined thermal domain 'th'. The power and displacer (heat exchanger) cylinders are denoted by 'p' and 'd', the feedback connection and valve by 'f', and the load line by 'l'. The connected vapour space above the liquid in the power and displacer cylinders, and also in the horizontal pipe connecting the two at their highest point, has been assumed previously (but not herein) to be an adiabatic vapour volume, denoted by 'ad'. The horizontal dashed line indicates the equilibrium (time-mean) liquid-vapour interface (liquid level) position in the two vertical cylinders. 25

1.8 Schematic diagram showing the operation of the NIFTE from (a) to (d), where the arrows indicate the direction of movement of the vapour-liquid interface in the power (left) and displacer (right, with heat exchanger) cylinders, and the dotted horizontal line indicates the equilibrium position. In (a) the working fluid is condensing on the cold heat excanger (CHX), (b) hydrostatic effects cause the vapour-liquid interface of the working fluid to return to equilibrium, (c) the working fluid evaporates on the hot heat exchanger (HHX) and, (d) hydrostatic effects cause the vapour-liquid interface of the working fluid to return to equilibrium. 26

1.9 Circuit representation of the NIFTE first presented in Ref. [2], where P_i and U_i represents the pressure drop across and volumetric flow rate through component 'i'. 28

1.10 The rearrangement of the NIFTE circuit in Fig. 1.9 to a phase shift oscillator circuit, taken from Ref. [2], page 113. 29

1.11 Infrared images of the top of the power cylinder with (from left to right) 0 %, 12.5 % and 25 % nitrogen by volume, taken from Ref. [2], page 204. 31

2.1 Schematic diagram of the NIFTE, indicating the three sub-model sections: **A**, where viscous friction and pressure drag, plus liquid flow inertia dominate in the feedback connection (f) and load line (l); **B**, where gravity/hydrostatic effects plus liquid flow inertia dominate in the power (p) and displacer (d) cylinders; and **C**, where vapour compressibility dominates in the adiabatic vapour volume (ad). 35

2.2 The temperature or power gradient along the hot heat exchanger (HHX) and cold heat exchanger (CHX) assumed in the (a) LTP, (b) CTD and (c) DHX models for the NIFTE device, where T_{HX} is the temperature at the surface of the heat exchanger block, ΔT is the temperature difference between the surface of the heat exchangers and the working fluid and $\dot{Q}_{\mathrm{HX}}$ is the power input to the heat exchanger blocks. 45

2.3 Close-up of the heat exchangers, where y_{d} is the vapour-liquid interface height in the displacer cylinder and $y_{C_{\mathrm{hx}}}$ is the height of the heat exchangers that participates in heat exchange with the working fluid. 46

2.4 Electrical circuit representation of the NIFTE (refer to Fig. 1.7) for the: (a) LTP, (b) CTD, and (c) DHX models. Here, k_j corresponds to the feedback gain for model 'j', R_i to a resistance, C_i to a capacitance, L_i to an inductance, P_i to a pressure and U_i to a volumetric flow-rate. Subscript 'hx' denotes the heat exchangers, 'th' the thermal domain, 'ad' the adiabatic domain, 'l' the load, 'p' the power cylinder, 'd' the displacer (heat exchanger) cylinder, and 'f' the feedback connection. 51

2.5 Closed-loop representation of the NIFTE where $G(s)$ is the modelled forward-loop transfer function between P_{th} and P_{d}, and k_i is the feedback gain for model 'i'. 53

2.6 Thermodynamic cycle undergone by a wet working fluid associated with an ideal theoretical vapour-cycle engine without mechanical-shaft components that can only interface with a low-pressure reservoir and a high-pressure load, or a low-temperature sink and high-temperature source, imposed externally by a specific application, featuring the following processes: compression of the saturated liquid by sudden exposure to the high pressure reservoir/load conditions (States 1 to 2), reversible isobaric (and isothermal) heat addition (States 2 to 3), expansion of the saturated vapour by sudden discharge into the low pressure surrounding environment/atmospheric conditions (States 3 to 4), and reversible isobaric (and isothermal) heat rejection (States 4 to 1). The engine can only exchange heat and work during the processes involving positive-displacement phase-change of the working fluid (i.e. from States 2 to 3 and States 4 to 1). 54

3.1 Stability plots for the LTP model. Effect of perturbing the main parameters feedback valve resistance R_f (dashed line), load line resistance R_l (solid line) and load line inertia L_l (dotted line) on the value of $(\mathrm{d}T/\mathrm{d}y)_\mathrm{HX}$ required for marginal stability; (a) without inductances, and (b) with inductances. Note, each parameter is shown normalised to their nominal value denoted by the superscript '*' and the solid vertical line marks the nominal value and point for all parameters. 65

3.2 Effect of R_f (dashed line), R_l (solid line) and L_l (dotted line) on oscillation frequency predicted by the LTP model; (a) without, and (b) with inductances. Note, each parameter is shown normalised to their nominal value denoted by the superscript '*' and the solid vertical line marks the nominal value and point for all parameters. 67

3.3 Effect of perturbing load parameters; resistance R_l (dashed line) and inertia L_l (solid line), and feedback resistance R_f (dotted line), on the exergetic efficiency η_ex of the system; (a) without, and (b) with inductances. Note, each parameter is shown normalised to their nominal value denoted by the superscript '*' and the solid vertical line marks the nominal value and point for all parameters. 68

3.4 Effect of (a) the capacitance in the power cylinder C_p and (b) the resistance in the feedback tube R_f, on the oscillation frequency f_0 from the non-inertive model and comparison with prediction from Eq. (3.1). The dashed lined represents the results from Eq. (3.1), and the solid and dotted lines represent results at $C_p = 7.43 \times 10^{-8}$ and $C_p = 3.22 \times 10^{-9}$ m^4.s^2/kg, respectively. Note, each parameter is shown normalised to their nominal value denoted by the superscript '*'. 71

3.5 Effect of inertia on the variations in oscillation frequency f_0 due to (a) feedback tube resistance R_f and (b) load resistance R_l, with nominal capacitance in the power cylinder $C_p = 7.43 \times 10^{-8}$ m^4.s^2/kg, where the dashed and solid lines are results from the model with and without inductances, respectively. In the case of the non-inertive result we plot $f_0/10$. Note, each parameter is shown normalised to their nominal value denoted by the superscript '*'. 72

3.6 Effect of (a) the resistance in the feedback tube (R_f) and (b) the inertia in the feedback tube (L_f) on the marginal stability frequency f_0 of the three models; LTP (solid line), CTD (dashed line) and DHX (dotted line), respectively. The vertical dashed line indicates the position of the parameter nominal value. 74

3.7 Effect of (a) the resistance in the feedback tube (R_f) and (b) the inertia in the feedback tube (L_f) on the device exergetic efficiency η_ex of the three models; LTP (solid line), CTD (dashed line) and DHX (dotted line), respectively. The vertical dashed line indicates the position of the parameter nominal value. 75

3.8 Effect of R_f (solid line) and L_f (dashed line) on the feedback gain of the (a) LTP, (b) CTD and (c) DHX models. The vertical dashed line indicates the position of the parameter nominal value. 77

3.9 Effect of (a) R_f and (b) L_f on the marginal stability frequency f_0 on the exergetic efficiency η_ex, for the LTP model (dash-dot line) and DHX model at various C_hx values. The vertical dashed line indicates the position of the parameter nominal value. 78

3.10 Effect of (a) R_f and (b) L_f on the exergetic efficiency η_ex, for the LTP model (dash-dot line) and DHX model at various C_hx values. Note in (a), the $C^*_{hx} = 0.02$ line is superimposed by the LTP line. The vertical dashed line indicates the position of the parameter nominal value. 79

3.11 Effect of (a) R_f and (b) L_f on the marginal stability frequency f_0 for the LTP model at nominal values (black solid line), low R_l (square symbol), high R_l (triangle symbol), low L_l (dotted black line) and high L_l (dashed black line). The vertical dashed line indicates the position of the parameter nominal value. 81

3.12 Effect of (a) R_f and (b) L_f on the marginal stability frequency f_0 for the DHX model at nominal values (black solid line), low R_l (square symbol), high R_l (triangle symbol), low L_l (dotted black line) and high L_l (dashed black line). The vertical dashed line indicates the position of the parameter nominal value. 82

3.13 Effect of (a) R_f and (b) L_f on the exergetic efficiency η_ex for the LTP model at nominal values (black solid line), low R_l (square symbol), high R_l (triangle symbol), low L_l (dotted black line) and high L_l (dashed black line). The vertical dashed line indicates the position of the parameter nominal value. 83

3.14 Effect of (a) R_f and (b) L_f on the exergetic efficiency η_ex for the DHX model at nominal values (black solid line), low R_l (square symbol), high R_l (triangle symbol), low L_l (dotted black line) and high L_l (dashed black line). The vertical dashed line indicates the position of the parameter nominal value. 84

3.15 Root locus of the closed loop poles for the LTP model on the Argand diagram, showing the shift in the dominant (purely imaginary) marginal pole (circled) with a change in parameter L_f, from (a) $L_f = 2.78 \times 10^5\,\mathrm{kg\,m^{-4}}$ to (b) $L_f = 2.87 \times 10^5\,\mathrm{kg\,m^{-4}}$. N.B.: There are 5 poles in total; the rest are not shown and lie in the stable left-hand side of the diagram, with a negative real part. 85

4.1 Illustration of the unsteady thermal loss impedance Z_TL due to irreversible heat transfer, which includes both the convective evaporation/condensation heat transfer loss associated with the heat transfer coefficient h, and the unsteady conduction heat transfer loss through the solid wall with thickness l_gl. 90

4.2 Electrical circuit representations of the NIFTE (see Fig. 1.7) for the: (a) $\mathrm{LTP_{TL}}$; and (b) $\mathrm{DHX_{TL}}$ models, where k_j corresponds to the feedback gain for model 'j', R_i to a resistance, C_i to a capacitance, L_i to an inductance, P_i to a pressure and U_i to a volumetric flow-rate. Subscript 'hx' refers to the heat exchangers, 'th' to the thermal domain, 'TL' to the unsteady thermal loss, 'ad' to the adiabatic vapour volume, 'l' to the load, 'p' to the power cylinder, 'd' to the displacer cylinder, and 'f' to the feedback line and valve. 96

4.3 The effect of load resistance R_l on the: (a) frequency of oscillation (operation) f_0; and (b) exergetic efficiency η_ex. Results are shown from the LTP model (solid line), nominal DHX model (dashed line), and DHX model with twice the nominal heat exchanger capacitance value $2\widetilde{C}_\mathrm{hx}$ (dotted line). Also shown are experimental data points from a NIFTE water pump prototype. 106

4.4 The effect of the timescale parameter $R_\mathrm{f}C_\mathrm{d}$ at constant displacer hydrostatic capacitance C_d on the predictions of the NIFTE: (a) frequency f_0; and (b) exergetic efficiency η_ex. Showing results from the LTP model (solid line), nominal DHX model (dashed line), and DHX model with $2\widetilde{C}_\mathrm{hx}$ (dotted line). 107

4.5 The effect of the timescale parameter $R_f C_d$ at constant displacer hydrostatic capacitance C_d on the predictions of the NIFTE: (a) frequency f_0; and (b) exergetic efficiency η_{ex}. Showing results for the revised models featuring the unsteady thermal loss impedance Z_{TL} with an *isothermal* boundary condition, namely $\text{LTP}_{\text{ISOTL}}$ (solid line), $\text{DHX}_{\text{ISOTL}}$ (dashed line), and $\text{DHX}_{\text{ISOTL}}$ with $2\widetilde{C}_{hx}$ (dotted line). 109

4.6 The effect of the timescale parameter $R_f C_d$ at constant displacer hydrostatic capacitance C_d on the predictions of the NIFTE: (a) frequency f_0; and (b) exergetic efficiency η_{ex}. Showing results for the revised models featuring the unsteady thermal loss impedance Z_{TL} with an *adiabatic* boundary condition, namely LTP_{ADTL} (solid line), DHX_{ADTL} (dashed line), and DHX_{ADTL} with $2\widetilde{C}_{hx}$ (dotted line). 110

4.7 Linearised T–S cycle diagrams for the NIFTE predicted by the: (a) LTP model; (b) LTP_{TL} model; (c) nominal DHX model; and, (d) DHX_{TL} model, where the prime $(\cdot)'$ denotes the fluctuation around the time-averaged value of variable $(\cdot)$. The solid black lines represent the net exergy made available to the device, and the dotted black lines represent the net exergy gained by the working fluid. The difference between the two cycles amounts to the exergy (useful work) destruction at the boundary between the working fluid and the heat exchangers, due to irreversible heat transfer. 113

4.8 Linearised P_{ad}–V_l diagrams for the NIFTE predicted by the LTP and DHX models: (a) excluding; and, (b) including, irreversible unsteady thermal loss effects. Comparison with a corresponding experimental P_{ad}–V_l diagram (red cycle) from a NIFTE prototype, taken from Ref. [2]. 115

5.1 The working fluid thermal efficiency η_{wf} for n-pentane, ammonia, water and R245ca against: (a) the heat addition saturation temperature T_{sat}, and (b) the temperature ratio $T_r = T_{sat}/T_{crit}$. (c) The working fluid exergy efficiency $\eta_{wf,ex} = \eta_{wf}/\eta_{Carnot}$ against the temperature ratio T_r. 123

5.2 The working fluid thermal efficiency η_{wf} for *n*-pentane on varying the maximum pressure P_{max}, saturation temperature T_{sat}, change in entropy due to vaporisation Δs_{vap}, and change in volume due to vaporisation Δv_{vap}, where: (a) each thermodynamic property is varied individually, (b) the sensitivity of η_{wf} to each individual thermodynamic property θ is considered, and (c) combinations of the thermodynamic properties are varied. 124

5.3 The exergy efficiency η_{ex} predicted by the DHX_{TL} model with *n*-pentane as the working fluid on varying the change in volume due to vaporisation Δv_{vap}, maximum pressure P_{max}, change in entropy due to vaporisation Δs_{vap}, liquid phase density ρ_{lq}, adiabatic index γ, and saturation temperature T_{sat}. The nominal values for the saturation properties are set to: (a) $T_{sat,nom} = 293.15\,K$, (b) $T_{sat,nom} = 333.15\,K$, and (c) $T_{sat,nom} = 393.15\,K$. 127

5.4 The exergy efficiency η_{ex} predicted by the DHX_{TL} model with *n*-pentane as the working fluid on varying combinations of the thermodynamic properties from the following list: change in volume due to vaporisation Δv_{vap}, saturation pressure P_{sat}, change in entropy due to vaporisation Δs_{vap}, liquid phase density ρ_{lq}, adiabatic index γ, and saturation temperature T_{sat}. The nominal values for the saturation properties are set to: (a) $T_{sat,nom} = 293.15\,K$, (b) $T_{sat,nom} = 333.15\,K$, and (c) $T_{sat,nom} = 393.15\,K$. 128

5.5 (a) Exergy efficiency η_{ex}, thermal efficiency η_{th} and working fluid efficiency η_{wf}, (b) oscillation frequency f_0, and (c) normalised power output per unit heat input $f_0\eta_{ex}$ for different working fluids and a system working against a 1 m head. 133

5.6 (a) Exergy efficiency η_{ex}, thermal efficiency η_{th} and working fluid efficiency η_{wf}, (b) oscillation frequency f_0, and (c) normalised power output per unit heat input $f_0\eta_{ex}$ for different working fluids and a system working against a 10 m head. 134

5.7 (a) Exergy efficiency η_{ex}, thermal efficiency η_{th} and working fluid efficiency η_{wf}, (b) oscillation frequency f_0, and (c) normalised power output per unit heat input $f_0\eta_{ex}$ for different working fluids and a system working against a 30 m head. 135

5.8 (a) Exergy efficiency η_{ex}, thermal efficiency η_{th} and working fluid efficiency η_{wf}, (b) oscillation frequency f_0, and (c) normalised power output per unit heat input $f_0\eta_{ex}$ for different working fluids and a system working with a hot heat exchanger temperature of 333.15 K. . 137

5.9 (a) Exergy efficiency η_{ex}, thermal efficiency η_{th} and working fluid efficiency η_{wf}, (b) oscillation frequency f_0, and (c) normalised power output per unit heat input $f_0\eta_{ex}$ for different working fluids and a system working with a hot heat exchanger temperature of 353.15 K. . 138

5.10 (a) Exergy efficiency η_{ex}, thermal efficiency η_{th} and working fluid efficiency η_{wf}, (b) oscillation frequency f_0, and (c) normalised power output per unit heat input $f_0\eta_{ex}$ for different working fluids and a system working with a hot heat exchanger temperature of 373.15 K. . 139

5.11 The exergy efficiency η_{ex} predicted by the DHX_{TL} model for: (a) a system working with a hot heat exchanger temperature of 60 °C, 80 °C and 100 °C, and a cold heat exchanger temperature of 293 K, against the maximum pressure for all working fluids, and (b) a system working against a 1 m, 10 m, 30 m and 100 m head, with a suction/supply pressure of 1 atm, against the maximum saturation temperature for all working fluids. 141

5.12 With the heat source (HHX) temperature T_{sat} set to some (variable) value and the heat sink (CHX) temperature set to 20 °C: (a) maximum ideal working fluid thermal efficiency η_{wf} over all working fluids tested in this study and NIFTE device thermal efficiency η_{th} (shown here multiplied by a factor of $\times 10$), and (b) maximum ideal working fluid exergy efficiency $\eta_{wf,ex}$ over all working fluids tested in this study and NIFTE device exergy efficiency η_{ex} (multiplied by a factor of $\times 10$). With the load pressure P_{max} set to some (variable) value and the suction/supply pressure set to 1 atm: (c) maximum ideal working fluid thermal efficiency η_{wf} over all working fluids tested in this study and NIFTE device thermal efficiency η_{th} (multiplied by a factor of $\times 10$), and (d) maximum ideal working fluid exergy efficiency $\eta_{wf,ex}$ over all working fluids tested in this study and NIFTE device exergy efficiency η_{ex} (shown here multiplied by a factor of $\times 10$). 142

List of Tables

2.1 Transfer functions for the three models (LTP, CTD and DHX) in Fig. 2.4(a), (b) and (c) . . 52

2.2 Electrical analogies in the NIFTE and relations for resistances (R_i), capacitances (C_i) and inductances (L_i). 52

3.1 Values for the thermodynamic properties in Table 2.2, where liquid n-pentane and water data are taken at 298.15 K and 1 atm and n-pentane vapour data is taken as saturated at 1 atm. 62

3.2 Nominal values and investigated ranges of variables in Table 2.2 63

3.3 Calculated nominal values and investigated ranges for the parameters in Table 2.2 63

3.4 Selection of perturbed values for parameters R_{th}, R_{l}, R_{f}, C_{ad}, C_{p}, C_d and showing the frequencies obtained from the non-inertive model and results from Eq. (3.1) and approximations (i) $|P_1/P_2| \gg 1$, (ii) $|P_1/P_3| \gg 1$, and (iii) $|U_f/U_l| \ll 1$ in Section 3.3.4 69

3.5 The extent by which C_{p}, L_{p} and L_{f} need to be perturbed by in order to observe a discontinuity in the marginal stability plot in each of the three models: LTP, CTD and DHX 86

4.1 Electrical analogies in the NIFTE and relations for resistances (R_i), capacitances (C_i) and inductances (L_i). Note that $\overline{U}_i$ denotes the time-averaged volumetric flow-rate, U, in component i. 98

4.2 Transfer functions for the $\mathrm{LTP_{TL}}$ and $\mathrm{DHX_{TL}}$ models shown in Fig. 4.2. 98

4.3 Comparison of parameter values presented in Ref. [2] and the values of the parameters in Table 2.2 considered here as best estimates for the *nominal* experimental configuration of the NIFTE prototype. 100

4.4 Data from experiments with a varying R_l reported in Ref. [2], where R_l is the load resistance, $\omega_0 = 2\pi f_0$ is the angular frequency and f_0 is the oscillation frequency. 101

4.5 Data from experiments with a varying R_f reported in Ref. [2], where R_f is the feedback resistance, C_d is the hydrostatic capacitance in the displacer cylinder, $\omega_0 = 2\pi f_0$ is the angular frequency, τ is the period and η_{ex} is the device exergetic efficiency. The re-scaled $R_f C_d$ values are based on a minimum feedback valve opening of $\xi = 40$ %. 102

4.6 Investigated ranges and nominal values for the parameters defined in Table 2.2. 103

5.1 List of working fluids investigated, ordered from top to bottom by decreasing exergy efficiency η_{ex} at a HHX and maximum saturation temperature T_{sat} of 333.15 K (or, 60 °C). . . 130

Contents

1 Introduction **15**

1.1 Heat grade and utilisation 15

1.2 Low-grade heat 17

1.3 Non-Inertive-Feedback Thermofluidic Engine 21

1.3.1 Configuration 22

1.3.2 Operation 27

1.4 Early modelling attempts 27

1.5 Aims and objectives of present work: modelling extensions and system optimisation . . . 32

2 Model Development for the NIFTE **34**

2.1 Electrical analogies 34

2.2 Electrical components: resistors, capacitors and inductors 36

2.3 Model development 37

2.3.1 Fluid domain 37

2.3.2 Thermal domain 43

2.4 Oscillation frequency 52

2.5 Efficiency definitions 54

2.5.1 Working fluid thermal efficiency (η_{wf}) 54

2.5.2 NIFTE exergy efficiency (η_{ex}) 56

2.5.3 NIFTE thermal efficiency (η_{th}) 57

2.6 Summary 58

3 Parametric Investigation on LTP, CTD and DHX models **59**

3.1 LTP, CTD and DHX models . . . 60

3.2 Parameter values and investigated Ranges . . . 62

3.3 Comparison of the LTP model with and without inertia . . . 63

3.3.1 Required gain or heat exchanger temperature gradient . . . 64

3.3.2 Oscillation frequency . . . 66

3.3.3 Exergetic efficiency . . . 66

3.3.4 Simplifying approximations . . . 69

3.4 Comparison of LTP, CTD and DHX models . . . 70

3.4.1 Oscillation frequency f_0 and exergetic efficiency η_{ex} . . . 73

3.4.2 Feedback gain and heat exchange implications . . . 73

3.4.3 Effect of heat exchanger capacitance C_{hx} in the DHX model . . . 76

3.4.4 Further LTP and DHX model comparison . . . 80

3.4.5 Discontinuity in the marginal stability frequency f_0 . . . 85

3.5 Summary of chapter findings . . . 86

4 Thermal Losses in the NIFTE **89**

4.1 Loss mechanisms . . . 90

4.2 Accounting for thermal losses . . . 91

4.2.1 Conduction . . . 92

4.2.2 Phase-change convection . . . 93

4.2.3 Linear temperature profile (LTP) . . . 94

4.2.4 Dynamic heat exchanger (DHX) . . . 95

4.3 Redefining feedback and load resistances . . . 96

4.4 Results . . . 99

4.4.1 Parameter uncertainties . . . 99

4.4.2 Comparison with experimental data . . . 104

4.4.3 Thermodynamic cycle diagrams . . . 114

4.5 Summary of chapter findings . . . 116

5 Working Fluid Investigation **118**

5.1 Thermodynamic properties 119

5.2 Application scenarios 119

5.3 Results and Discussion 120

5.3.1 Parametric and sensitivity study on η_{wf} 120

5.3.2 Parametric study on η_{ex} 126

5.3.3 Working fluid comparison 129

5.4 Summary of chapter findings 142

6 Conclusions and Future Work **145**

6.1 Future work 149

6.1.1 Experimental data 149

6.1.2 Heat exchanger modelling 149

6.1.3 Working fluid design 150

6.1.4 Optimisation 150

1 Introduction

1.1 Heat grade and utilisation

In 1824, a French physicist by the name of Nicolas Léonard Sadi Carnot defined an ideal heat engine [3], which went on to be one of the most important definitions in thermodynamics. This work would go on to be the foundation for the work carried out by Èmile Clapeyron [4] and subsequently Rudolf Clausius [5] in defining the second law of thermodynamics. The engine proposed by Carnot, aptly known as the Carnot engine, assumes that all the processes within the cycle are reversible and as such have no losses.

In a Carnot engine, shown in Fig. 1.1(a), heat flows through a fluid from a hot temperature T_{H} source to a cold temperature T_{C} sink, thereby causing the fluid to do work W on its surroundings [6]. The thermodynamic cycle of an ideal Carnot engine is shown in the temperature-entropy diagram in Fig. 1.1(b). The process undergone between each thermodynamic state point is:

$1 \rightarrow 2$ Isothermal and reversible heat addition (expansion),

$2 \rightarrow 3$ Adiabatic and reversible (isentropic) expansion,

$3 \rightarrow 4$ Isothermal and reversible heat rejection (compression) and,

$4 \rightarrow 1$ Adiabatic and reversible (isentropic) compression.

The thermal efficiency of any heat engine is defined as the ratio of the net work done to the heat input. Following from this definition, the thermal efficiency of the Carnot engine (η_{Carnot}) is, based on the schematic shown in Fig. 1.1(a), W/Q_{H}. As all processes are assumed to be reversible, the thermal efficiency can be simplified to,

$$\eta_{\mathrm{Carnot}} = 1 - \frac{T_{\mathrm{C}}}{T_{\mathrm{H}}}, \tag{1.1}$$

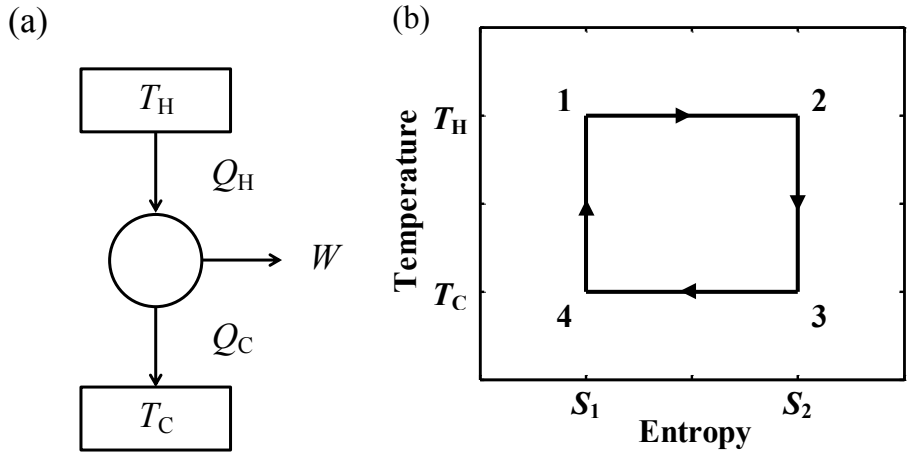


Figure 1.1: (a) Schematic diagram of a Carnot engine where Q_H is the heat at the hot temperature T_H, Q_C is the heat at the cold temperature T_C, and W is the work. (b) Temperature-entropy diagram of the Carnot cycle, where T_H and T_C are the temperatures of the heat source and sink, respectively. Isothermal heat addition occurs between States 1 and 2, isentropic expansion during States 2 and 3, isothermal heat rejection between States 3 and 4, and isentropic compression between States 4 and 1.

where T_C is the temperature of the heat sink and T_H is the temperature of the heat source. Based on his findings, Carnot stipulated that [3]:

1. Any Carnot engine operating between the same temperature heat source and sink, where the temperature of the heat source is greater than the temperature of the heat sink, will have the same thermal efficiency defined by Eq. (1.1), and

2. Any heat engine operating between a heat source and sink will have a thermal efficiency less than the equivalent Carnot efficiency.

Following on from the second point, any real process that is undergone in a heat engine cycle is irreversible, that is there are unavoidable losses as a result of the process taking place. Therefore the efficiency of any real engine cannot equal or exceed the Carnot efficiency. As a result, the Carnot efficiency is used as an indication of the maximum theoretical thermal efficiency a process can achieve.

From Eq. (1.1) it can be seen that the Carnot efficiency tends towards unity as the temperature difference between the heat source and sink increases, that is a Carnot efficiency of unity can only be achieved if the cold sink is at 0 K or if the heat source is infinitely large. The Carnot efficiency of the heat engine will be zero when the temperature of the heat source and heat sink are equal, that is $T_H = T_C$. As a result, industrial

process with a 'high-temperature' heat source would inherently have a higher maximum efficiency than processes with a 'low-temperature' heat source. For this reason the industry of power generation has been dominated by high-temperature heat engines.

A common source of energy for high-temperature power generation is fossil fuels, such as coal, natural gas and oil, as they are energy-dense form of fuel which can easily be stored and transported [7]. The global average efficiency, found from investigating 14 countries, for coal, natural gas and, oil-fired plants up until 2003 was found to be 35%, 45% and 38%, respectively [8]. However, the combustion of fossil fuels leads to the emissions of harmful green house gases (GHGs), including but not limited to carbon dioxide, methane and nitrous oxide. These emissions have a detrimental effect of the climate and as a result the Kyoto protocol was drawn up to set a global initiative to reduce emissions [9]. One method by which emissions from fossil fuel plants were reduced was increasing the efficiency. In the European Union, the efficiency of coal-fired plants increased by 4 % from 1990 to 2005, and is expected to increase by a further 2 % by 2015 [10]. Similarly, the efficiency gas-fired plants increased by 16 % and is expected to increase by a further 4 % [10].

Despite the progress on increasing the efficiency of fossil fueled power generation, there is a limit to not only the increase in efficiency, but also the availability of the resources. In 2009, it was estimated that the reserves of oil, natural gas and coal would deplete in approximately 35, 37 and 107 years, respectively [11]. As the aforementioned fossil fuels are the main sources of energy for power generation, much work has been done in the use and implementation of alternative sources of energy.

There has been a large focus on the use of renewable energy sources, that is energy sources that are stored continuously such as solar, wind and geothermal energy, to be used to compensate for the depleting fossil fuels reserves. In 2011, renewable resources contributed 16 % to the global energy consumption [12], and this is set to increase. Another group of energy resources that has become increasingly popular in recent years, due to its increase economic viability and lower environmental impact, is low-grade heat [13].

1.2 Low-grade heat

Low-grade heat is an umbrella term used to identify any source of heat available at low temperature, relative to ambient temperature. The main sources of low-grade heat are solar thermal, geothermal and industrial

waste heat, though it also includes any source of heat available at temperatures less than approximately 250 °C [14]. As low-grade heat is abundantly available from natural resources or as waste heat from processes, it is becoming an increasingly attractive source of energy.

An excellent review of the uses of low-grade, specifically in the form of waste heat from industrial processes was carried out by Ammar et al. [13]. In this review, low-grade heat is defined as heat that cannot be recovered within a process. Several uses of low-grade heat were identified, which are based on the temperature and the form of the heat. One use of low-grade heat is heating, for example, in Iceland where geothermal energy has been used since 1930 as a method of supplying district heating and it supplies 89 % of the space heating requirements in the country [15]. It is estimated that in Denmark, waste heat from power plants, industry, waste incinerators and combined heat and power (CHP) are used for district heating [16]. Another use for low-grade heat is cooling through heat pumps and refrigerators. Adsorption refrigeration for the production of ice, chilled water and air conditioning is found to be an efficient use of low temperature heat [17].

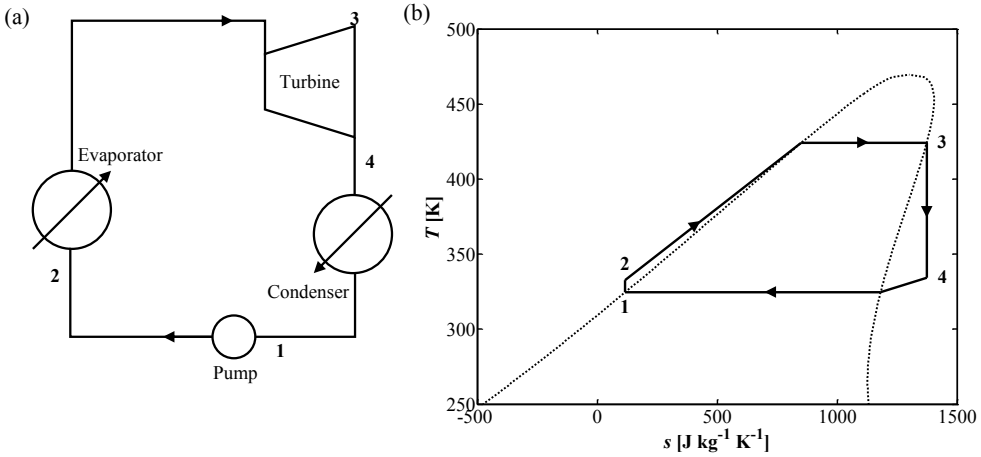


Figure 1.2: (a) Schematic diagram of a typical Rankine cycle and (b) temperature (T) – entropy (s) diagram of the Rankine cycle with n-pentane as there working fluid. Isentropic compression occurs between States 1 and 2, isobaric heat addition during States 2 and 3, isentropic expansion between States 3 and 4, and isobaric heat rejection between States 4 and 1.

One of the main technologies that has been investigated for the use of low-grade heat for power generation is the Rankine cycle. The most common working fluid used in a Rankine cycle is water, however this is not feasible at temperatures lower than 370 °C [18]. Therefore organic working fluids are more de-

sirable for the utilisation of low-grade heat. Rankine cycles or organic Rankine cycles (ORCs) are used to convert heat into electricity, through a process and cycle shown in the schematic diagram in Fig. 1.2. The main components are a pump, evaporator, condenser and turbine, through which power is extracted. The thermodynamic processes that occur in an ideal cycle, as shown in Fig. 1.2(b), are:

$1 \rightarrow 2$ Adiabatic and reversible (isentropic) compression,

$2 \rightarrow 3$ Isobaric heat addition,

$3 \rightarrow 4$ Adiabatic and reversible (isentropic) expansion and,

$4 \rightarrow 1$ Isobaric heat rejection.

Following from the previous definition for thermal efficiency, defined as the ratio between the net work out to the heat in, the thermal efficiency for a rankine cycle $\eta_{\text{th,Rankine}}$ is given as,

$$\eta_{\text{th,Rankine}} = \frac{W_{\text{turbine}} - W_{\text{pump}}}{Q_{\text{evaporator}}}, \tag{1.2}$$

where W_{turbine} is the work out of the turbine, W_{pump} is the work supplied to the pump, and $Q_{\text{evaporator}}$ is the heat into the evaporator. In processes utilising low-grade heat, it is becoming increasingly favoured to consider the efficiency of the process in relation to the maximum efficiency achievable. This relative efficiency is known as the exergetic efficiency, or second law efficiency. Here, exergy is defined as the maximum work that can be attained from an energy source or the maximum energy available to the system [19] such that the irreversibility due to an increase in entropy is accounted for. As previously shown, the maximum efficiency that can be achieved by a heat engine or heat pump is the Carnot efficiency (refer Eq. (1.1)), so the exergetic efficiency of an ORC $\eta_{\text{ex,Rankine}}$ is given as,

$$\eta_{\text{ex,Rankine}} = \frac{\eta_{\text{th,Rankine}}}{\eta_{\text{Carnot}}}. \tag{1.3}$$

There are several existing ORC technologies which have been adapted for the use of low-grade heat. These include the 30 – 65 kW “Green Machine” by ElectraTherm is quoted by the manufacturer as having an exergetic efficiency of $\sim$ 35 % when running with a hot water inlet temperature of 100 °C and a 20 °C cold water inlet temperature [20]. ENERBasque’s 25 kW “Prometheus” is quoted as having an exergetic efficiency of 32 – 34 % when running with hot water at 90 – 95 °C and cold water at 15 – 25 °C [21], and 26 – 27 % when running with hot water at 85 °C and the same cold water temperature.

Thermofluidic oscillators are a class of heat engines that are capable of converting low-grade heat into useful work. Unlike in ORCs where the heat is converted into electrical power, thermofluidic oscillators tend to convert heat into an oscillatory pumping action. The term 'thermofluidic oscillator' is used generally to describe a heat engine within which periodic thermodynamic (e.g. pressure, temperature), heat and fluid oscillations are induced from *steady* thermal boundary conditions (i.e. the external heat source and heat sink temperatures) [2]. Examples of thermofluidic oscillators include gas-cycle thermoacoustic engines [22–25], liquid-piston Fluidyne engines [26–28], free-piston Stirling engines (FPSE) [29, 30], and pulse-tube engines [31].

A liquid-piston Fluidyne engine is a form of a Stirling engine where the mechanical moving piston is replaced by liquid pistons. The Fluidyne engine pumps liquid through the use of non-return valves [28]. Another thermofluidic engine based on the Stirling engine is known as the free-piston Stirling Engine. As the name suggests, this engine has free pistons, that is pistons which are not mechanically coupled to each other [32]. FPSEs can be used for pumping liquids or connected to a linear alternator to generate electricity. The pulse-tube engine relies on a phase shift between the heat transfer to the gas and the movement of the gas within a tube. The expansion and compression work generated as a result is converted into mechanical work by means of a piston, which subsequently can be converted into electrical power [31].

A thermofluidic oscillator consists of compartments and interconnections that contain a working fluid, while typically featuring no (or few) moving mechanical parts. The working fluid is exposed to an externally imposed temperature difference that is established by a pair of heat exchangers; hot (interfacing with the heat source) and cold (interfacing with the heat sink). The temperature difference gives rise to alterations between successive heat addition (and evaporation of the working fluid) and rejection (and condensation of the working fluid) phases, at the hot and cold heat exchangers. The volume oscillations that arise from the phase change, lead, in turn, to an oscillatory, periodic fluid displacement (motion).

The main feature of thermofluidic oscillators that is of particular interest in the current work concerns their ability to operate across small temperature differences between the heat source and sink, making them ideal devices for the conversion of low-grade heat. The use of low-grade heat makes thermofluidic oscillators inherently inefficient compared to their high energy counterparts. However, the low (or zero) cost of their energy source, together with their increased reliability from the lack of mechanical moving parts, result in the advantages of lower operating and maintenance costs [33]. A particular two-phase (or, vapour-

cycle) thermofluidic oscillator realisation that the present work focuses on involves the alternating phase change of the working fluid, and known as the Non-Inertive-Feedback Thermofluidic Engine (NIFTE), was presented by Smith [2, 34, 35].

1.3 Non-Inertive-Feedback Thermofluidic Engine

In 2006, Smith [2] designed and built a bench-scale prototype of the Non-Inertive-Feedback Thermofluidic Engine (NIFTE), shown in Fig. 1.3. This engine is classified as a two-phase thermofluidic oscillator, where the working fluid undergoes periodic evaporation and condensation during operation, and so it is in the vapour phase and liquid phase simultaneously. A significant advantage the NIFTE has compared to other similar thermoacoustic or thermofluidic devices is the presence of phase change during operation, resulting in a higher heat transfer coefficient. In addition, the change of phase of the working fluid during operation only requires a small temperature difference between the heat source and sink for operation. The idealised thermodynamic cycle undergone in the NIFTE can be seen in Fig. 1.4. It is noted that the complete cycle takes place inside the two-phase saturation region of the working fluid, which is *n*-pentane based on the prototype developed by Smith [2].

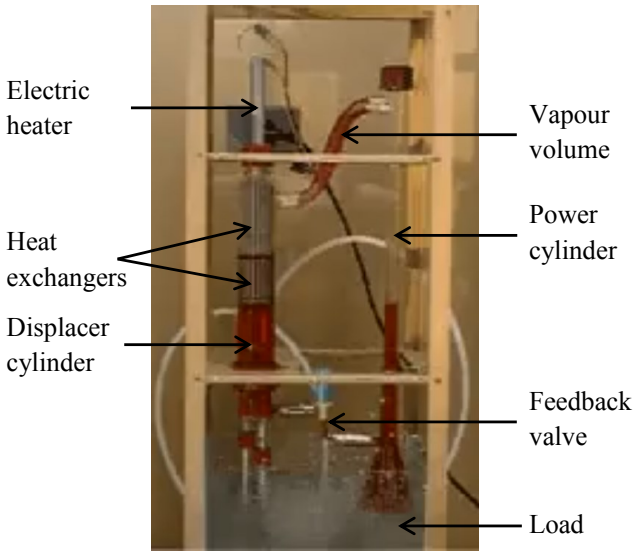


Figure 1.3: Prototype of the NIFTE taken from Ref. [1].

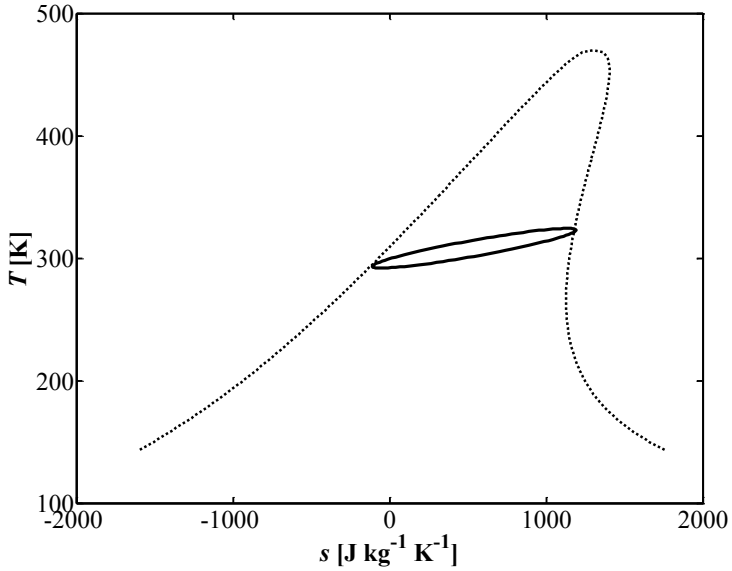


Figure 1.4: Temperature (T) – entropy (S) phase diagram of the working fluid (dotted line), n-pentane, used in the NIFTE prototype [2], and T–S diagram of a typical linearised thermodynamic cycle undergone by the working fluid contained within the device (solid line).

Due to the NIFTE's mechanical reliability, low capital investment and minimal running costs, it has become more economically viable in areas where pumps are not currently viable. The NIFTE is capable of pumping a variety of fluids including sensitive biological cultures and chemically or mechanically abrasive media. It is also capable of utilising low temperature heat, such as solar thermal energy to operate. A viable application for a solar powered NIFTE is low flow rate water pumping for drip irrigation.

1.3.1 Configuration

A prototype of the NIFTE, shown in Fig. 1.3, consists of two vertical glass cylinders connected by two horizontal plastic tubes, with a gate valve is fitted in the bottom tube. The working fluid in the prototype, n-pentane, has been coloured to distinguish it from the pumped liquid, water, from which it is immiscible. The working fluid also exists in the vapour phase, found above the liquid phase, though it is colourless.

Two heat exchangers are situated in the left hand cylinder, a hot heat exchanger (HHX) above a cold heat exchanger (CHX), which are necessary for operation. The HHX and CHX provide the external temperature difference necessary to drive the phase change of the working fluid in the NIFTE. The HHX is powered through an electrical heater which is inserted into the centre of the heat exchanger, whereas heat is removed

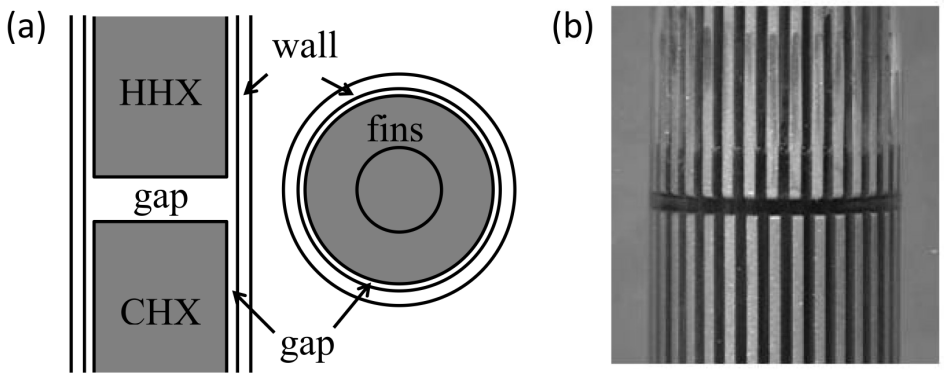


Figure 1.5: (a)Schematic of the hot heat exchanger (HHX) and cold heat exchanger (CHX) in the NIFTE and (b) Heat exchangers used in the NIFTE prototype showing the fins, taken from Ref. [2], page 171.

from the cold heat exchanger through an internal liquid pump, whose tubes can be seen just below the left cylinder. In an earlier prototype of the NIFTE, solid finger-like copper and borosilicate glass blocks were used for the hot and cold heat exchangers, respectively, however sustained oscillations could not be achieved due to the high thermal resistance. These finger-like blocks were replaced by deep finned cylindrical aluminium blocks, as shown in Fig. 1.5 [2], in an effort to increase the surface area and decrease the thermal resistance [2].

There were two experimental setups for the load in the NIFTE, which are shown in Fig. 1.6. The 'dynamic' load setup, shown in Fig. 1.6(a) uses an adjustable throttling valve which allows for easily and continuous change in position. The experimental data been presented by Smith [2] that has been used in the present study, has primarily used the dynamic load setup as it is useful when forming correlations with the linear models. The 'hydrostatic' setup shown in Fig. 1.6(b) uses two non-returning valves where a static head difference is imposed, which is more realistic representation for the use of the NIFTE.

In order to model the NIFTE, a simplified schematic diagram, shown in Fig. 1.7, was developed, in which the NIFTE is divided into sections. The white area in Fig. 1.7 represents the vapour phase and the grey area represents the liquid phase of the working fluid. As in the prototype, the general configuration of the NIFTE in the schematic consists of two vertical cylinders connected by two horizontal tubes. One of the two vertical cylinders known as the displacer cylinder, denoted by 'd' in Fig. 1.7, contains the hot heat exchanger (HHX) and cold heat exchanger (CHX), denoted by 'th' in Fig. 1.7. The oscillatory fluid

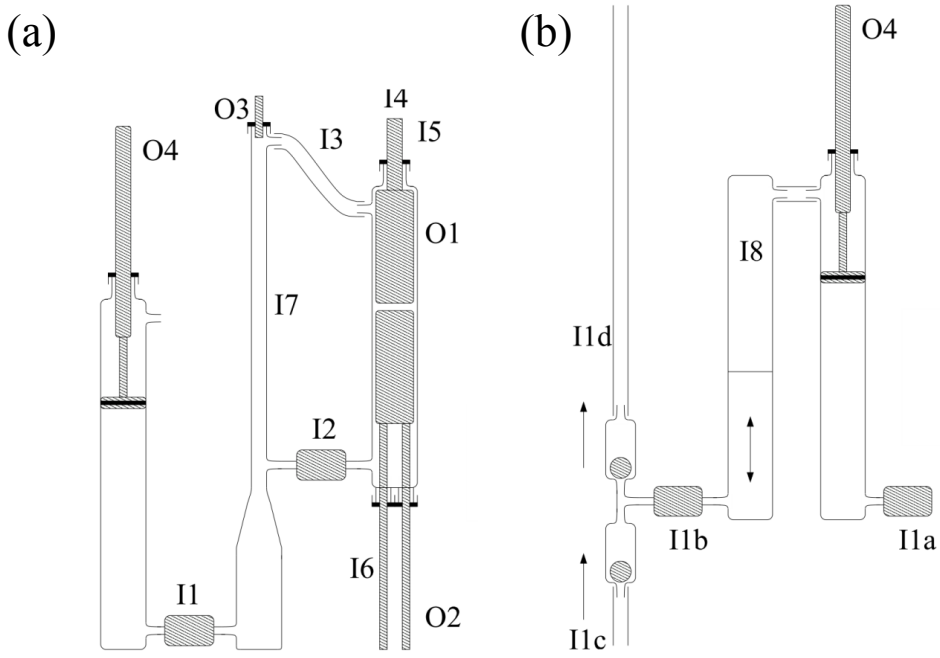


Figure 1.6: Schematic diagram showing the experimental setup of the NIFTE with (a) a dynamic load, taken from Ref. [2] page 126 and (b) a hydrostatic load taken from Ref. [2] page 161.

flow that occurs in the power cylinder (‘p’, in Fig. 1.7) as a result of this periodic phase change creates an inwards suction and a subsequent outward positive displacement of liquid in the load line (‘l’ in Fig. 1.7), so creating the desired pumping motion in the load, where useful work is done and measured.

Due to gravity the liquid phase is found in the lower parts of the device. The tube connecting the power cylinder and displacer cylinder, that contains the working fluid in the liquid phase, is referred to as the feedback connection (‘f’, in Fig. 1.7). The feedback tube features a valve that can be used to adjust the operation of the engine, if necessary during operation. The vapour phase collects in the upper part of the device in a combined vapour region that has been termed ‘adiabatic vapour volume’ (‘ad’, in Fig. 1.7). This denomination follows the conventional practice employed in the treatment of the NIFTE [2]. In reality the vapour volume is only nominally adiabatic, and in fact experiences parasitic cyclic heat transfer, which was not modelled in the work of Smith [2], but this will be considered in detail in the present thesis (see Chapter 4).

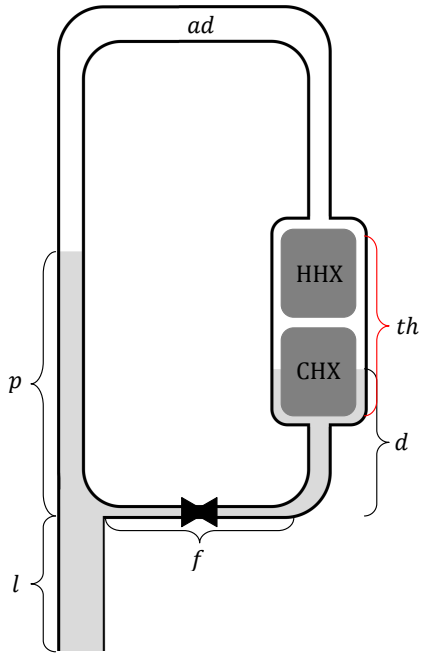


Figure 1.7: Schematic diagram of the NIFTE device. The hot heat exchanger (HHX) and cold heat exchanger (CHX) blocks are found within the combined thermal domain 'th'. The power and displacer (heat exchanger) cylinders are denoted by 'p' and 'd', the feedback connection and valve by 'f', and the load line by 'l'. The connected vapour space above the liquid in the power and displacer cylinders, and also in the horizontal pipe connecting the two at their highest point, has been assumed previously (but not herein) to be an adiabatic vapour volume, denoted by 'ad'. The horizontal dashed line indicates the equilibrium (time-mean) liquid-vapour interface (liquid level) position in the two vertical cylinders.

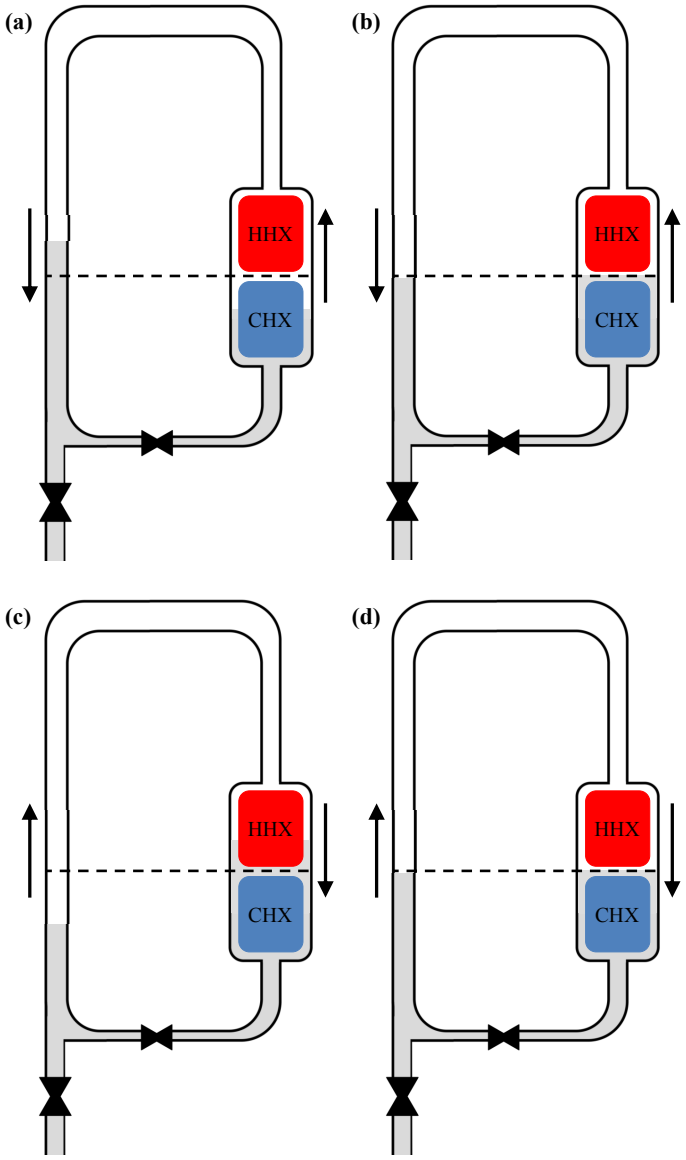


Figure 1.8: Schematic diagram showing the operation of the NIFTE from (a) to (d), where the arrows indicate the direction of movement of the vapour-liquid interface in the power (left) and displacer (right, with heat exchanger) cylinders, and the dotted horizontal line indicates the equilibrium position. In (a) the working fluid is condensing on the cold heat excanger (CHX), (b) hydrostatic effects cause the vapour-liquid interface of the working fluid to return to equilibrium, (c) the working fluid evaporates on the hot heat exchanger (HHX) and, (d) hydrostatic effects cause the vapour-liquid interface of the working fluid to return to equilibrium.

1.3.2 Operation

The NIFTE is an oscillating device in which all flows oscillate around an equilibrium point. The operation of the NIFTE is loosely demonstrated in the sequence of diagrams shown in Fig. 1.8. Briefly describing the operation of the NIFTE, the schematic in Figs. 1.8 and the starting point (furthest left diagram) in Fig. 1.8 shows the liquid level (i.e., vapour-liquid interface) in the displacer cylinder ('d', containing the heat exchangers) to be in contact with the cold heat exchanger block. At this point the working fluid in the vapour phase is condensing over the cold heat exchanger surface, which is at a temperature lower than the condensation temperature of the working fluid at the operation pressure. This causes a pressure decrease in the adiabatic vapour volume ('ad') and in turn allows the liquid level in the power cylinder ('p') to rise. At the same time, the hydrostatic pressure difference developing between the liquid levels in the power and displacer cylinders causes the levels to return back to equilibrium, that is when both liquid levels are at the same height (horizontal dashed line in Fig. 1.7), and then to overshoot this. The liquid level in the displacer cylinder then contacts the hot surface of the HHX block, which causes the working fluid in the liquid phase to evaporate. This causes a pressure increase in the adiabatic vapour volume that displaces the liquid level in power cylinder down further. Once more, the hydrostatic pressure difference between the liquid levels in the power and displacer cylinders causes the levels to return back to equilibrium and then to overshoot this, at which point the NIFTE returns back to the position shown in the far left of Fig. 1.8. This process repeats, leading to sustained oscillations from the stationary boundary conditions of the heat exchangers. The oscillations in the power cylinder are of great importance as they also affect the oscillations in the load ('l'), where (hydraulic; fluid pumping) work is done.

1.4 Early modelling attempts

A simple dynamic linear model for the NIFTE was developed by Smith [2]. This model involved compartmentalising the NIFTE device into suitable sections, and developing spatially lumped, linearised first-order sub-models for each component section. Analogies were then drawn between the governing equations of each sub-model in the device and linear passive electrical components, such as resistors, capacitors and inductors [36]. The component sub-models were interconnected to form an electrical circuit representation of the device, shown in Figs. 1.9 and 1.10.

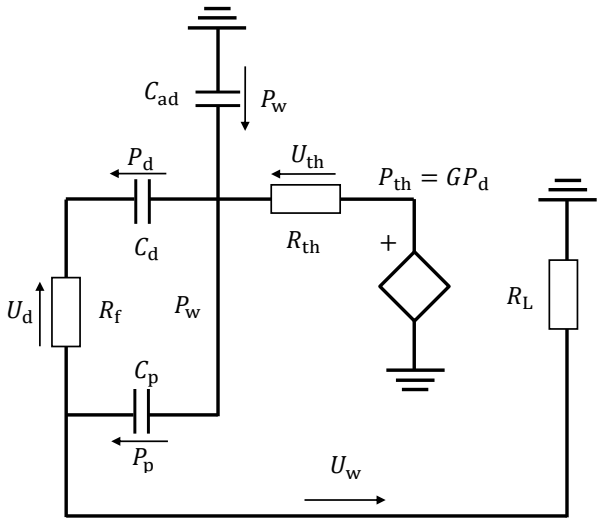


Figure 1.9: Circuit representation of the NIFTE first presented in Ref. [2], where P_i and U_i represents the pressure drop across and volumetric flow rate through component 'i'.

Electrical analogies have been used in a number of research fields, including the analysis of the permeation in a dense metal membrane [37], simulation of mass and charge transport in lithium-ion batteries [38] and the modelling of water transport in xylem [39]. Olson [40] summarises the use of electrical analogies to a number of disciplines, namely analogies between mechanical, acoustical, magnetic systems and electrical systems. There are three main electrical components used for this analogy; resistors, capacitors and inductors. Each of these electrical components can be described by a relation between the potential difference (E_i) across and the current (I_i) running through a component. In each of the aforementioned disciplines, these electrical components represent an aspect of the system. In order to form the analogies, the equivalent variables within each discipline that are represented by the potential difference and current need to be chosen. For example, typically in a mechanical system, force is represented by the potential difference and velocity is represented by the current [40]. As a result, a damper in a mechanical system is represented by a resistor, a spring is represented by a capacitor and mass is represented by an inductor.

More specifically, this approach has been used in modelling thermoacoustic systems and is provided in detail by Swift [33]. In a thermoacoustic system, the pressure is represented by the potential difference and the volumetric flow rate is represented by current. As such the resistance to fluid flow and viscous losses are represented as resistors, vapour compression and hydrostatic pressure are represented by capacitors

and the fluid mass is represented by inductors. Backhaus and Swift [41] used this method to model a thermoacoustic Stirling engine and Huang and Chung [42] used this method to model an orifice pulse-tube refrigerator. Both found this modelling method to be good at capturing the first-order dynamics of the devices. However there are some deviations which are attributed to the nonlinearities in the devices which cannot be captured by the linearised modelling method.

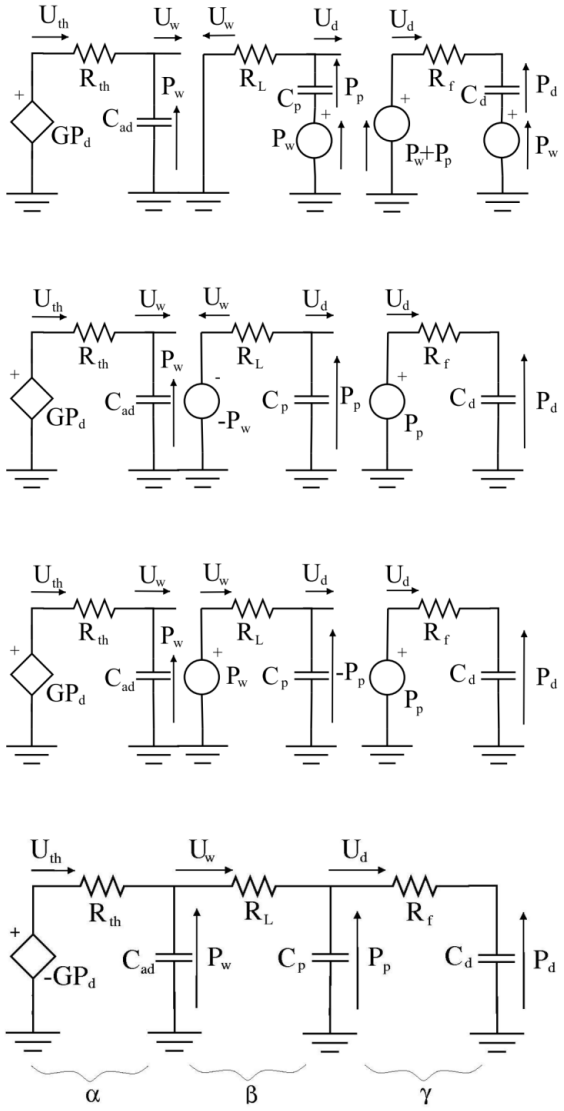


Figure 1.10: The rearrangement of the NIFTE circuit in Fig. 1.9 to a phase shift oscillator circuit, taken from Ref. [2], page 113.

Smith [2, 34, 35] extended the work done by Backhaus and Swift and Huang and Chung to develop a model for a thermofluidic oscillator, that did not depend on fluid inertia, in an effort to develop devices that can sustain higher pressure amplitudes that their inertia-dependant counterparts. Smith also introduced working fluid phase change so that high power densities could be achieved. In the previous thermoacoustic modelling methods [41, 42], spatially-dependant models were developed. Smith built upon this to develop dynamic, spatially lumped models for a theoretical two-phase thermofluidic engine. In addition, Smith extended the method to include thermal effects. In the thermal domain, analogies were made between the temperature and potential difference, and entropy flow and current. In order to develop the electrical circuit, two coupling equations were developed to link the thermal domain to the fluid domain, that is link temperature to pressure and entropy flow to volumetric flow rate. This will be discussed further in Chapter 2.

The initial circuit representation of the NIFTE, developed by Smith, is shown in Fig. 1.9. The circuit was rearranged to resemble a phase shift oscillator, where the steps taken are shown in Fig. 1.10. The first step was to identify three first order RC (resistor-capacitor) filters which had the same inputs and outputs as the circuit in Fig. 1.9.

An early prototype of the NIFTE that used *n*-pentane as the working fluid was reported to operate with a temperature difference as low as 30 K between the heat source and sink, with the temperature of the heat source being well within the limits of low-grade heat [43]. When operating with a $45-150$ W heat source at $65-90$ °C (via Joule heating in an electrical element embedded in the HHX), a heat sink at $4-12$ °C (via the circulation of pumped cooling ice-water through the CHX) and with *n*-pentane chosen to be the working fluid with a saturation temperature of 36 °C at the pumped pressure of $\sim$ 1 bar, this prototype achieved thermal efficiencies up to a little less than 1 % and exergetic efficiencies (as previously mentioned, the ration of the thermal efficiency to the Carnot efficiency) up to 1.7 % [2]. These efficiency values achieved by the early NIFTE prototype can be considered low when compared to: (i) the high thermal efficiency from a standing-wave heat engine of 18.4 %, reported by Backhaus and Swift [41] as recorded by Jin using the apparatus described by Godshalk et al. [44]; (ii) the travelling-wave heat engine of Backhaus and Swift [41] that reported exergetic efficiencies of up to 41 %; and (iii) the efficiencies associated with Fluidyne engines, typically around $3-4$ %, but as high as 7 % for some larger engines. Clearly, there is ample space for improvements to be made that can allow the NIFTE technology to achieve considerably higher efficiencies

than those attained by the early prototype.

The models developed by Smith were compared to experimental data using the aforementioned NIFTE prototype. The experiments were carried out at two hot heat exchanger temperature set points; low at 65 °C, and high at 90 °C. At both low and high hot heat exchanger temperatures, the model predicted oscillation frequency deviated from the experimental points. At the low temperature, this was particularly noticeable at low loads. This deviation was attributed to the attenuation of the displacer liquid piston as a result of asymmetric rate of heat transfer. Accounting for the attenuation in the displacer piston led to better oscillation frequency predictions.

The experimental exergetic efficiencies for the NIFTE were also compared to the model predictions. The exergetic efficiency of the NIFTE was found to be lower than those predicted by the model. This was attributed to the presence of additional loss mechanisms that had not been accounted for be the models. These two main loss mechanisms were identified to be entrance condensation and shuttle loss, where the latter was hypothesised to be the dominant cause of power loss, particularly at high loads. In order to reduce the losses, Smith proposed the introduction of nitrogen into the vapour volume (adiabatic chamber) [2]. Infrared images of the power cylinder with an increasing amount of nitrogen is shown in Fig. 1.11, from which it was determined that increasing the nitrogen volume in the vapour chamber decreased the shuttle loss and the entrance condensation.

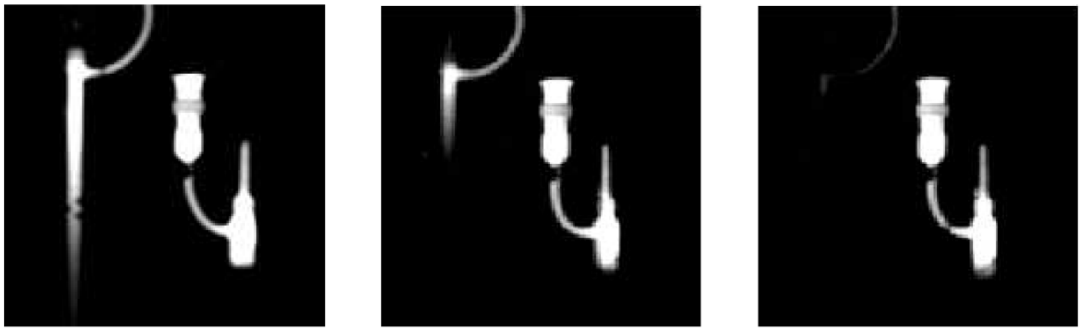


Figure 1.11: Infrared images of the top of the power cylinder with (from left to right) 0 %, 12.5 % and 25 % nitrogen by volume, taken from Ref. [2], page 204.

1.5 Aims and objectives of present work: modelling extensions and system optimisation

In this thesis, electrical analogies are used to model the NIFTE. The model for the NIFTE presented by Smith [2, 34, 35] neglected the effects of any liquid masses, that is inertia, in the NIFTE. However, a notable amount of the fluid volume, specifically some of the working fluid and the load, is in the liquid phase, shown in Fig. 1.7. The effect of liquid inertia is included in the NIFTE model presented by Smith [2], and is presented in Chapter 2. In Chapter 3, the inertive and non-inertive model for the NIFTE are compared.

The heat exchangers are perhaps the most important and at the same time most poorly understood components of the NIFTE. In the model presented by Smith, it was assumed that there was a linear temperature profile along the height of the hot and cold heat exchangers [2, 34, 35]. The linear temperature profile assumption is a reasonable starting point, however it is evident that it is also unrealistic since it implies an unbounded temperature increase in the hot heat exchanger and decrease in the cold heat exchanger. Two alternative heat transfer assumptions for the NIFTE are presented in Chapter 2; the first assuming there is a constant temperature difference between the temperature at the wall of the heat exchangers and the temperature of the working fluid, and the second taking into account the ability of heat exchangers to dynamically store and release heat. These models are compared with the original linear temperature profile assumption in Chapter 3 through parametric testing.

As previously mentioned, there are several loss mechanisms that have been identified within the NIFTE device, but have not been accounted for within the models [2]. There are two main loss mechanisms that have not been included in these models, which are expected to affect detrimentally the accuracy of their predictions [2], in particular with respect to efficiency. The first is a shuttle loss, where there is a loss of exergy arising from the irreversible alternating heat transfer between the working fluid and the solid walls of the power cylinder. The second are entrance and retrograde condensation losses where there is a loss of exergy due to the alternative parasitic condensation and re-evaporation of the working fluid vapour onto the inner walls and surfaces of the vapour region. These losses have been incorporated into the NIFTE models and a parametric study is carried out and presented in Chapter 4.

The studies that have been carried out thus far on the NIFTE have involved investigating changes in

the configuration of the device, whilst keeping the variables associated with the working fluid constant, that is the saturation data of *n*-pentane at atmospheric conditions (1 atm). In recent years, there have been numerous publications on working fluid selection for Organic Rankine Cycles (ORCs) [45–48]. A review on 35 working fluids for ORCs presented by Chen et al. showed that there are no best working fluids for different heat source temperatures. However, the critical temperature of the fluid and the slope of the vapour saturation curve of the fluid are important criteria to take into account when determining the type of cycle and operating temperature of the fluid. A study on the fluid selection for an ORC in a biomass power and heat plant has been carried out by Drescher and Brüggerman. Contrary to other low-grade heat driven ORCs, a higher maximum process temperature of 600 K is defined in this study, where the best working fluids were found to be in the alkylbenzene family [47]. A study carried out by Madhawa Hettiarachchi et al. investigated four working fluids for the use in an ORC with low-temperature (70 °C - 100 °C) geothermal heat sources. Here, ammonia was found to be the optimal working fluid for a cost-effective ORC, though PF5050 was found to have better physical and chemical characteristics.

Following the selection of the recommended model for the NIFTE, 31 working fluids are selected from Chen et al. [45]. For a given NIFTE configuration and a number of different operating conditions, a study to determine the best working fluid is carried out. In addition to this, the effect of different thermodynamic properties on the exergetic efficiency of the NIFTE is investigated. This is presented in Chapter 5.

2 Model Development for the NIFTE

In Chapter 1, the method by which the NIFTE was modelled by Smith[2, 34, 35] is discussed. In this chapter, this modelling method is looked at in further detail and extended to develop novel models for the NIFTE. The models shown here have been published in some detail in Refs. [49–52].

2.1 Electrical analogies

The basic foundation of the method by which the NIFTE is modelled stems from the use of electrical analogies to describe a device. Electrical analogies have been used in a number of research fields, including the analysis of the permeation in a dense metal membrane [37], simulation of mass and charge transport in lithium-ion batteries [38] and the modelling of water transport in xylem [39]. Much work has been carried out in laying the foundation for electrical analogies, such as the basic analogies between electrical, mechanical, acoustical, magnetic and electrical systems is given is published by Harry F. Olson [40]. A more in depth look into the usee of electrical analogies for acoustical systems, which was published by Swift [33].

Electrical analogies have been used in modelling thermoacoustic devices [25, 41, 42], whereby the analogies are made between the linearised, spatially lumped governing equations for thermal and fluid transport, and descriptions of linear, passive electrical components. Backhaus et al. and Huang et al. noted that this method is good at capturing the first-order dynamics in the devices, however the nonlinear effects could not be captured.

The first model developed for the NIFTE, presented by Smith [2], uses an extension of this approach, which includes the phase-change heat transfer processes that occur over the heat exchangers and a description of the exergetic losses due to irreversible heat transfer across the temperature difference between the

working fluid and the heat exchangers. The models presented in this chapter are developed in the same manner as the original models presented in Ref. [2].

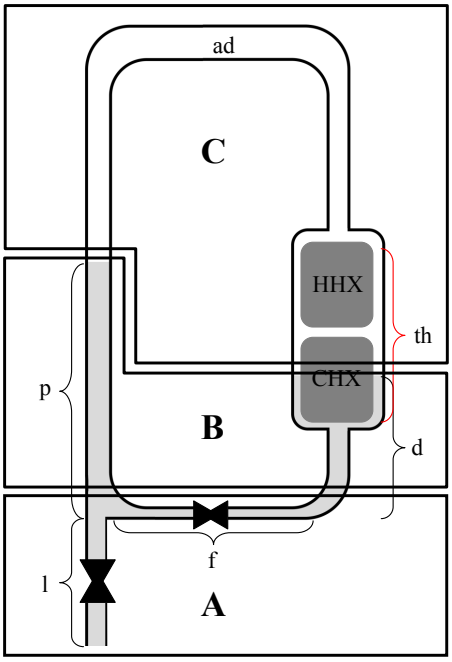


Figure 2.1: Schematic diagram of the NIFTE, indicating the three sub-model sections: **A**, where viscous friction and pressure drag, plus liquid flow inertia dominate in the feedback connection (f) and load line (l); **B**, where gravity/hydrostatic effects plus liquid flow inertia dominate in the power (p) and displacer (d) cylinders; and **C**, where vapour compressibility dominates in the adiabatic vapour volume (ad).

The first step in the development of a model for the NIFTE device requires the identification of a number of sections (spatial regions) within which well-defined, specific thermal and fluid processes are undergone. In this work, the regions denoted by the subscripts in Fig. 1.7 and Fig. 2.1 are identified, namely: (i) the regions in the power ('p') and displacer ('d') cylinders that are occupied by the working fluid in the liquid phase (Section B in Fig. 2.1); (ii) the *nominally* adiabatic vapour region ('ad') above these two regions that is occupied by the vapour phase (Section C in Fig. 2.1); (iii) the thermal domain ('th') that comprises the hot and cold heat exchanger blocks; (iv) the connecting feedback line and valve ('f'; Section A in Fig. 2.1); and (v) the load ('l') at the lower end of the device (Section A in Fig. 2.1) where the engine does useful hydraulic work (pumping and circulation), which strictly speaking is external to the NIFTE device itself, but nevertheless is included in the models due to its importance in affecting the behaviour and performance

of the device.

The above identification requires that each section is characterised by a single dominant thermal or fluid transport process. The aim is then to develop linearised and spatially lumped sub-models that describe the dynamic thermal or fluid processes undergone within each domain. The linearisation of a governing equation for a thermal or fluid transport process allows for a comparison to be made with linear, passive electrical components, that is: resistors (R), inductors (L) and capacitors (C).

In a final stage the sub-models of the various regions are connected together in a network that describes the complete NIFTE device. The interconnections between the sub-models that are represented by these electrical components lead to the construction of an analogue electrical (RLC) circuit representing the NIFTE engine. This is the approach that has been employed in the previous related work on the NIFTE [2, 34, 35, 43]).

2.2 Electrical components: resistors, capacitors and inductors

Each electrical component in the NIFTE RLC circuit represents a sub-model (i.e. region) of the NIFTE device, whereby: (i) resistors describe heat transfer and viscous effects (both associated with pure exergetic dissipation and loss); (ii) capacitors describe gravitational and vapour compressibility effects; and (iii) inductors describe the inertia experienced by the oscillating liquid flow. This approach requires analogies to be made between the physical domain and the electrical domain. As such, a pressure (P_i) difference across a physical NIFTE device component in the fluid domain, in region 'i' (e.g. i = f, l, d, p, ad), is represented by a voltage (E_i) difference across an equivalent analogous electrical component, while the volumetric flow-rate (U_i) through the same physical component is represented by the current (I_i) flowing through the corresponding electrical component. Similarly in the thermal domain, in region 'i' (e.g. th, hx), a temperature (T_i) difference across a physical NIFTE component is represented by a voltage (E_i) drop across an equivalent electrical component, and the resulting entropy flow ($\dot{S}_i$) through the physical component is represented by a current (I_i) flowing through the electrical component.

Now, the dynamic equation describing a pure resistor R_i is given by Ohm's law,

$$E_i \equiv R_i I_i \,, \tag{2.1}$$

where the voltage across the resistor E_i is directly proportional to the current running through it I_i. The dynamic equation describing an inductor L_i arises from Faraday's law of induction as,

$$E_i \equiv L_i \frac{\mathrm{d}I_i}{\mathrm{d}t} \Longrightarrow E_i = sL_iI_i\,, \tag{2.2}$$

where right-hand side expression in Eq. (2.2) shows the governing equation for an inductor in the Laplace domain, and the Laplace variable s represents a time derivative. Finally, the dynamic equation describing a capacitor C_i is derived from Gauss's law as,

$$\frac{\mathrm{d}E_i}{\mathrm{d}t} \equiv \frac{I_i}{C_i} \Longrightarrow E_i = \frac{1}{sC_i}I_i\,, \tag{2.3}$$

where the right-hand side expression shows the Laplace domain governing equation for a capacitor.

As mentioned previously, two domains in the physical device are considered when modelling the NIFTE: the fluid domain and the thermal domain. The sub-models that are built in these domains are described below, in Sections 2.3.1 and 2.3.2, respectively.

2.3 Model development

2.3.1 Fluid domain

In this section, the sub-models describing the fluid domain of the NIFTE are discussed. The device is split into three sections, highlighted in Fig. 2.1: (A) the feedback and load tubes; (B) the displacer and power cylinders; and (C) the nominally adiabatic vapour volume.

Section A: Feedback connection and load line

Resistance:

First consider Section A in Fig. 2.1, which involves liquid flow through the feedback connection and the load line. In both cases these components feature pipes and, possibly, valves. The total pressure (or, head) losses in pipe flows can be split into two categories: 'major head' losses due to viscous dissipation in the pipe flow, and 'minor head' losses from pipe components such as valves [53].

It is assumed that the NIFTE operates under quasi-steady conditions, which is a reasonable approximation for viscous flow in a smooth pipe at laminar Reynolds numbers *Re* and low Womersley parameters *Wo* (i.e. low frequencies) [54, 55]. Under this assumption the viscous losses (major head losses) can be derived from the Darcy equation for fully developed, steady laminar flow. Here, the model is based on the NIFTE prototype described in Refs. [2, 34, 35], for which experimental data are available for model validation purposes. In this case, the major head losses due to pipe friction are taken into account. The pressure drop across the feedback tube (ΔP_f) is directly related to the velocity of the fluid flow (u_f) though it by the drag coefficient C_D, given by,

$$C_D = \frac{\Delta P_\mathrm{f}}{\frac{1}{2}\rho_\mathrm{wf} u_\mathrm{f}^2}, \tag{2.4}$$

where ρ_wf is the density of the working fluid in the liquid phase. In a laminar flow regime, the drag coefficient can be given by the Darcy-Weisbach factor such that $C_D = 64/\mathrm{Re}$. Here, Re is the Reynolds number which is defined as $\mathrm{Re} = \rho_\mathrm{wf} u_\mathrm{f} d_\mathrm{f}/\mu_\mathrm{f}$, where d_f is the diameter of the feedback tube and μ_wf is the viscosity of the working fluid in the liquid phase. Substituting these two relations into Eq. (2.4) results in the Hagen-Poiseille equation relating the pressure drop to the volumetric flow rate U_f ($=u_\mathrm{f}A_\mathrm{f} = \pi d_\mathrm{f} l_\mathrm{f}$), where l_f is the length of the feedback connection,

$$\Delta P_\mathrm{f} = \frac{128\mu_\mathrm{wf} l_\mathrm{f} U_\mathrm{f}}{\pi d_\mathrm{f}^4}. \tag{2.5}$$

Further, the NIFTE is a (periodic) oscillating device, so it is possible to represent all thermodynamic, heat and fluid flow quantities as the sum of a time-averaged component and a fluctuating component. For example, the volumetric flow-rate in the feedback line U_f is represented as,

$$U_\mathrm{f}(t) \equiv \overline{U}_\mathrm{f} + U'_\mathrm{f}(t)\,, \tag{2.6}$$

where $\overline{U}_\mathrm{f}$ is the time-averaged (mean) volumetric flow-rate and $U'_\mathrm{f}(t)$ is the fluctuation about this mean, such that the time average of the fluctuation is zero by definition, $\overline{U'_\mathrm{f}} = 0$.

At this point a number of simplifications and conventions that are made in the modelling procedure for the NIFTE are highlighted. Firstly, since the NIFTE is a purely oscillating (zero-mean) flow device, only

the fluctuating components of the time-varying quantities around their respective time-means (also referred to as the 'equilibrium' values) need be considered. Secondly, it is assume that all time-varying quantities exhibit only *small* perturbations around their respective time-means, e.g. $U'_{\mathrm{f}} \ll \overline{U}_{\mathrm{f}}$. Thirdly, for simplicity, the primes are dropped by convention from the notation, so here $U'_{\mathrm{f}}(t) \rightarrow U_{\mathrm{f}}(t)$.

Assuming there are only small perturbations and the pressure drop is taken to be the fluctuation, the ratio of the pressure fluctuation to the volumetric flow rate fluctuation is given by,

$$\frac{P_{\mathrm{f}}}{U_{\mathrm{f}}} = \frac{128\mu_{\mathrm{wf}} l_{\mathrm{f}}}{\pi d_{\mathrm{f}}^4}. \tag{2.7}$$

Comparing Eq. (2.7) to the characteristic equation for a resistor in Eq. (2.1), and using the aforementioned analogies between the fluid and the electrical domains, where pressure is represented by voltage and volumetric flow-rate is represented by current, the resistance (in the electrical domain) to flow through the feedback valve is,

$$R_{\mathrm{f}} \equiv \frac{P_{\mathrm{f}}}{U_{\mathrm{f}}} = \frac{128\mu_{\mathrm{wf}} l_{\mathrm{f}}}{\pi d_{\mathrm{f}}^4}. \tag{2.8}$$

The fluid flow through the load line can be dealt with in a similar way to the fluid flow through the feedback connection, such that the resistance to flow due to the valve in the load can be found from,

$$\frac{P_{\mathrm{l}}}{U_{\mathrm{l}}} = \frac{128\mu_{\mathrm{w}} l_{\mathrm{l}}}{\pi d_{\mathrm{l}}^4} \equiv R_{\mathrm{l}}, \tag{2.9}$$

where μ_{w} is the viscosity of the pumped fluid (in the case of the prototype, water), l_{l} is the length of the load tube and d_{l} is the cross-sectional area of the load tube. Therefore, the resistance due to flow through the load valve is $R_{\mathrm{l}} = 128\mu_{\mathrm{w}} l_{\mathrm{l}}/(\pi d_{\mathrm{l}}^4)$. In both R_{f} and R_{l} above, k_{v} is a dimensionless valve loss coefficient, which is a function of valve opening ξ.

Inductance:

In the first modelling attempt of the NIFTE [2] it was assumed that inertia, that is, the effect of fluid mass, is always negligible. This is a reasonable approximation in the limit of low Reynolds and Womersley flows. In fact, both Jayasinghe et al. [54] and Ünsal et al. [55] have shown directly, with suitable experiments, that at low oscillation frequencies this is an acceptable assumption. As a consequence the

dynamic relationship between the flow-rate U_i through a component i and the pressure drop P_i across the component can be described by a resistor R_i, as discussed above. However, Jayasinghe et al. [54] and Ünsal et al. [55] have also shown that with increasing frequency f the effects of inertia become increasingly important in determining the flow behaviour, and that this appears in the form of a first-order decay in the ratio of magnitudes $|U_i/P_i|$ (i.e. $\sim 1/f$, or -20 dB per decade), and a corresponding first-order (i.e. 90 ° maximum) phase-lead in the impedance defined between the pressure and the flow-rate $Z_i = P_i/U_i$. Therefore, an inductive component (in conjunction with a resistor) is necessary to account for these changes in the relationship between U_i and P_i.

The inertial (inductive) contributions can be introduced via Newton's second law of motion, which states that a net resultant force F_f on a body of constant mass m_f is equal to the rate of change of its linear momentum. Thus, for the liquid in the feedback tube one can write,

$$F_\mathrm{f} = \frac{m_\mathrm{f}}{A_\mathrm{f}} \frac{\mathrm{d}U_\mathrm{f}}{\mathrm{d}t}\,, \tag{2.10}$$

where the mass of fluid in the feedback m_f is assumed to remain constant with time.

In order to relate Eq. (2.10) to electrical components, this equation is written in terms of pressure,

$$P_\mathrm{f} = \frac{F_\mathrm{f}}{A_\mathrm{f}} = \frac{\rho_\mathrm{wf} l_\mathrm{f}}{A_\mathrm{f}} \frac{\mathrm{d}U_\mathrm{f}}{\mathrm{d}t} \equiv L_\mathrm{f} \frac{\mathrm{d}U_\mathrm{f}}{\mathrm{d}t} = sL_\mathrm{f} U_\mathrm{f}\,, \tag{2.11}$$

where l_f is the length of the feedback tube occupied by liquid. Comparing Eq. (2.11) to the characteristic equation for an inductor in Eq. (2.2), making the same analogies between the fluid domain and electrical domain, the inductance due to inertia in the feedback tube is $L_\mathrm{f} = \rho_\mathrm{wf} l_\mathrm{f}/A_\mathrm{f}$.

Similarly, the inertia of the liquid in the load line is given by,

$$P_\mathrm{l} = \frac{\rho_\mathrm{w} l_\mathrm{l}}{A_\mathrm{l}} \frac{\mathrm{d}U_\mathrm{l}}{\mathrm{d}t} \equiv L_\mathrm{l} \frac{\mathrm{d}U_\mathrm{l}}{\mathrm{d}t} = sL_\mathrm{l} U_\mathrm{l}\,, \tag{2.12}$$

where l_l is the length of the load tube. Therefore, the inductance due to inertia in the load is $L_\mathrm{l} = \rho_\mathrm{w} l_\mathrm{l}/A_\mathrm{l}$.

Total impedance:

Since the (by definition *linear*) resistance R_f and inductance L_f that govern the dynamic relationship between U_f and P_f in the feedback connection act simultaneously on the same body of fluid, these are placed in series with each other as an impedance $Z_\mathrm{f} = R_\mathrm{f} + sL_\mathrm{f} = R_\mathrm{f} + \mathrm{j}\omega L_\mathrm{f}$ in the electrical circuit representation of the NIFTE, as shown in Fig. 2.4. Here, $s = \mathrm{j}\omega$ is the Laplace variable. This configuration is supported by results from Jayasinghe et al. [54] and also Ünsal et al. [55], where the oscillating fluid flow through a pipe resembled the behaviour of a resistor in series with an inductor. Similarly with the feedback connection, the resistance R_l and inductance L_l in the load line are placed in series with each other as an impedance $Z_\mathrm{l} = R_\mathrm{l} + sL_\mathrm{l} = R_\mathrm{l} + \mathrm{j}\omega L_\mathrm{l}$, again as shown in Fig. 2.4.

Section B: Displacer and power cylinders

Capacitance:

Consider Section B in Fig. 2.1, which relates to the fluid flow in the displacer ('d') and power ('p') cylinders, and in particular the hydrostatic pressure (weight due to gravity) and inertial forces acting on the two vertical liquid columns (also, 'liquid pistons'). In Ref. [54] the quasi-steady approximation was shown to be valid for oscillating flow in a U-tube at low frequencies.

In these conditions, the hydrostatic (gauge) pressure at the bottom of the displacer cylinder P_d can be approximated to first order by,

$$P_\mathrm{d} = \rho_\mathrm{wf} g \frac{V_\mathrm{d}}{A_\mathrm{d}}\,, \tag{2.13}$$

for a for a given volume of liquid in the displacer cylinder V_d. Here, g is the gravitational acceleration constant and A_d is the cross-sectional area of the displacer cylinder. To form an equivalence to electrical components, Eq. (2.13) is differentiated with respect to time,

$$\frac{\mathrm{d}P_\mathrm{d}}{\mathrm{d}t} = sP_\mathrm{d} = \frac{\rho_\mathrm{wf} g}{A_\mathrm{d}} \frac{\mathrm{d}V_\mathrm{d}}{\mathrm{d}t} = \frac{\rho_\mathrm{wf} g}{A_\mathrm{d}} U_\mathrm{d}\,, \tag{2.14}$$

where U_d is the volumetric flow-rate into the displacer cylinder from the feedback connection. Now, comparing Eq. (2.14) to the governing equation for a capacitor in Eq. (2.3),

$$\frac{\mathrm{d}P_\mathrm{d}}{\mathrm{d}t} = sP_\mathrm{d} = \frac{1}{C_\mathrm{d}} U_\mathrm{d}\,, \tag{2.15}$$

the capacitance due to hydrostatic effects in the displacer cylinder is $C_\mathrm{d} = A_\mathrm{d}/\rho_\mathrm{wf} g$.

Similarly, the fluid flow in the power cylinder can be expressed by a second capacitor,

$$\frac{\mathrm{d}P_\mathrm{p}}{\mathrm{d}t} = sP_\mathrm{p} = \frac{\rho_\mathrm{wf} g}{A_\mathrm{p}} U_\mathrm{p} = \frac{1}{C_\mathrm{p}} U_\mathrm{p}\,, \tag{2.16}$$

where P_p is the hydrostatic (gauge) pressure at the bottom of the power cylinder and U_p is the volumetric flow-rate into the power cylinder from the load line and the feedback connection. The capacitance in the power cylinder is thus given by $C_\mathrm{p} = A_\mathrm{p}/\rho_\mathrm{wf} g$, with A_p the cross-sectional area of the cylinder.

Inductance:

In addition to hydrostatic pressure, since the displacer and power cylinders contain a quantity of working fluid which is in the liquid phase, the inertia of this liquid region must be taken into account. Following from the inertial term developed for the feedback tube, given in Section 2.3.1, an equivalent inertial term for the liquid flow in the displacer cylinder can be found from,

$$P_\mathrm{d} = \frac{\rho_\mathrm{wf} l_\mathrm{d}}{A_\mathrm{d}} \frac{\mathrm{d}U_\mathrm{d}}{\mathrm{d}t} = s\frac{\rho_\mathrm{wf} l_\mathrm{d}}{A_\mathrm{d}} U_\mathrm{d}\,, \tag{2.17}$$

where l_d is the length of the displacer cylinder. Hence, the inductance due to inertia in the displacer cylinder is found to be $L_\mathrm{d} = \rho_\mathrm{wf} l_\mathrm{d}/A_\mathrm{d}$. The combined (linear) contributions of hydrostatic pressure and inertial forces in the displacer cylinder are superimposed by placing the capacitor and inductor in series, as shown in Fig. 2.4.

Similarly, the inertia in the power cylinder is given as,

$$P_\mathrm{p} = \frac{\rho_\mathrm{wf} l_\mathrm{p}}{A_\mathrm{p}} \frac{\mathrm{d}U_\mathrm{p}}{\mathrm{d}t} = \frac{\rho_\mathrm{wf} l_\mathrm{p}}{A_\mathrm{p}} sU_\mathrm{p}\,, \tag{2.18}$$

where l_p is the length of the power cylinder, and the inductance due to inertia in the power cylinder is given as $L_\mathrm{p} = \rho_\mathrm{wf} l_\mathrm{p}/A_\mathrm{p}$.

As a final note, it is emphasised that the pressure and flow-rate terms appearing Eqs. (2.15) to 2.18 are also defined as fluctuations around time-mean, equilibrium values. The equilibrium flow-rate is zero-mean by definition, while the equilibrium pressure is defined at a symmetric datum (vertical height) that passes

though the mid-height between the HHX and CHX, illustrated in Fig. 1.7(a).

Section C: Nominally adiabatic vapour volume

In Section C of Fig. 2.1, the (nominally) adiabatic vapour volume can be seen. Assuming the processes undergone by the working fluid (in the vapour phase) in this volume are adiabatic and reversible (i.e. isentropic), the vapour compression and expansion of this volume can be described by,

$$P_{\mathrm{ad}} V_{\mathrm{ad}}^{\gamma} = \text{constant}\,, \tag{2.19}$$

where P_{ad} and V_{ad} are the time-varying pressure and volume of the vapour, respectively, and γ is the heat capacity ratio of the working fluid. As in Eq. (2.6), the pressure and volume can be expressed as the sum of the time-averaged mean and the fluctuation about this mean, i.e. $P_{\mathrm{ad}} = \overline{P}_{\mathrm{ad}} + P'_{\mathrm{ad}}$ and $V_{\mathrm{ad}} = \overline{V}_{\mathrm{ad}} + V'_{\mathrm{ad}}$. Assuming there are only small fluctuations and taking the time derivative of Eq. (2.19),

$$\frac{1}{\overline{P}_{\mathrm{ad}}} \frac{\mathrm{d}P_{\mathrm{ad}}}{\mathrm{d}t} + \frac{\gamma}{\overline{V}_{\mathrm{ad}}} \frac{\mathrm{d}V_{\mathrm{ad}}}{\mathrm{d}t} = 0\,. \tag{2.20}$$

The time-averaged pressure is taken to be the equilibrium pressure, P_0, and time-averaged volume is taken to be the equilibrium volume, $V_{\mathrm{g},0}$, such that $P_0 \equiv \overline{P}_{\mathrm{ad}}$ and $V_{\mathrm{g},0} \equiv \overline{V}_{\mathrm{ad}}$, and,

$$\frac{\mathrm{d}P_{\mathrm{ad}}}{\mathrm{d}t} = sP_{\mathrm{ad}} = \frac{\gamma P_0}{V_{\mathrm{g},0}} U_{\mathrm{ad}} = \frac{1}{C_{\mathrm{ad}}} U_{\mathrm{ad}}\,, \tag{2.21}$$

where U_{ad} is the rate of *reduction* of the adiabatic vapour volume, or the *net* volumetric flow-rate *into* the adiabatic vapour volume, defined as $-\mathrm{d}V_{\mathrm{ad}}/\mathrm{d}t$. Comparing Eq. (2.21) to the equation for a capacitor in Eq. (2.3), the capacitance due to adiabatic compression/expansion is $C_{\mathrm{ad}} = V_{\mathrm{g},0}/\gamma P_0$.

2.3.2 Thermal domain

In this section the focus is on the thermal domain contributions to the NIFTE models. The only model for the NIFTE that has been presented thus far has been the linear temperature profile (LTP) model by Smith. Here, the thermal contributions for the LTP model, in addition to two alternative models with different governing heat exchange expressions; the constant heat exchanger (CHX) and dynamic heat exchanger

(DHX) models are developed.

Domain coupling

To link the thermal domain processes to the ones taking place in the fluid domain (described in Section 2.3.1), two coupling equations are required; one between entropy flow and volumetric flow, and the other between temperature and pressure. The large change in density that takes place during phase change leads to the following coupling equation between the entropy flow $\dot{S}_{\mathrm{th}}$ and volumetric flow-rate U_{th},

$$\dot{S}_{\mathrm{th}} \approx \rho_{\mathrm{g},0} \Delta s_{\mathrm{fg}} U_{\mathrm{th}} \,, \tag{2.22}$$

where $\rho_{\mathrm{g},0}$ is the time-averaged density of the working fluid in the vapour phase and Δs_{fg} is the entropy change due to vapourisation.

Further, assuming that the thermal processes are governed by phase change with small perturbations about a certain time-mean saturation temperature T_0 (and pressure P_0), the coupling equation between temperature and pressure is,

$$T_i = \left(\frac{\mathrm{d}T}{\mathrm{d}P}\right)_{\mathrm{sat}} P_i \,, \tag{2.23}$$

where $(\mathrm{d}T/\mathrm{d}P)_{\mathrm{sat}}$ is the change in temperature with pressure along the saturation curve of the working fluid about the equilibrium point, found from the Clausius-Clapeyron relation.

Linear temperature profile (LTP)

In order to model the heat transfer process occurring in the heat exchangers, a linear temperature profile model can be used [2]. In this model it is assumed that the heat transfer is governed by convective heat transfer [56], for which all heat transferred $\dot{Q}$, goes into the phase change of the working fluid with an associated entropy flow-rate $\dot{S}_{\mathrm{th}}$,

$$\frac{\dot{Q}}{T_0} = \dot{S}_{\mathrm{th}} = \frac{hA_{\mathrm{s}}}{T_0} \left(T_{\mathrm{hx}} - T_{\mathrm{ad}}\right) \,, \tag{2.24}$$

where h is the convective heat transfer coefficient, A_{s} is the surface area of the heat exchanger blocks involved in the phase-change heat transfer, T_{ad} is the temperature of the working fluid and T_{hx} is the temperature of the heat exchangers. As before, T_0 is the time-averaged, saturation temperature for the working

fluid, about which the temperatures fluctuate. This temperature is assumed to be equal to the mean temperature of the hot and cold heat exchangers, as well as the time-averaged temperature of the working fluid in the vapour phase, such that $T_0 \equiv \overline{T}_{\mathrm{hx}} = \overline{T}_{\mathrm{ad}}$.

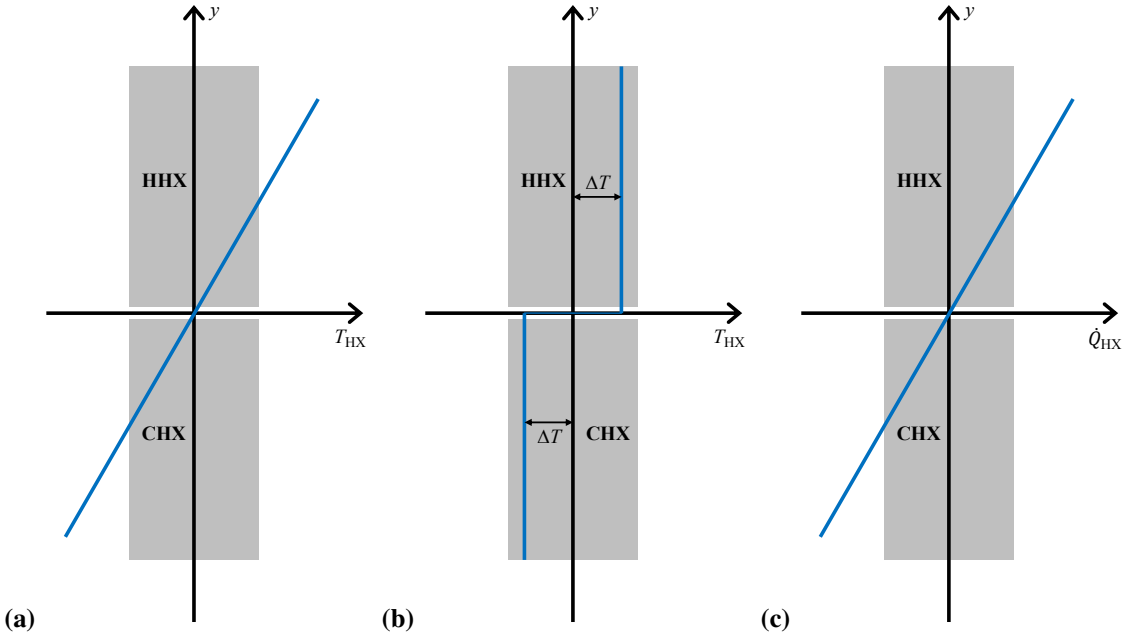


Figure 2.2: The temperature or power gradient along the hot heat exchanger (HHX) and cold heat exchanger (CHX) assumed in the (a) LTP, (b) CTD and (c) DHX models for the NIFTE device, where T_{HX} is the temperature at the surface of the heat exchanger block, ΔT is the temperature difference between the surface of the heat exchangers and the working fluid and $\dot{Q}_{\mathrm{HX}}$ is the power input to the heat exchanger blocks.

Now, substituting the two coupling equations that link the thermal domain to the fluid domain, Eq. (2.22) and (2.23), into the heat transfer equation, Eq. (2.24) in the fluid domain is written,

$$P_{\mathrm{th}} - P_{\mathrm{ad}} = \frac{\rho_{\mathrm{g},0} T_0 \Delta s_{\mathrm{fg}}}{h A_{\mathrm{s}} (\mathrm{d}T/\mathrm{d}P)_{\mathrm{sat}}} U_{\mathrm{th}} = R_{\mathrm{th}} U_{\mathrm{th}} \,. \tag{2.25}$$

Comparing Eq. (2.25) to the equation for a resistor, Eq. (2.1), the heat exchanger thermal resistance in the LTP model is $R_{\mathrm{th}} = \rho_{\mathrm{g},0} T_0 \Delta s_{\mathrm{fg}} / h A_{\mathrm{s}} (\mathrm{d}T/\mathrm{d}P)_{\mathrm{sat}}$.

In addition to this, the LTP model [2, 34, 35, 43] imposes a linear temperature profile along the heat exchangers, that is, the temperature on the walls of the heat exchangers T_{hx} is assumed to vary linearly with (and thus, is proportional to) the height in the displacer cylinder y_{d} ($= P_{\mathrm{d}}/\rho_{\mathrm{wf}} g$), as shown in Fig. 2.2(a).

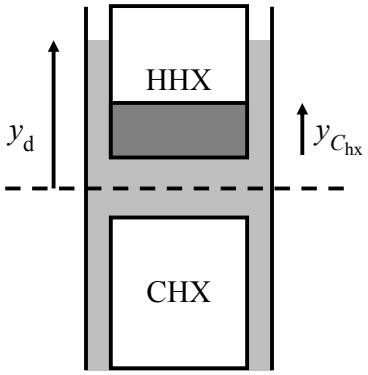


Figure 2.3: Close-up of the heat exchangers, where y_d is the vapour-liquid interface height in the displacer cylinder and $y_{C_{hx}}$ is the height of the heat exchangers that participates in heat exchange with the working fluid.

Recall that here, according to the convention used throughout, y_d is in fact the fluctuation of this height around its equilibrium level, which is indicated in Fig. 1.7.

Solution:

Firstly, using the equation for the thermal resistance in the heat exchangers, Eq. (2.25), and the relations in Section 2.3.1, an electrical circuit representing the linear temperature profile model (LTP) is developed. The electrical circuit network representing the inertive LTP NIFTE can be seen in Fig. 2.4(a).

At this stage a transfer function for the NIFTE, which relates an input to an output of the system [57], can be written in order to solve the system. The transfer function for the NIFTE can be found by considering the circuit in Fig. 2.4(a) and using Kirchoff's voltage and current laws [58]. In modelling the NIFTE, the input is taken to be P_{th}, which represents the pressure associated with the temperature of the heat exchangers T_{hx} ($= P_{th}(dT/dP)_{sat}$). The output is taken to be the pressure in the displacer cylinder P_d, which directly relates to the height of the vapour-liquid interface in the displacer cylinder, y_d ($= P_d/\rho_{wf}g$, refer Section 2.3.1). Hence, the forward-loop transfer function $G_{LTP}(s)$ for the LTP model is,

$$G_{LTP}(s) = -\frac{\alpha_{LTP}\beta_{LTP}\gamma_{LTP}}{1 + s^2 C_d L_d}\,, \tag{2.26}$$

where α_{LTP}, β_{LTP} and γ_{LTP} are four sub-systems, shown in Fig. 2.4(a), which are a function of the electrical component impedances and are given in Table 2.1.

In electrical circuits, the impedance for components placed in series with each other is given by $Z_{\mathrm{TOT,ser}} = \sum_i Z_i$, whereas the impedance for components placed in parallel is given by $Z_{\mathrm{TOT,par}}{}^{-1} = \sum_i Z_i^{-1}$, where Z_i is the impedance in section 'i' [58]. The total impedance of the circuit representing the LTP model (Fig. 2.4(a)), is required to determine the forward-loop transfer function in Eq. (2.26), and this is found from combining impedance contributions in series and parallel as appropriate, such that,

$$Z_{\mathrm{TOT,LTP}} \equiv P_{\mathrm{th}}/U_{\mathrm{th}} = R_{\mathrm{th}} + (sC_{\mathrm{ad}} + (Z_{\mathrm{l}} + ((Z_{\mathrm{f}} + Z_{\mathrm{d}})^{-1} + Z_p^{-1})^{-1})^{-1})^{-1}\,, \tag{2.27}$$

where $Z_{\mathrm{l}} = R_{\mathrm{l}} + sL_{\mathrm{l}}$, $Z_{\mathrm{p}} = sL_{\mathrm{p}} + 1/sC_{\mathrm{p}}$, $Z_{\mathrm{f}} = R_{\mathrm{f}} + sL_{\mathrm{f}}$ and $Z_{\mathrm{d}} = sL_{\mathrm{d}} + 1/sC_{\mathrm{d}}$, are the impedances associated with the load, power cylinder, feedback and displacer cylinder, respectively. These impedances are a function of the parameters defined in Table 2.2.

In order to close the set of equations and solve the system, an additional relation between the input P_{th} and output P_{d} is required. This feedback relation is demonstrated in Fig. 2.5. In the LTP, the feedback constant k_{LTP} is found from the imposed linear temperature gradient in the heat exchangers, such that $P_{\mathrm{th}} = k_{\mathrm{LTP}} P_{\mathrm{d}}$ (shown in Fig. 2.4(a)), where $k_{\mathrm{LTP}} = (\mathrm{d}T_{\mathrm{hx}}/\mathrm{d}y)/\rho_{\mathrm{wf}} g(\mathrm{d}T/\mathrm{d}P)_{\mathrm{sat}}$. Thus, it can be seen that the feedback gain k_{LTP} is proportional to the temperature gradient in the heat exchangers, $\mathrm{d}T_{\mathrm{hx}}/\mathrm{d}y$. At the point of marginal stability, that is the condition in a linear system at which continuous sustained oscillations are observed, the feedback gain will give an indication of the minimum temperature gradient in the heat exchangers required to achieve this state.

Constant temperature difference (CTD)

As in the LTP model, the heat transfer process in the constant temperature difference (CTD) model is governed by convective heat transfer. In addition it is assumed that there is a constant temperature difference between the working fluid and the heat exchanger block, as shown in Fig. 2.2(b), $\Delta T = T_{\mathrm{hx}} - T_{\mathrm{ad}}$, where as before T_{hx} is the wall temperature of the heat exchangers and T_{ad} is the temperature of the working fluid. This may be a reasonable assumption at low loads (and hence pressures). In this case the heat exchanger surface area $A_{\mathrm{s}}(y) = l_{\mathrm{c}} y$ that participates in heat transfer evolves with time as the liquid-solid contact area

varies with the position y of the vapour-liquid interface in the displacer cylinder, such that,

$$\frac{\dot{Q}}{T_0} = \dot{S}_{\mathrm{th}} = \frac{h\Delta T}{T_0} A_{\mathrm{s}}(y) = \frac{h\Delta T}{T_0}(l_{\mathrm{c}} y)\,, \tag{2.28}$$

where l_c is a (constant) circumferential length.

In the CTD model, a constant temperature difference between the temperature at the wall of the heat exchangers and the working fluid is imposed. Unlike in the LTP model, the surface area of the heat exchangers varies with the height of the displacer cylinder y_{d}.

Solution:

Contrary to the LTP mode, there are no thermal resistances in the CTD model, so using the relations in Section 2.3.1, an electrical circuit representing the constant temperature difference model (CTD) is developed. The electrical circuit network representing the inertive CTD NIFTE can be seen in Fig. 2.4(b).

The forward-loop transfer function in the CTD model, $G_{\mathrm{CTD}}(s)$, relating P_{th} (the pressure input representing the volumetric flow-rate in U_{th}) to output P_{d} is,

$$G_{\mathrm{CTD}}(s) = -\frac{\alpha_{\mathrm{CTD}}\beta_{\mathrm{CTD}}}{1 + s^2 C_{\mathrm{d}} L_{\mathrm{d}}}\,, \tag{2.29}$$

where α_{CTD}, and β_{CTD} are two sub-systems, shown in Fig. 2.4(b) and given in Table 2.1, which are a function of the electrical component impedances and are given in Table 2.2.

The total impedance of the circuit in Fig. 2.4(b) relating the input pressure P_{th} to the input flow-rate U_{th}, is obtained by adding contributions from all impedances in the circuit, similarly to the LTP model,

$$Z_{\mathrm{TOT,CTD}} \equiv P_{th}/U_{\mathrm{th}} = (sC_{\mathrm{ad}})^{-1} + (Z_{\mathrm{l}} + ((Z_{\mathrm{f}} + Z_{\mathrm{d}})^{-1} + Z_{\mathrm{p}}^{-1})^{-1})^{-1}\,. \tag{2.30}$$

The relation $P_{th} = k_{\mathrm{CTD}} P_d / s$ in Fig. 2.4(b) describes the heat transfer from the heat exchanger blocks as a function of the height of the vapour-liquid interface in the displacer cylinder, y. In this model $k_{\mathrm{CTD}} = hl_{\mathrm{c}}\Delta T/\rho_{\mathrm{pen}} g \rho_{\mathrm{g}} \Delta s_{\mathrm{vap}} T_0 C_{\mathrm{ad}}$ is a feedback constant, which is proportional to the temperature difference between the heat exchanger blocks and the working fluid, ΔT. Hence, the temperature difference found at marginal stability is the minimum required temperature difference to achieve continuous oscillations.

Dynamic heat exchanger (DHX)

In the DHX model, the ability of the heat exchangers to store and release energy dynamically as they interact with the working fluid that removes energy during evaporation and re-deposits energy during condensation, is taken into account. As in the LTP model, it is assumed that heat transfer to the fluid is governed by phase-change convective heat transfer, though some energy (per unit time) to/from the heat exchanger blocks $\dot{Q}_{\mathrm{hx}}$ is used in heating/cooling the heat exchanger blocks, such that,

$$\dot{Q}_{\mathrm{hx}} - m_{\mathrm{al}} c_{\mathrm{al}} \frac{\mathrm{d}T_{\mathrm{hx}}}{\mathrm{d}t} = hA_{\mathrm{s}} \left[T_{\mathrm{hx}}(y) - T_{\mathrm{ad}} \right] , \tag{2.31}$$

where m_{al} is the mass of the heat exchanger that participates in the heat transfer process, c_{al} is the specific heat capacity and T_{hx} is the wall temperature of the heat exchangers, assumed to be made of aluminium [2, 34]. As before, T_{ad} is the temperature of the working fluid. Using the coupling equations defined in Eqs. (2.22) and (2.23), Eq. (2.31) which is written in the thermal domain and in terms of thermal domain variables can be referred to the fluid domain,

$$\frac{\dot{Q}_{\mathrm{hx}}}{\rho_{\mathrm{g},0} T_0 \Delta s_{\mathrm{fg}}} = \frac{m_{\mathrm{al}} c_{\mathrm{al}} \left(\mathrm{d}T/\mathrm{d}P\right)_{\mathrm{sat}}}{\rho_{\mathrm{g},0} \Delta s_{\mathrm{fg}} T_0} \frac{\mathrm{d}P_{\mathrm{hx}}}{\mathrm{d}t} + \frac{hA_{\mathrm{s}} (\mathrm{d}T/\mathrm{d}P)_{\mathrm{sat}}}{\rho_{\mathrm{g},0} T_0 \Delta s_{\mathrm{fg}}} \left(P_{\mathrm{th}} - P_{\mathrm{ad}}\right) . \tag{2.32}$$

Now, comparing Eq. (2.32) to the equation for a resistor, Eq. (2.1), and for a capacitor, Eq. (2.3), the thermal resistance and the heat exchanger capacitance can be identified,

$$U_{\mathrm{th}} = \frac{1}{C_{\mathrm{hx}}} \frac{\mathrm{d}P_{\mathrm{hx}}}{\mathrm{d}t} + R_{\mathrm{th}} \left(P_{\mathrm{th}} - P_{\mathrm{ad}}\right) , \tag{2.33}$$

where it is noted that the thermal resistance in the DHX model R_{th}, found from the second term on the right-hand side of Eq. (2.32), remains the same as that identified in the LTP model. Furthermore, on comparing the first term in Eq. (2.32) to the equation for a capacitor, Eq. (2.3), the heat exchanger capacitance $C_{\mathrm{hx}} = m_{\mathrm{al}} c_{\mathrm{al}} \left(\mathrm{d}T/\mathrm{d}P\right)_{\mathrm{sat}} / \rho_{\mathrm{g},0} \Delta s_{\mathrm{fg}} T_0$ can be found, and is given in Table 2.2.

Thus, the DHX model introduces an ability for the heat exchangers to interact dynamically with the phase change of the working fluid in an effort to more accurately predict the behaviour of the NIFTE. The value of C_{hx} depends on the mass m_{al} of the heat exchangers that participates in the heat transfer

process, that is, the mass of the heat exchangers whose temperature changes significantly during operation. It is emphasised that the section of the heat exchangers that takes part in this process (height $y_{C_{\mathrm{hx}}}$) is not the same as the extent that is washed periodically by the liquid phase (height y_{d}), although it is expected that the two will be strongly related (refer to Fig. 2.3(b)). From Ref. [1] it is known by direct video observation of the NIFTE demonstrator during operation that the amplitude of the vapour-liquid interface in the displacer cylinder $\hat{y}_{\mathrm{d}}$ is about 9 mm. Now, and referring again to Fig. 2.3(b), the gap between the heat exchanger blocks was stated in Ref. [2] as being of the order of a few mm (in fact, 3 – 4 mm), and this was also measured in Ref. [1] and confirmed as being $\sim$ 4 mm. Taking a half-gap size of 2 mm, the 9 mm displacer cylinder amplitude $\hat{y}_{\mathrm{d}}$ corresponds to an overlap height over the heat exchanger blocks $\hat{y}_{C_{\mathrm{hx}}}$ of about 7 mm [1].

The solution of the DHX model, as defined by the heat exchange relation in Eq. (2.32), requires the heat (equivalent to a current) source term $\dot{Q}_{\mathrm{hx}}$ (or, its equivalent $U_{\mathrm{th}} \equiv \dot{Q}_{\mathrm{hx}}/\rho_{\mathrm{g},0}T_0\Delta s_{\mathrm{fg}}$) to be prescribed. In this work a heat (current) input is imposed into the heat exchangers that is proportional to the overlap height of liquid over the heat exchangers, i.e. that is proportional to y_{d} (= $P_{\mathrm{d}}/\rho_{\mathrm{wf}}g$).

Solution:

An electrical circuit representing the DHX model can be formed by converting from a current input system to a voltage input system using the Norton-Thévenin theorem, and using the relations developed in Section 2.3.1. The conversion creates the voltage source $P_{\mathrm{th}} = k_{\mathrm{DHX}}P_{\mathrm{d}}/s$, which includes the feedback constant k_{DHX}. The circuit is shown in Fig. 2.4(c).

The forward-loop transfer function in the DHX model, $G_{\mathrm{DHX}}(s)$, relating P_{th} (the pressure input representing the volumetric flow-rate in U_{th}) to output P_{d} is,

$$G_{\mathrm{DHX}}(s) = -\frac{\alpha_{\mathrm{DHX}}\beta_{\mathrm{DHX}}\gamma_{\mathrm{DHX}}}{1 + s^2 C_{\mathrm{d}} L_{\mathrm{d}}}\,, \tag{2.34}$$

where α_{DHX}, β_{DHX} and γ_{DHX} are three sub-systems, shown in Fig. 2.4(c), which are a function of the electrical component impedances and are given in Table 2.1.

For this model, the total impedance is,

$$Z_{\mathrm{TOT,DHX}} \equiv \frac{P_{\mathrm{th}}}{U_{\mathrm{th}}} = R_{\mathrm{th}} + (sC_{\mathrm{hx}})^{-1} + (Z_{\mathrm{TL}}{}^{-1} + ((sC_{\mathrm{ad}} + (Z_{\mathrm{l}} + ((Z_{\mathrm{f}} + Z_{\mathrm{d}})^{-1} + Z_{\mathrm{p}}{}^{-1})^{-1})^{-1})^{-1})^{-1})^{-1}\,. \tag{2.35}$$

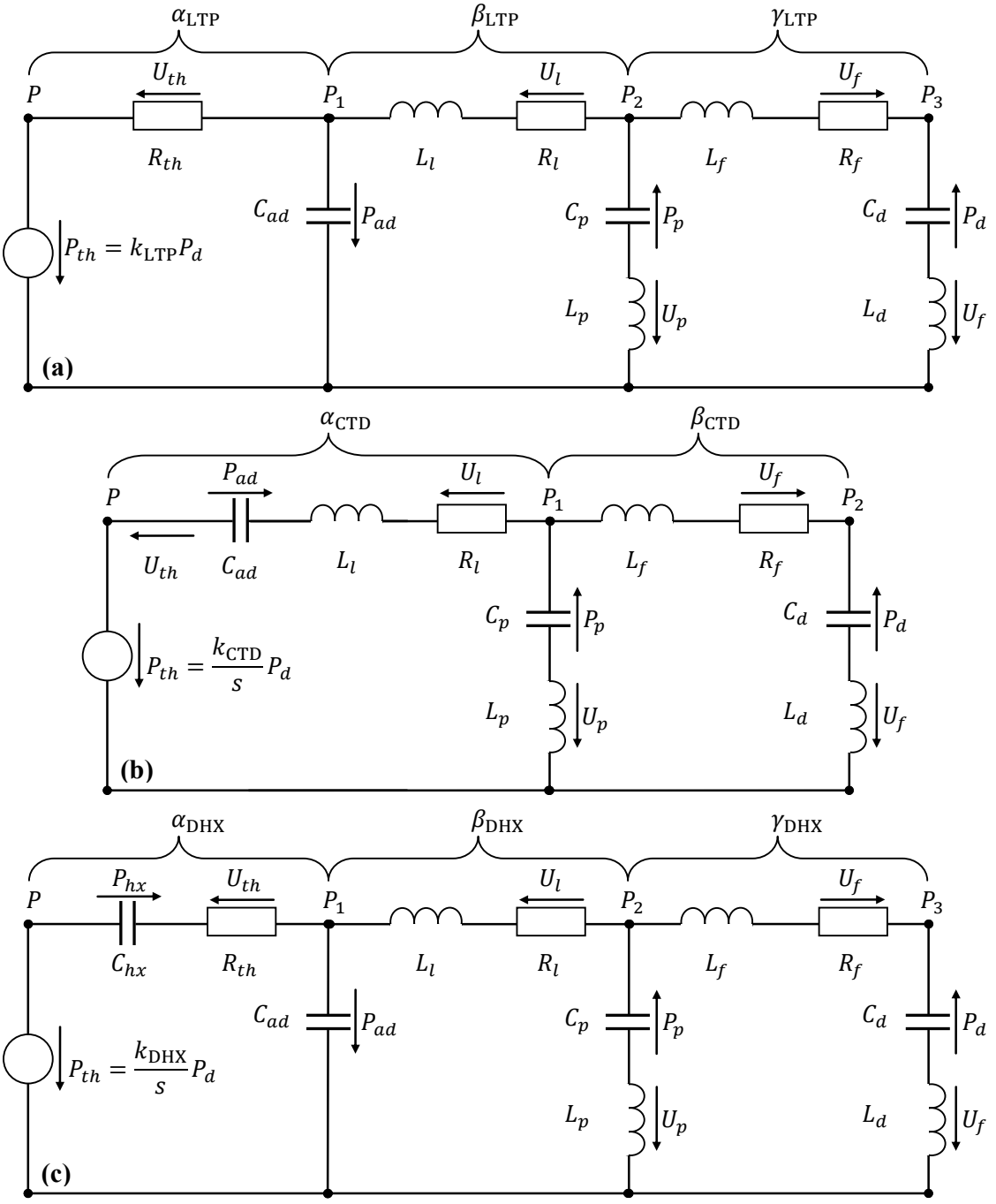


Figure 2.4: Electrical circuit representation of the NIFTE (refer to Fig. 1.7) for the: (a) LTP, (b) CTD, and (c) DHX models. Here, k_j corresponds to the feedback gain for model 'j', R_i to a resistance, C_i to a capacitance, L_i to an inductance, P_i to a pressure and U_i to a volumetric flow-rate. Subscript 'hx' denotes the heat exchangers, 'th' the thermal domain, 'ad' the adiabatic domain, 'l' the load, 'p' the power cylinder, 'd' the displacer (heat exchanger) cylinder, and 'f' the feedback connection.

As with the LTP and CTD, the solution of the DHX model requires an additional relation between P_{th} and P_{d}. In the DHX model, the feedback gain k_{DHX} appearing in the feedback relation $P_{\text{th}} = k_{\text{DHX}} P_{\text{d}}/s$ is given by $k_{\text{DHX}} = (\text{d}\dot{Q}_{\text{hx}}/\text{d}y)/\rho_{\text{wf}} g \rho_{\text{g},0} \Delta s_{\text{fg}} T_0 C_{\text{hx}}$. It can be seen that the feedback gain is proportional to the power gradient in the heat exchangers, $\text{d}\dot{Q}_{\text{hx}}/\text{d}y$. At the point of marginal stability, the feedback gain in DHX model gives an indication of the minimum power required to achieve sustained oscillations.

Table 2.1: Transfer functions for the three models (LTP, CTD and DHX) in Fig. 2.4(a), (b) and (c)

	$\alpha = P_1/P$	$\beta = P_2/P_1$	$\gamma = P_3/P_2$
LTP	$1 - R_{\text{th}}/Z_{\text{TOT,LTP}}$	$1 - Z_{\text{l}}(1/\alpha_{\text{LTP}} Z_{\text{TOT,LTP}} - sC_{\text{ad}})$	$1/(1 + Z_{\text{f}}/Z_{\text{d}})$
CTD	$1 - (Z_{\text{l}} + 1/sC_{\text{ad}})/Z_{\text{TOT,CTD}}$	$1/(1 + Z_{\text{f}}/Z_{\text{d}})$	—
DHX	$1 - (R_{\text{th}} + 1/sC_{\text{hx}})/Z_{\text{TOT,CTD}}$	$1 - Z_{\text{l}}(1/\alpha_{\text{DHX}} Z_{\text{TOT,DHX}} - sC_{\text{ad}})$	$1/(1 + Z_{\text{f}}/Z_{\text{d}})$

Table 2.2: Electrical analogies in the NIFTE and relations for resistances (R_i), capacitances (C_i) and inductances (L_i).

Electrical Element	**Thermal-Fluid Effect**	**Parameter Expression**
Resistance (R)	Thermal resistance	$R_{\text{th}} = \rho_{\text{g},0} T_0 \Delta s_{\text{vap}}/hA_{\text{s}}(\text{d}T/\text{d}P)_{\text{sat}}$
	Load flow resistance (viscous/pressure drag)	$R_{\text{l}} = 128\mu_{\text{w}} l_{\text{l}}/\pi d_{\text{l}}^4$
	Feedback valve flow resistance (drag)	$R_{\text{f}} = 128\mu_{\text{wf}} l_{\text{f}}/\pi d_{\text{f}}^4$
Capacitance (C)	Vapour compressibility	$C_{\text{ad}} = V_{\text{g},0}/\gamma P_0$
	Power cylinder hydrostatic capacitance	$C_{\text{p}} = A_{\text{p}}/\rho_{\text{wf}} g$
	Displacer cylinder hydrostatic capacitance	$C_{\text{d}} = A_{\text{d}}/\rho_{\text{wf}} g$
	Heat exchanger heat storage capacitance	$C_{\text{hx}} = m_{\text{al}} c_{\text{al}} (\text{d}T/\text{d}P)_{\text{sat}}/\rho_{\text{g},0} \Delta s_{\text{vap}} T_0$
Inductance (L)	Load inertia (fluid mass)	$L_{\text{l}} = \rho_{\text{w}} l_{\text{l}}/A_{\text{l}}$
	Power cylinder inertia	$L_{\text{p}} = \rho_{\text{wf}} l_{\text{p}}/A_{\text{p}}$
	Displacer cylinder inertia	$L_{\text{d}} = \rho_{\text{wf}} l_{\text{d}}/A_{\text{d}}$
	Feedback tube inertia	$L_{\text{f}} = \rho_{\text{wf}} l_{\text{f}}/A_{\text{f}}$

2.4 Oscillation frequency

The models presented Section 2.3.2 have each been defined with a forward-loop transfer function $G_i(s)$, for a given model i, which relates the input P_{th} to the output P_{d}. In addition, each model has a defined feedback constant k_i which again relates the input to the output, but in the opposite direction. A closed-loop transfer function can then be found for the NIFTE system, which can be used to find the operating state for a given set of parameters. The closed-loop representation of the NIFTE is shown in Fig. 2.5, from which

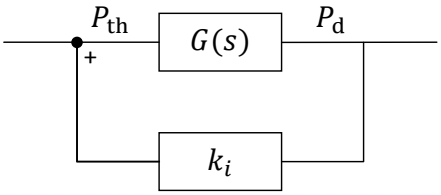


Figure 2.5: Closed-loop representation of the NIFTE where $G(s)$ is the modelled forward-loop transfer function between P_{th} and P_{d}, and k_i is the feedback gain for model 'i'.

the closed-loop transfer function $C(s)$ is defined as,

$$C(s) = \frac{G_i(s)}{1 - k_i G_i(s)} \,. \tag{2.36}$$

The forward-loop transfer functions $G_i(s)$ for the LTP, CTD and DHX models, found in Eqs. (2.26), (2.29) and (2.34), are dependent on the R, C and L parameters (from Table 2.2), and are also a function of the Laplace variable, s, which is a function of the frequency f_0 such that $s = \sigma \pm \mathrm{j}\omega_0 = \sigma \pm \mathrm{j}2\pi f_0$, where σ is a real number and ω_0 is the angular oscillation frequency.

For a given set of parameter values (R_i, C_i and L_i) and feedback gain (k_i) the poles of Eq.(2.36) are the values of s for which the denominator of Eq. (2.36) becomes equal to zero. These poles can be used to investigate the stability of the system. The poles take the form of $s = \sigma \pm \mathrm{j}\omega_0$, and can either be purely real (i.e. $\omega_0 = 0$), or appear as a complex conjugate pair. There are three types of dynamic response in a linear system: stable, unstable and marginally stable. In a stable system, which occurs when all poles have negative real parts ($\sigma < 0$), all oscillations decay exponentially. In an unstable system, which occurs when at least one pole has a positive real part ($\sigma > 0$), the oscillations grow exponentially.

The NIFTE operates with sustained oscillations with constant amplitude, which is best described as being marginally stable. A linear system becomes marginally stable when one pair of complex conjugate poles has a purely imaginary part (i.e. $\sigma = 0 \rightarrow s = \pm\mathrm{j}\omega_0$), and all remainder poles have negative real parts. The value of the point at which the poles cross the imaginary axis, ω_0, is the known as the marginal stability frequency. Any quantity of interest, for example the efficiency, in the model is evaluated at this condition (frequency).

2.5 Efficiency definitions

The efficiency of an engine is a key quantity against which its performance is evaluated and assessed. In order to investigate the effect of changing the working fluid on the efficiency of the NIFTE, three efficiency definitions are identified in this work: the ideal maximum 'working fluid' thermal efficiency (η_{wf}); along with the NIFTE exergy (η_{ex}) and thermal (η_{th}) efficiencies. Descriptions of these efficiency measures are given in the sections below.

2.5.1 Working fluid thermal efficiency (η_{wf})

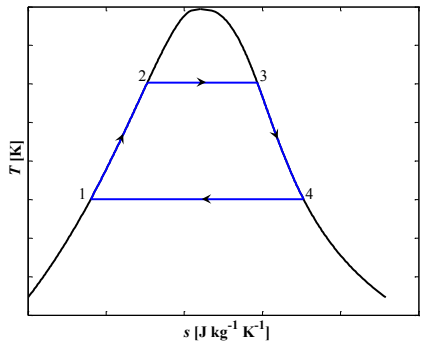


Figure 2.6: Thermodynamic cycle undergone by a wet working fluid associated with an ideal theoretical vapour-cycle engine without mechanical-shaft components that can only interface with a low-pressure reservoir and a high-pressure load, or a low-temperature sink and high-temperature source, imposed externally by a specific application, featuring the following processes: compression of the saturated liquid by sudden exposure to the high pressure reservoir/load conditions (States 1 to 2), reversible isobaric (and isothermal) heat addition (States 2 to 3), expansion of the saturated vapour by sudden discharge into the low pressure surrounding environment/atmospheric conditions (States 3 to 4), and reversible isobaric (and isothermal) heat rejection (States 4 to 1). The engine can only exchange heat and work during the processes involving positive-displacement phase-change of the working fluid (i.e. from States 2 to 3 and States 4 to 1).

The working fluid efficiency η_{wf} is a *theoretical* ideal (maximum) *thermal* efficiency that relates to the total useful work done by taking fluid from a low-pressure reservoir and pumping it into a high-pressure load during a positive-displacement phase-change process, ignoring any parasitic power dissipated (exergy destruction) in valves and exegetic losses incurred due to heat transfer across finite temperature differences in the thermal domain (heat exchangers, thermal losses). Consider an ideal device without mechanical-

shaft components that undergoes a thermodynamic vapour cycle during which work can only be extracted by positive displacement into the load due to phase change of the working fluid. This device undergoes processes at constant pressure and temperature which are imposed externally by the application, that is, either: (i) the high and low pressures are set by the load and the atmosphere, or (ii) the hot and cold temperatures are set by the heat source and sink, respectively. Thus, the ideal method by which heat can be added or rejected is by phase change at these constant pressure and temperature conditions. Further, there is no intermediate pressure or temperature reservoir that the device can interact with.

The ideal thermodynamic cycle from which the working fluid efficiency is determined is shown in Fig. 2.6. The most important thermodynamic processes are identified as those that take place between thermodynamic States 2 and 3, and States 4 and 1, where phase change (heat) and restricted volumetric changes (work) occur. No heat or work can be provided or extracted between States 1 and 2, or States 3 and 4, owing to the lack of suitable components and the sudden and unrestricted nature of the pressure-volume changes. The temperature changes during these processes are due to the pressure changes imposed on to the system due to the interaction of the system with the low and high pressure reservoirs. The reversible isobaric (and isothermal) heat addition and expansion process that takes place at the highest temperature between States 2 and 3 is where the heat added to the cycle q_{in} goes towards the evaporation of the working fluid. The specific heat added to the system, q_{23}, is given by $q_{23} = T_2(s_3 - s_2) = T_2\Delta s_{\text{vap}}(T_2)$, where T_2 is the temperature at which phase change from liquid to vapour occurs and $\Delta s_{\text{vap}} = s_3 - s_2$ is the change in entropy due to vaporisation at that temperature,

$$q_{\text{in}} = q_{23} = T_2\Delta s_{\text{vap}}(T_2)\,. \tag{2.37}$$

In addition, the specific displacement work done during the isobaric heat addition (phase change) process between States 2 and 3, w_{23}, is $w_{23} = P_2(v_3 - v_2) = P_2\Delta v_{\text{vap}}(P_2)$, where P_2 is the (load) pressure at which the work is done, and $\Delta v_{\text{vap}} = v_3 - v_2$ is the volume change due to vaporisation at that pressure. The net work output is equal to the work done during this positive-displacement, that is the process when a fluid is pumped to a higher pressure, process minus the work dissipated in displacing the atmosphere (taken as the minimum pressure, $P_1 = P_{\text{atm}}$), $P_1\Delta v_{\text{vap}}(P_2)$, which is not considered 'useful'. Therefore the *net useful*

displacement work between States 2 and 3 is $w_{23} = (P_2 - P_1)\Delta v_{\text{vap}}(P_2)$ and the total w_{net} over the cycle is,

$$w_{\text{net}} = w_{23} = (P_2 - P_1)\Delta v_{\text{vap}}(P_2)\,. \tag{2.38}$$

The working fluid thermal efficiency η_{wf} is defined as the ratio of the net displacement work done to the total heat input to the ideal cycle in Fig. 2.6. Using the expressions derived above, the working fluid efficiency is obtained as,

$$\eta_{\text{wf}} = \frac{w_{\text{net}}}{q_{\text{in}}} = \frac{(P_{\text{max}} - P_{\text{min}})\Delta v_{\text{vap}}(P_{\text{max}})}{T_{\text{sat}}\Delta s_{\text{vap}}(T_{\text{sat}})}\,, \tag{2.39}$$

where P_{max} $(= P_2)$ is the maximum pressure that the device is displacing against, P_{min} $(= P_1 = P_{\text{atm}})$ is the ambient pressure, Δv_{vap} is the volume change by vaporisation at P_{max}, T_{sat} $(= T_2)$ is the saturation temperature at P_{max}, and Δs_{vap} is the entropy change due to vaporisation at T_{sat} and P_{max}. Given that this definition of the working fluid efficiency η_{wf} does not include any information on the particular configuration of the device, this efficiency measure can be considered the maximum efficiency that a *fluid* can achieve in undergoing the ideal cycle illustrated in Fig. 2.6. It is also noted that in this ideal cycle, following isothermal phase-change expansion and then adiabatic expansion to State 4, a cold sink at T_{min} $(= T_1)$ always exists (that is not necessarily at ambient temperature) into which heat can be rejected from States 4 to 1, to close the cycle.

2.5.2 NIFTE exergy efficiency (η_{ex})

The small temperature differences made available externally to the NIFTE device establish a small temperature difference between its hot and cold heat exchangers. As stated previously, this imposes a low Carnot efficiency (the maximum efficiency any heat engine can achieve operating between those two temperatures), and consequently also, an inherently low thermal efficiency onto this specific device. The exergy efficiency, which is defined as the ratio of the thermal efficiency to the Carnot efficiency at equivalent conditions, is a better thermodynamic performance indicator for the NIFTE. The exergy efficiency η_{ex} is evaluated as the time-averaged power dissipated in the load over the time-averaged exergy flow-rate into the device from the

heat source [43],

$$\eta_{\text{ex}} = \frac{\overline{P_{\text{l}}(t)U_{\text{l}}(\text{t})}}{\overline{T_{\text{hx}}(t)\dot{S}_{\text{th}}(t)}} = \frac{\overline{P_{\text{l}}(t)U_{\text{l}}(t)}}{\overline{P_{\text{hx}}(t)U_{\text{th}}(t)}} = \left|\frac{P_{\text{l}}}{P_{\text{hx}}}\right|^2 \frac{\text{Re}\,(1/Z_{\text{l}})}{\text{Re}\,(1/Z_{\text{TOT}})}\,, \tag{2.40}$$

where T_{hx} is the external temperature of the heat exchanger surfaces, $\dot{S}_{\text{th}}$ is the entropy flow-rate into the device, P_{hx} is the pressure that represents the temperature of the heat exchanger, P_{l} is the pressure in the load (which is application specific), and U_{l} and U_{th} are the volumetric flow-rates of pumped liquid in the load and evaporating vapour at the heat exchangers, respectively. The transfer function $P_{\text{l}}/P_{\text{hx}}$ that appears on the right-hand side of Eq. (2.40) can be found from the expressions given in Table 2.1, and the application of Kirchoff's voltage and current laws to the NIFTE circuit. In addition, Z_{TOT} is the total impedance of the NIFTE circuit given in Eqs. (2.27), (2.30) (2.35), and $Z_{\text{l}} = R_{\text{l}} + sL_{\text{l}}$ as defined and used in Table 2.1.

Then, the exergy efficiency η_{ex} of the NIFTE can be found from evaluating Eq. (2.40) at the marginal stability frequency f_0, for a given set of values for the R, C and L parameters that appear in the relevant expressions and transfer functions that appear in the definition of η_{ex}. Referring to the definitions of the R, C and L parameters listed in Table 2.2, note that each parameter is a function of physical characteristics (geometric variables/dimensions) of the actual NIFTE device and thermophysical properties of the working fluid and pumped medium.

2.5.3 NIFTE thermal efficiency (η_{th})

A thermal efficiency η_{th} of the NIFTE can be evaluated from the exergy efficiency η_{ex} (Section 2.5.2) and the Carnot efficiency η_{Carnot} (refer Eq. (1.1)), for a given set of thermal boundary conditions to the device, such that,

$$\eta_{\text{th}} = \eta_{\text{ex}}\eta_{\text{Carnot}}\,, \tag{2.41}$$

where as previously mentioned, the Carnot efficiency is the maximum efficiency any thermodynamic cycle can achieve working between a given heat source (T_{H}) and cold sink (T_{C}) temperature, such that $\eta_{\text{Carnot}} = 1 - T_{\text{C}}/T_{\text{H}}$.

2.6 Summary

The method by which the NIFTE models have been developed has been presented in this chapter. The models shown are an extension of the first model presented by Smith [2]. Three models have been developed, each using a different description for the heat exchange process; linear temperature profile (LTP) model, constant temperature difference (model) and the dynamic heat exchanger (DHX) model.

From running the models, several key and interesting properties of the NIFTE can be found, namely the oscillation frequency and the exergetic efficiency. It is shown how each of these properties are found and calculated from the models. In the next chapter, these three models will be investigated by carrying out a parametric study wherein the parameters given in Table 2.2 are varied across a range of values. The models are compared with the key properties of the NIFTE. This is a useful exercise to carry out to determine which, if any, of the models presented in this chapter best represents the NIFTE prototype developed and described by Smith [2].

3 Parametric Investigation on LTP, CTD and DHX models

Three models believed to be a simplified theoretical representation of the NIFTE, based on the description provided by Smith [2], are developed and presented in Chapter 2. In order to determine the model, if any, that best describes the NIFTE, a parametric study is carried out. This involves varying the value of a parameter in order to determine the impact on the results obtained. From this, the results obtained from the model can be compared to experimental data based on the device undergoing the same parametric changes. In addition, parametric studies are often carried out to aid in early stage design of novel technologies and is a technique that is used to determine the best design for a device.

In Smith [2, 34, 35] a simple, but useful model for the dynamic behaviour of the NIFTE was proposed, using similar methods as in Backhaus and Swift [35], Ceperley [25] and Huang and Chuang [42]. This approach of forming spatially lumped and first order linear sub-models for each sub-component of the NIFTE is given in Chapter 2. The network employed in Refs. [2, 34, 35] contains resistive and capacitive components, with the former accounting for viscosity, fluid drag and thermal resistance, and the latter for gravity and compressibility. However, it does not contain inductive components, and as such cannot capture finite inertive effects that embody (fluid) inertial phenomena.

The original 'non-inertive model' was validated against experimental data, with partial success. For example, in Ref. [35] good predictions of the trends of the NIFTE's oscillation frequency (f_0) and temperature gain (related to the spatial temperature gradient in the heat exchangers) required for operation (k) were obtained by adjusting a parameter that was not measured, specifically the feedback valve resistance (R_f), in order to obtain the best fit between model predictions and experimental data. However, this fit was

performed by the inclusion of R_f into a term that was then scaled. Since the behaviour of the NIFTE is very sensitive to this parameter, this may have led to a situation whereby even though the trends of f_0 and k were captured, the actual values for R_f necessary to achieve this, which were hidden by its grouping with other parameters, were unrealistic.

Furthermore, the non-inertive LTP model's predictions of the variations in the NIFTE's oscillation frequency due to changes in the load did not correlate well with experimental observations [2, 35]. It was proposed that this is probably due to a transition in the mode of evaporation in the hot heat exchanger from pool boiling to flash boiling, which is not accounted for in the model, as well as a breakdown of the assumption that the specific volume of the vapour is much greater than that of the liquid. It is important to ascertain whether this discrepancy can in fact be explained by reference to inertial effects. An objective of the current work is to examine the applicability of inertive LTP model of the NIFTE, presented in Chapter 2, that includes resistive, capacitive and inductive components, and to compare key results with those from the non-inertive LTP model.

In addition to this, the heat exchangers in the NIFTE is considered to be one of the most important components of the NIFTE device, however it is also the most poorly understood, mainly due to the complex nature of the two-phase heat transfer that takes place there. Smith [2, 34, 35] first proposed a model in which a linear temperature profile (LTP) along the height of the hot and cold heat exchangers was assumed. The linear temperature profile assumption was a reasonable starting point in the modelling of this device, yet it is evident that it is also unrealistic since it implies an unbounded hot and cold temperature availability in the heat exchangers. Two alternative models for the heat exchangers and the associated heat transfer process are proposed and described in full detail in Chapter 2: a constant temperature difference (CTD) model and a dynamic heat exchanger (DHX) model. To determine the best description for the heat exchange process, the key performance indicators of the inertive LTP, CTD and DHX models, are compared. The results presented in this chapter have been in publish in Refs. [49, 50].

3.1 LTP, CTD and DHX models

In Chapter 2, a detailed description of the linear temperature profile (LTP), constant temperature difference (CTD) and dynamic heat exchanger (DHX) models for the NIFTE is given. The differences between these

models is given in Chapter 2, but briefly going through it here. In the LTP model it is assumed that all heat transferred per unit time, that is $\dot{Q}$, between the heat exchangers and the working fluid results in phase change of a thin active region of the working fluid at the vapour-liquid interface in the displacer cylinder only. In addition it is assumed that this process is governed by a convective heat transfer equation involving a constant heat transfer coefficient h, $\dot{Q} = hA_s\left[T_{HX}(y) - T_{ad}\right]$, where A_s is the (constant) surface area of the heat exchanger which participates in the heat transfer and phase-change process. A linear temperature profile is imposed in the vertical direction at the surface of the heat exchanger blocks, as shown in Fig. 2.2(a). The electrical circuit representation of the LTP model is shown in Fig. 2.4(a).

As in the LTP model, it is assumed that the heat transfer between the heat exchangers and the working fluid in the CTD model is governed by convective phase change heat transfer. However, it is assumed that the temperature difference between the heat exchangers and the working fluid $\Delta T = T_{HX} - T_{ad}$ is constant, as shown in Fig. 2.2(b). As such, heat transfer in the CTD model is allowed to take place over a larger (time-varying) contact area between the heat exchangers and working fluid. The heat exchanger surface area that participates in heat transfer, A_s is equal to the multiple of the (constant) circumference of the heat exchanger blocks l_c and the fluid-solid contact height y such that $A_s(t) = l_c y(t)$, is allowed to evolve with time as the position of the vapour-liquid interface $y(t)$ varies in the displacer cylinder during operation. The heat transfer equation in the CTD model takes the form of $\dot{Q} = hA_s(y)\Delta T = h\left(l_c y\right)\Delta T$. The electrical circuit representation of the CTD model is shown in Fig. 2.4(b).

In the DHX model, the ability of the solid heat exchanger blocks to store and release heat periodically is taken into account. Considering an addition of heat from an external source to the hot heat exchanger block (and a removal of heat from the cold heat exchanger block to an external sink) denoted by $\dot{Q}_{HX}$ and ignoring external heat losses, the heat transfer balance in the heat exchanger blocks is assumed to obey, $\dot{Q}_{HX} - mc_{al}\left(\mathrm{d}T_{HX}/\mathrm{d}t\right) = hA_s(T_{HX} - T_{ad})$, where m is the (fixed) mass of the heat exchanger block that participates in the heat transfer process, c_{al} is the specific heat capacity of the heat exchanger material, which is aluminium for a NIFTE prototype [2, 35]. The active phase change surface area of the surface area is taken to be the same as in the LTP model. In the DHX model, it is assumed that the thermal power $\dot{Q}_{HX}$ deposited into the heat exchanger mass m is proportional to the instantaneous liquid level height in the displacer cylinder $y(t)$, that is $\dot{Q}_{HX}(t) \propto y(t)$ as shown in Fig. 2.2(c). The electrical circuit representation of the DHX model is given in Fig. 2.4(c).

Table 3.1: Values for the thermodynamic properties in Table 2.2, where liquid *n*-pentane and water data are taken at 298.15 K and 1 atm and *n*-pentane vapour data is taken as saturated at 1 atm.

Thermodynamic Property	Value	Units
P_0	1.01×10^5	Pa
T_0	309	K
γ	1.09	-
Δs_{vap}	1.16×10^3	J/kg K
ρ_{wf}	621	kg/m^3
$\rho_{g,0}$	2.98	kg/m^3
ρ_{w}	998	kg/m^3
μ_{wf}	2.18×10^{-4}	kg/m s
μ_{w}	1.00×10^{-3}	kg/m s
$(\text{d}T/\text{d}P)_{\text{sat}}$	28.9×10^{-5}	K/Pa

3.2 Parameter values and investigated Ranges

The results presented in Sections 3.3 and 3.4 are based on a parametric study carried out on the LTP, CTD and DHX models, whereby each parameter is varied over a range which is within acceptable physical limits while all other parameters are set to a nominal value. In order to carry out a parametric study, a nominal value and a range is assigned to each parameter shown in the electrical circuit representations in Fig. 2.4, defined in Table 2.2. It can be seen that the parameters are a function of the geometry and configuration of the NIFTE device, in addition to the thermodynamic properties of the working fluid and the load fluid. In this study, the working fluid is taken to be *n*-pentane, which is the working fluid used in a NIFTE prototype [2, 34, 35] and the load fluid is taken to be water. The thermodynamic properties for these two fluids is shown in Table 3.1, where the properties associated with liquids is taken at ambient temperature and pressure of 298.15 K and 1 atm, respectively, and the vapour properties are taken to be the saturation properties at an ambient pressure of 1 atm.

The nominal values for each parameter in Table 2.2 is calculated based on the configuration of a prototype NIFTE device described in detail in Ref. [2]. The ranges for the parameters are calculated using a minimum and maximum value (within acceptable physical limits for the NIFTE device) for each variable. The nominal values and investigated ranges for the variables are given in Table 3.2 and the corresponding nominal values and ranges for the parameters are given in Table 3.3.

Table 3.2: Nominal values and investigated ranges of variables in Table 2.2

Variable	Nominal Value	Investigated Range	Units
A_d	4.48×10^{-4}	9.71×10^{-5} to 7.34×10^{-3}	m^2
A_f	1.96×10^{-5}	7.85×10^{-7} to 1.96×10^{-3}	m^2
A_l	7.85×10^{-5}	7.07×10^{-6} to 7.85×10^{-3}	m^2
A_p	4.52×10^{-4}	1.96×10^{-5} to 7.85×10^{-3}	m^2
A_s	1.60×10^{-3}	1.07×10^{-4} to 1.22×10^{-1}	m^2
d_f	0.005	0.001 to 0.05	m
d_l	0.01	0.003 to 0.1	m
g	9.81	-	m^2/s
h	4.61×10^3	1.00×10^3 to 2.00×10^4	W/m^2 K
l_d	0.26	0.2 to 2	m
l_f	0.15	0.05 to 0.5	m
l_l	1	0.01 to 30	m
l_p	0.55	0.2 to 2	m
V_0	1.94×10^{-4}	2.37×10^{-5} to 2.25×10^{-2}	m^3

Table 3.3: Calculated nominal values and investigated ranges for the parameters in Table 2.2

Electrical parameter	Nominal value	Investigated range	Units
R_{th}	5.02×10^8	$3.27 \times 10^7 - 6.74 \times 10^9$	$kg\,m^{-4}\,s^{-1}$
R_l	4.08×10^6	$4.08 \times 10^0 - 1.51 \times 10^{10}$	$kg\,m^{-4}\,s^{-1}$
R_f	2.13×10^6	$7.10 \times 10^1 - 4.44 \times 10^9$	$kg\,m^{-4}\,s^{-1}$
C_{ad}	1.76×10^{-9}	$1.87 \times 10^{-9} - 1.46 \times 10^{-7}$	$m^4\,s^2\,kg^{-1}$
C_p	7.43×10^{-8}	$3.22 \times 10^{-9} - 1.29 \times 10^{-6}$	$m^4\,s^2\,kg^{-1}$
C_d	7.35×10^{-8}	$1.59 \times 10^{-8} - 1.21 \times 10^{-6}$	$m^4\,s^2\,kg^{-1}$
C_{hx} (DHX only)	4.79×10^{-9}	9.58×10^{-11} & 9.58×10^{-10}	$m^4\,s^2\,kg^{-1}$
L_l	1.27×10^7	$1.27 \times 10^3 - 4.24 \times 10^9$	$kg\,m^{-4}$
L_p	3.77×10^5	$7.90 \times 10^3 - 3.16 \times 10^7$	$kg\,m^{-4}$
L_f	4.74×10^6	$1.57 \times 10^4 - 3.95 \times 10^8$	$kg\,m^{-4}$
L_d	1.80×10^5	$8.50 \times 10^3 - 6.40 \times 10^6$	$kg\,m^{-4}$

3.3 Comparison of the LTP model with and without inertia

In previous work [2, 34, 35], inertia (i.e. inductances) were assumed to be negligible everywhere. Here, the effect of including finite inductances is investigated by comparing the inertive LTP model's predictions against the non-inertive LTP model (i.e. setting all inductances to zero). Importantly, all other parameters were varied within acceptable physical limits given by the ranges in Table 3.3. The parameters are stated normalised by their nominal values, with the ratio represented by the superscript '*' in each case. The main focus is on the effects of the resistance to flow in the feedback tube (R_f), the resistance to flow in the load (R_l), and the inertia of the liquid in the load (L_l), on the behaviour and performance of the system. The data

was generated parametrically, with each parameter perturbed independently and all others set to a nominal value.

3.3.1 Required gain or heat exchanger temperature gradient

In Fig. 3.1(a) the effects of R_f, R_l and L_l on the required feedback gain k_LTP for marginal stability in the LTP model are shown. The required gain k_LTP is directly proportional to the required temperature gradient along the heat exchanger blocks $(\mathrm{d}T/\mathrm{d}y)_\mathrm{HX}$, and scales with the temperature difference ΔT_HX between the two blocks. The lines on these plots can be considered stability limits at which the system is marginally stable. Below the lines the system is stable (i.e. oscillations decay exponentially), whereas above them it is unstable(i.e. oscillations grow exponentially). Similarly, in Fig. 3.1(b) the effects of R_f and R_l on the required gain for the non-inertive LTP model are shown (i.e. all inductances set to zero).

The most striking feature of Fig. 3.1 is the fact that the inclusion of inertia leads to results that are not only entirely different in magnitude, but also in the trends they reveal and, by extension, the design rules they imply. In Fig. 3.1(a) an increase in resistance leads to a decrease in the required $(\mathrm{d}T/\mathrm{d}y)_\mathrm{HX}$ for operation, which is very desirable given the goal of utilising heat at low temperature. However, in Fig. 3.1(b) a general increase is seen in the required $(\mathrm{d}T/\mathrm{d}y)_\mathrm{HX}$ as the resistances are increased. In the case of R_f this is monotonic, but in the case of the R_l (and also L_l) there is a wide range over which the necessary $(\mathrm{d}T/\mathrm{d}y)_\mathrm{HX}$ is independent of the load. Furthermore, the values of $(\mathrm{d}T/\mathrm{d}y)_\mathrm{HX}$ for the non-inertive model shown in Fig. 3.1(b) are unrealistically high, whereas the temperature gradient in the heat exchangers predicted by the inertive model, shown in Fig. 3.1(a), contains more realistic values which are representative of a prototype device.

Physically, it is expected that a larger feedback resistance R_f will results in a lower flow velocity in the NIFTE, subsequently leading to a lower oscillation frequency f_0, which is shown in further detail in Section 3.3.2 below. Consequently, as the fluid is exposed to the heat source or cold sink for a large period of time, a lower temperature difference between the hot and cold heat exchangers is expected to be required to carry out the required amount of heat transfer./par

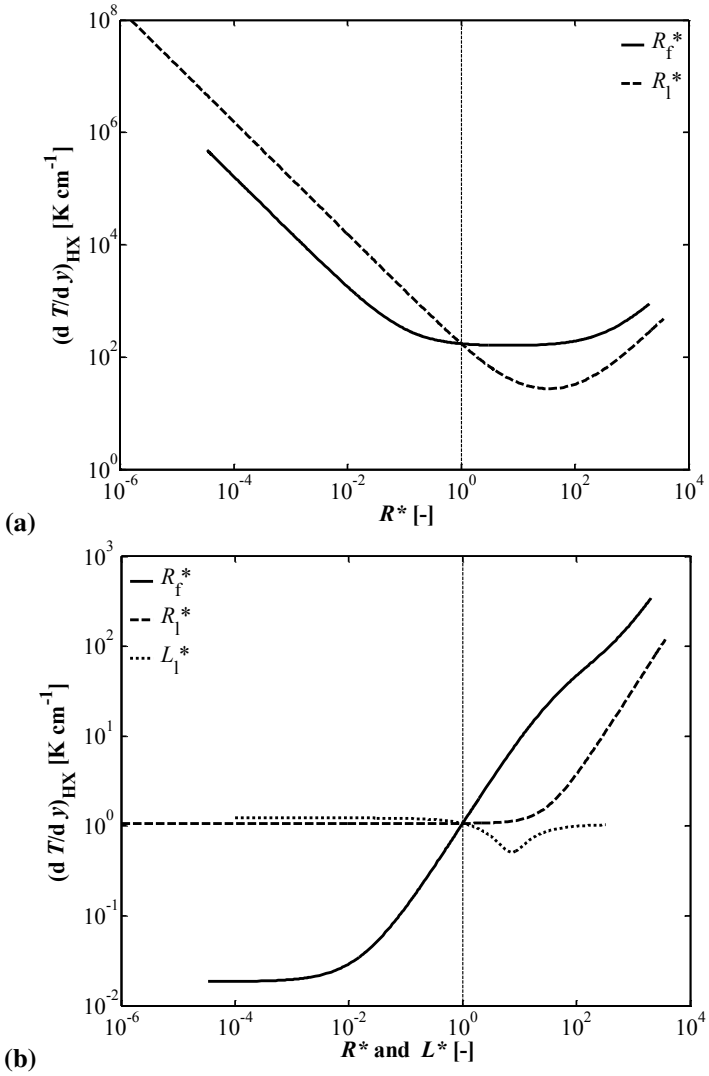


Figure 3.1: Stability plots for the LTP model. Effect of perturbing the main parameters feedback valve resistance R_f (dashed line), load line resistance R_l (solid line) and load line inertia L_l (dotted line) on the value of $(dT/dy)_{HX}$ required for marginal stability; (a) without inductances, and (b) with inductances. Note, each parameter is shown normalised to their nominal value denoted by the superscript '*' and the solid vertical line marks the nominal value and point for all parameters.

3.3.2 Oscillation frequency

In Fig. 3.2(a) the effects of feedback valve resistance R_f, load line resistance R_l and load line inertia L_l on the oscillation frequency f_0 predicted by the LTP model with inertia are shown, and in Fig. 3.2(b) these effects are seen in the absence of inertia. Experimental measurements have shown that the NIFTE operates with a frequency f_0 in the order of 0.1–0.2 Hz [34] for the range of parameters used in the present study.

In both figures f_0 decreases with increasing resistance or inductance, which is expected to occur in the NIFTE. Yet, in Fig. 3.2(b), where the effects of inertia have been neglected, a sharp decrease with increasing resistance is seen, followed by a plateau at large resistance values. The frequency range is large and unrealistic except for those predicted at extremely high resistances. Comparing this result to the NIFTE operation, as mentioned the resistance in the feedback has an impact on the frequency of oscillation, however it is also known that the effect of the liquid mass has an effect on the oscillation frequency such that there it imposes a limit to the frequency that can be achieved. Following this, at low resistances, neglecting the inertive effects of the liquid fluid will lead to an unrealistically high frequency of oscillation. In Fig. 3.2(a) on the other hand, where the fluid inertia has been included, changes in R_f, R_l and L_l are not seen to affect the frequency over a large parameter space. At very high values of these parameters f_0 does indeed decrease, as expected qualitatively from the non-inertive model.

3.3.3 Exergetic efficiency

In Fig. 3.3 the effects of R_f, R_l and L_l on the exergetic efficiency η_{ex} predicted by the LTP model, both with and without inertia, are shown. The inertive and non-inertive values of η_{ex} are significantly different, and clearly the presence of inertia in the load L_l leads to higher (and more realistic) efficiencies. Experimental measurements have shown η_{ex} to be up to 10 % [34] over the range of parameters used in the present study. In both plots it can be seen that an increase in load resistance R_l leads to an in increase in exergetic efficiency η_{ex} until a maximum is reached after which η_{ex} decreases again. However, the effects of feedback valve resistance R_f are contradictory. In the inertive LTP model an increase in R_f leads to a strong reduction in η_{ex}, the exact opposite of which is observed when inertia is neglected.

Summarising briefly, the results shown in Figs. 3.1, 3.2 and 3.3 suggest that the inclusion of inertia leads to a more realistic model, capable of returning values that are comparable to the values observed ex-

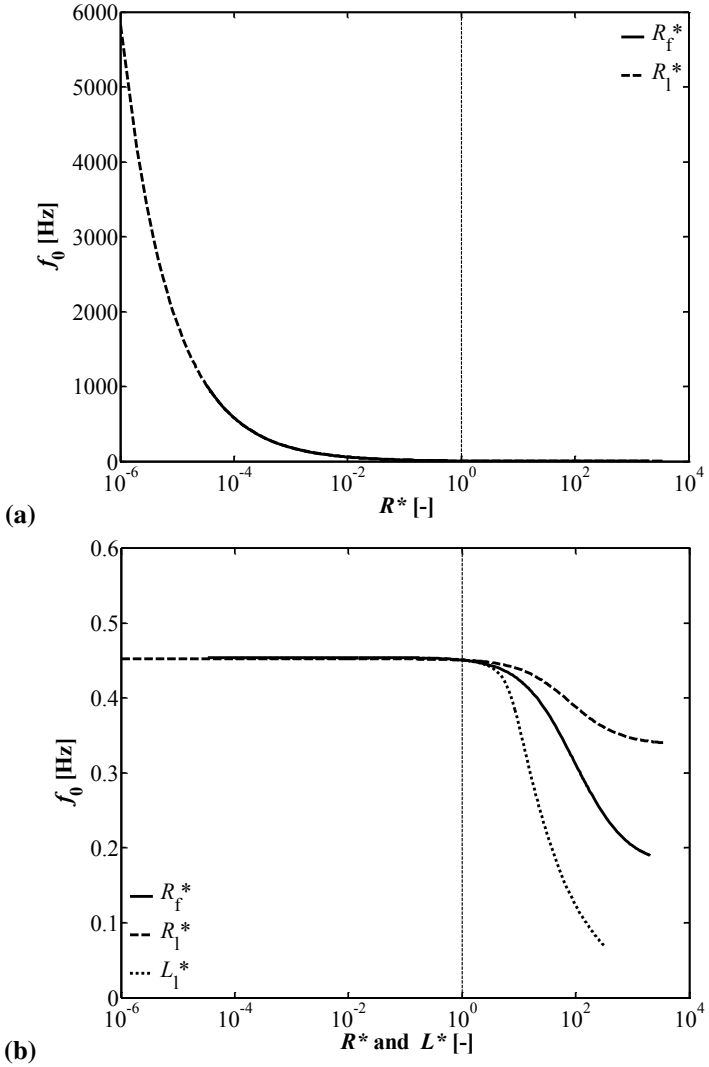


Figure 3.2: Effect of R_f (dashed line), R_l (solid line) and L_l (dotted line) on oscillation frequency predicted by the LTP model; (a) without, and (b) with inductances. Note, each parameter is shown normalised to their nominal value denoted by the superscript '*' and the solid vertical line marks the nominal value and point for all parameters.

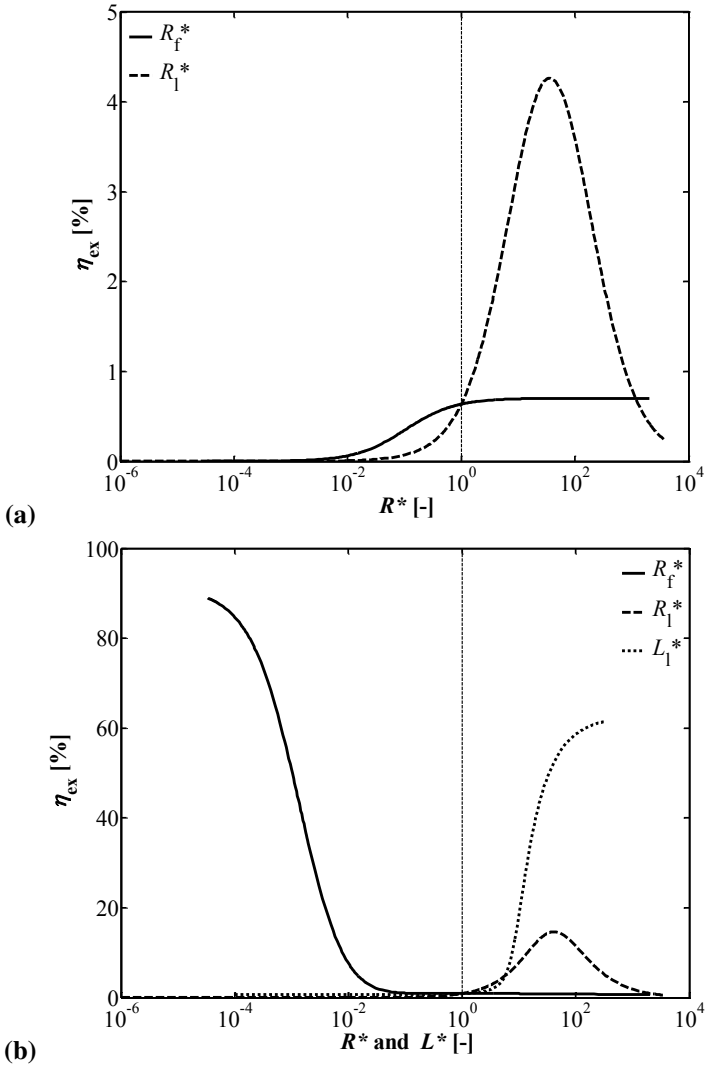


Figure 3.3: Effect of perturbing load parameters; resistance R_l (dashed line) and inertia L_l (solid line), and feedback resistance R_f (dotted line), on the exergetic efficiency η_{ex} of the system; (a) without, and (b) with inductances. Note, each parameter is shown normalised to their nominal value denoted by the superscript '*' and the solid vertical line marks the nominal value and point for all parameters.

Table 3.4: Selection of perturbed values for parameters R_{th}, R_{l}, R_{f}, C_{ad}, C_{p}, C_d and showing the frequencies obtained from the non-inertive model and results from Eq. (3.1) and approximations (i) $|P_1/P_2| \gg 1$, (ii) $|P_1/P_3| \gg 1$, and (iii) $|U_f/U_l| \ll 1$ in Section 3.3.4

		Frequency (Hz)		**Approximations**		
Parameter	Perturbed Value	Non-Inertive Model	From Eq. (3.1)	$\left\|\frac{P_1}{P_2}\right\| \gg 1$	$\left\|\frac{P_1}{P_3}\right\| \gg 1$	$\left\|\frac{U_f}{U_l}\right\| \ll 1$
R_{th}	3.3×10^{7}	1.2×10^{3}	8.2×10^{2}	2.3×10^{0}	2.2×10^{0}	2.4×10^{0}
	6.7×10^{9}	6.7×10^{0}	4.7×10^{0}	2.2×10^{0}	2.2×10^{0}	2.4×10^{0}
R_{l}	4.1×10^{0}	6.7×10^{3}	4.7×10^{3}	2.1×10^{0}	2.0×10^{0}	2.4×10^{0}
	1.5×10^{10}	6.1×10^{-1}	4.3×10^{-1}	3.0×10^{3}	9.0×10^{3}	4.8×10^{-1}
R_{f}	7.1×10^{1}	1.2×10^{3}	8.2×10^{2}	1.1×10^{0}	1.0×10^{0}	4.5×10^{1}
	1.3×10^{9}	4.1×10^{-1}	1.9×10^{-1}	4.3×10^{-1}	4.8×10^{1}	8.8×10^{-3}
C_{ad}	6.4×10^{-10}	1.1×10^{1}	7.9×10^{0}	2.2×10^{0}	2.2×10^{0}	2.4×10^{0}
	1.5×10^{-7}	1.0×10^{0}	5.2×10^{-1}	6.9×10^{0}	2.9×10^{0}	1.3×10^{0}
C_{p}	3.2×10^{-9}	2.4×10^{1}	4.8×10^{0}	2.7×10^{0}	3.9×10^{1}	1.7×10^{0}
	2.0×10^{-3}	4.8×10^{0}	4.8×10^{0}	3.8×10^{1}	1.4×10^{3}	7.5×10^{-2}
C_d	4.2×10^{-8}	8.0×10^{0}	6.3×10^{0}	3.9×10^{0}	2.0×10^{0}	1.9×10^{0}
	1.2×10^{-6}	4.9×10^{0}	1.2×10^{0}	1.4×10^{0}	5.4×10^{0}	3.2×10^{0}

perimentally for the temperature gradient along the heat exchangers, frequency of oscillation and exergetic efficiency [2, 34, 35]. They also suggest that although the NIFTE does not rely on inertia, its presence can lead to significant improvements in performance, and to a change in the predicted behaviour of the system (even qualitatively) that must be taken into account in any model.

3.3.4 Simplifying approximations

For the electrical circuit network in Fig. 2.4(a), neglecting all inertia (i.e. setting all inductances to zero), it was stated in a previous study [34] that subject to a few reasonable approximations, the angular frequency of oscillation ω_0 can be evaluated from,

$$\omega_0 = 2\pi f_0 = \sqrt{\frac{R_{\text{th}} + R_{\text{l}}}{R_{\text{th}} R_{\text{f}} R_{\text{l}} C_{\text{ad}} C_{\text{d}}}}. \tag{3.1}$$

The validity of these approximations, which are: (i) $|P_1/P_2| \gg 1$, (ii) $|P_1/P_3| \gg 1$, and (iii) $|U_{\text{f}}/U_{\text{l}}| \ll 1$, are investigated in this section. Starting from nominal values, each system parameter was changed to a 'high' and 'low' value, which was still practically viable, with all other parameters unchanged, that is they remain at their nominal values. Recall from Section 3.2 that practically achievable values for each parameter were chosen as representations of reasonable incremental perturbations from the existing physical

NIFTE [2, 34, 35], always leading to an acceptable and realistic design. The nominal value of each parameter can be found in Table 3.3, and the results from the parametric study are shown in Table 3.4. Specifically, from the second and third columns it can be seen that the approximate result for the oscillation frequency f_0 from Eq. (3.1) captures the order of magnitude for f_0 as evaluated from the non-inertive model, though discrepancies of up to a factor of 5 can be seen. This discrepancy is investigated further in Fig. 3.4. We note that capacitance in the power cylinder C_p is absent from Eq. (3.1) due to the assumption that $|U_\mathrm{f}/U_\mathrm{l}| \ll 1$. It can be seen in Table 3.4, as well as in Fig. 3.4(a), that at large values of C_p this assumption holds true. At low values of C_p however, the assumption is far from valid, and therefore Eq. (3.1) will fail to agree with the prediction of f_0 from the non-inertive model to an acceptable degree. Returning to Table 3.4, the last three columns reveal that the approximations are not generally valid. Therefore expressions such as Eq. (3.1) based on these approximations may also not be valid in general, and should be used with care.

The different predictions of the oscillation frequency f_0 are considered more closely in Fig. 3.4(b) and Fig. 3.5. From Fig. 3.2 we are aware that the use of nominal values results in great differences between inertive and non-inertive predictions of f_0. In order to compare further the two models we modify the nominal value of C_p to 7.43×10^{-8} m^4.s^2/kg. Interestingly, the non-inertive prediction of the effect of the feedback tube resistance R_f on f_0 is both: (i) in close agreement with Eq. (3.1), as seen in Fig. 3.4(b); and also (ii) in relatively good agreement with the inertive prediction in Fig. 3.5(a), except at low R_f. However, even in this case, there remains a deviation in the predictions of the effect of load resistance R_l on f_0 between the non-inertive and inertive models, the latter of which are considerably more realistic. It is possible that inertia is responsible for the model-experiment discrepancy observed in Ref. [35], although there are other factors which have not been taken into account and are probable to be playing a role.

3.4 Comparison of LTP, CTD and DHX models

In this section the results from a parametric study performed on the three models for the NIFTE developed in Chapter 2, that is the linear temperature profile (LTP), constant temperature difference (CTD) and dynamic heat exchanger (DHX) model, whereby each parameter was perturbed independently while all others were set to their nominal values (shown in Table 3.3) is presented. The parameters are stated normalised by their nominal values as in Section 3.3, with the ratio represented by the superscript '*' in each case. The results

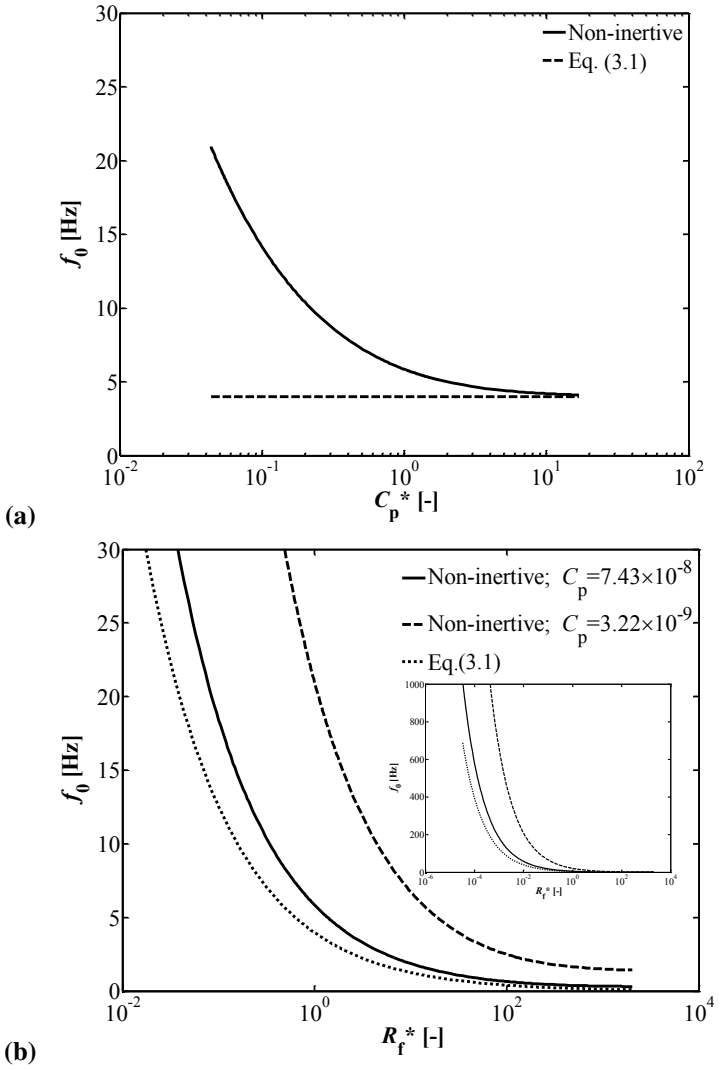


Figure 3.4: Effect of (a) the capacitance in the power cylinder C_p and (b) the resistance in the feedback tube R_f, on the oscillation frequency f_0 from the non-inertive model and comparison with prediction from Eq. (3.1). The dashed lined represents the results from Eq. (3.1), and the solid and dotted lines represent results at $C_p = 7.43\times10^{-8}$ and $C_p = 3.22\times10^{-9}$ m^4.s^2/kg, respectively. Note, each parameter is shown normalised to their nominal value denoted by the superscript '*'.

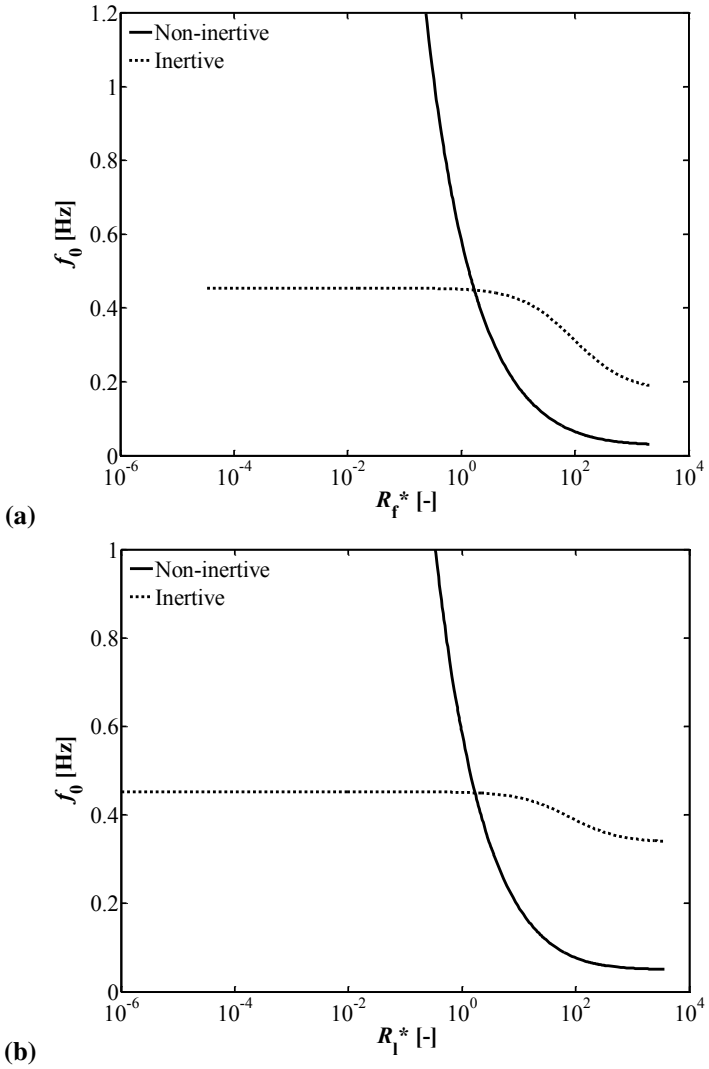


Figure 3.5: Effect of inertia on the variations in oscillation frequency f_0 due to (a) feedback tube resistance R_f and (b) load resistance R_l, with nominal capacitance in the power cylinder C_p = 7.43×10^{-8} m^4.s^2/kg, where the dashed and solid lines are results from the model with and without inductances, respectively. In the case of the non-inertive result we plot f_0/10. Note, each parameter is shown normalised to their nominal value denoted by the superscript '*'.

focus predominantly on the effects of liquid flow resistance (R_f) and inertia (L_f) in the feedback connection. These two parameters represent a part of the physical NIFTE device that can be easily manipulated, even during operation. In addition, a recent study [43] found the efficiency of the NIFTE to be most sensitive to R_f and L_f above all other parameters.

Following from the observations in Section 3.3, it is determined the inertia plays a vital role in the model predictions for the key performance indicators, that is the feedback gain, oscillation frequency f_0 and exergetic efficiency η_ex and as such in the following and all subsequent studies, the LTP, CTD and DHX models include inertial effects.

3.4.1 Oscillation frequency f_0 and exergetic efficiency η_ex

The effects of (a) the resistance R_f and (b) the inertia L_f in the feedback connection on the marginal stability frequency f_0 and device exergetic efficiency η_ex are shown in Figs. 3.6 and 3.7, respectively. Experimentally, the NIFTE has been shown to operate at frequencies $f_0 = 0.1 - 0.2$ Hz [2]. The three models predict frequencies that are within this expected order of magnitude. At the nominal value for each parameter, $R_f^* = 1$ and $L_f^* = 1$, the LTP and CTD models predict a frequency of very similar value, $f_0 = 0.355$ Hz and $f_0 = 0.357$ Hz, respectively. The DHX model predicts a lower frequency of $f_0 = 0.242$ Hz.

With all parameters set to their nominal values, the LTP and DHX models predict similar exergetic efficiencies of $\eta_{ex} = 0.95\%$ and $\eta_{ex} = 0.89\%$ respectively, whereas the CTD model predicts a much higher efficiency of $\eta_{ex} = 25\%$. This discrepancy persists even when deviating the investigated parameters from their nominal values by a factor within the range $10^{\pm 1}$. The overestimation of efficiency can be attributed to the lack of a thermal resistance (R_th) component in the CTD model. Experimentally η_ex has been measured and found to be of the order of ~1% [35, 43]. This value is best predicted by the DHX model, over the whole range of values for two parameters studied (R_f and L_f). A discontinuity in the efficiency η_ex is observed that arises from a discontinuity in the frequency f_0 when the inertia in the feedback connection L_f (Fig. 3.6(b) and 3.7(b)) is varied. This interesting feature is investigated further in Section 3.4.5.

3.4.2 Feedback gain and heat exchange implications

In Fig. 3.8 the effects of the feedback connection resistance R_f and inductance L_f on the required feedback gain for marginal stability (i.e., for the establishment of sustained oscillations) is shown, for the CTD and

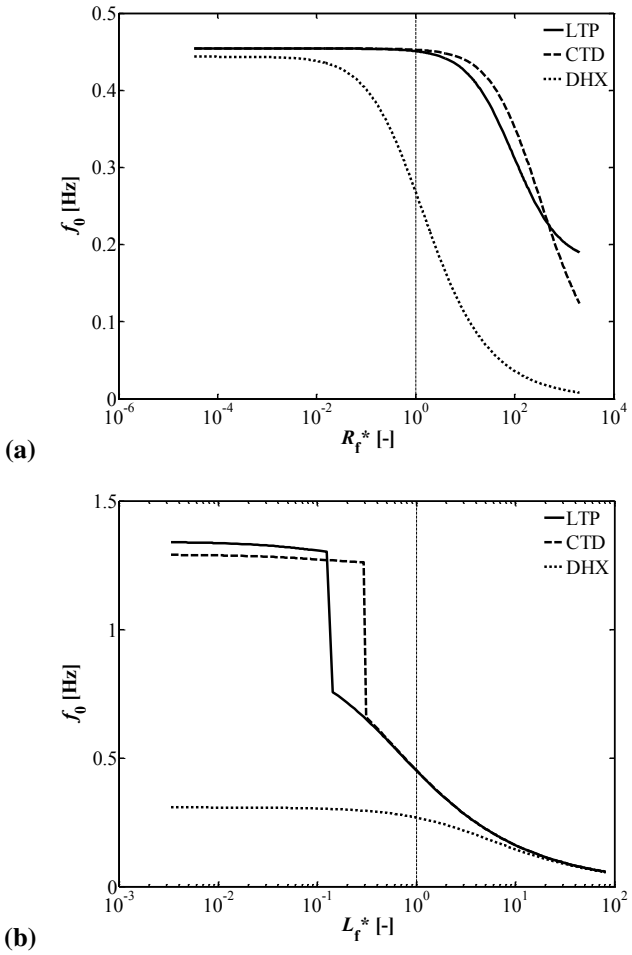


Figure 3.6: Effect of (a) the resistance in the feedback tube (R_f) and (b) the inertia in the feedback tube (L_f) on the marginal stability frequency f_0 of the three models; LTP (solid line), CTD (dashed line) and DHX (dotted line), respectively. The vertical dashed line indicates the position of the parameter nominal value.

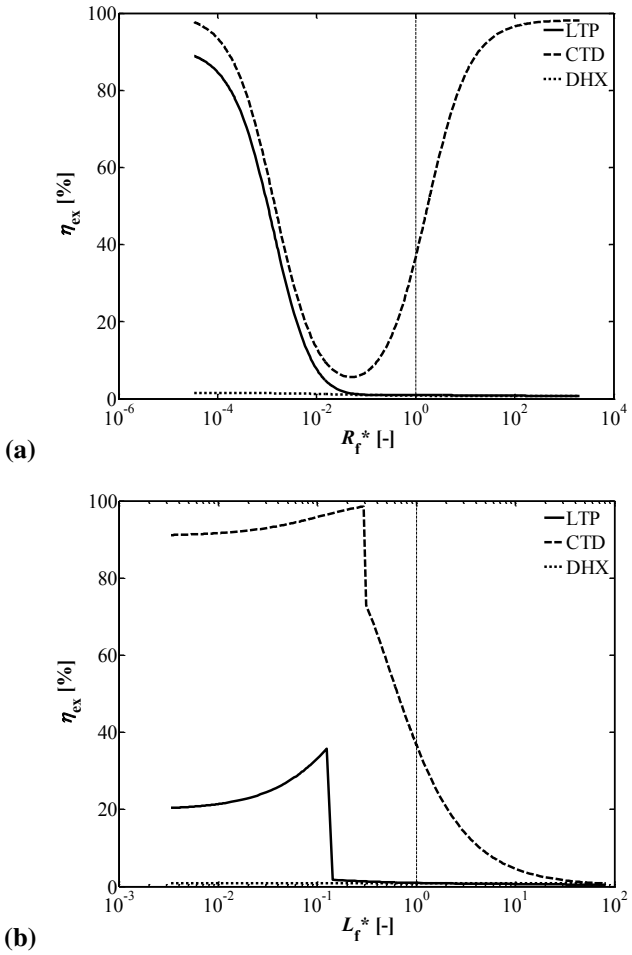


Figure 3.7: Effect of (a) the resistance in the feedback tube (R_f) and (b) the inertia in the feedback tube (L_f) on the device exergetic efficiency η_{ex} of the three models; LTP (solid line), CTD (dashed line) and DHX (dotted line), respectively. The vertical dashed line indicates the position of the parameter nominal value.

DHX models. Results concerning the feedback gain for the LTP model can be found in Ref. [2]. As mentioned in Chapter 2, the feedback gain in the CTD model is proportional to the temperature difference between the heat exchangers and the working fluid ΔT (Fig. 2.2(b)). With all parameters set to their nominal values, the predicted minimum ΔT required for sustained oscillations is 0.2 K, a value that is deemed to be an unrealistically low representation of the real heat transfer process. The CTD model does predict more realistic temperature differences for operation, but at high values of feedback connection resistance R_{f}.

The feedback gain in the DHX model is proportional to the supplied power gradient in the heat exchanger blocks ($\mathrm{d}\dot{Q}_{hx}/\mathrm{d}y$). With the parameters at their nominal values, this model predicts a minimum required gradient of 32 W cm^{-1} for oscillatory operation. A 125 W power source rating, which was used in the experimental prototype to achieve sustained oscillations [35], requires a vertical liquid level oscillation amplitude over the heat exchangers within the displacer cylinder of 3.9 cm to attain this value of power gradient. This calculation does not account for any heat losses, or for the intermittent use of the heat source used to maintain the hot heat exchanger at a specific temperature, as was reported in Ref. [35]. Either of these factors would lead to an underestimation of the power required to achieve sustained oscillations, and an overestimation of the liquid level oscillation amplitude observed during sustained oscillations.

3.4.3 Effect of heat exchanger capacitance $C_{\mathbf{hx}}$ in the DHX model

The thermal capacity of the solid heat exchanger blocks and hence their ability to store and release heat periodically (a process not accounted for in the LTP description), is described by the heat exchanger capacitance parameter C_{hx}. Of the total mass (vertical height) of the heat exchangers (HHX and CHX), only a part is involved in the time-varying heat exchange process with the working fluid. This leads to a difficulty in assigning a value to C_{hx}. Assuming that C_{hx} is determined by the amplitude of the liquid level oscillations over the heat exchangers inside the displacer cylinder, a nominal value for C_{hx} was chosen to correspond to an oscillation amplitude of 12.5 mm, based on visual observations [58]. This however is an arbitrary choice, so in this work we investigate explicitly the effect that other values of C_{hx} will have on the model predictions. Specifically, two values are investigated: 0.2 C_{hx} and 0.02 C_{hx} (see Table 3.3), which represent heights of 2.6 mm and 0.26 mm in the heat exchangers.

For each of the three selected values of C_{hx}, the effects of varying the resistance R_{f} and inertia L_{f} associated with liquid flow in the feedback connection on the NIFTE oscillation frequency f_0 and exergetic

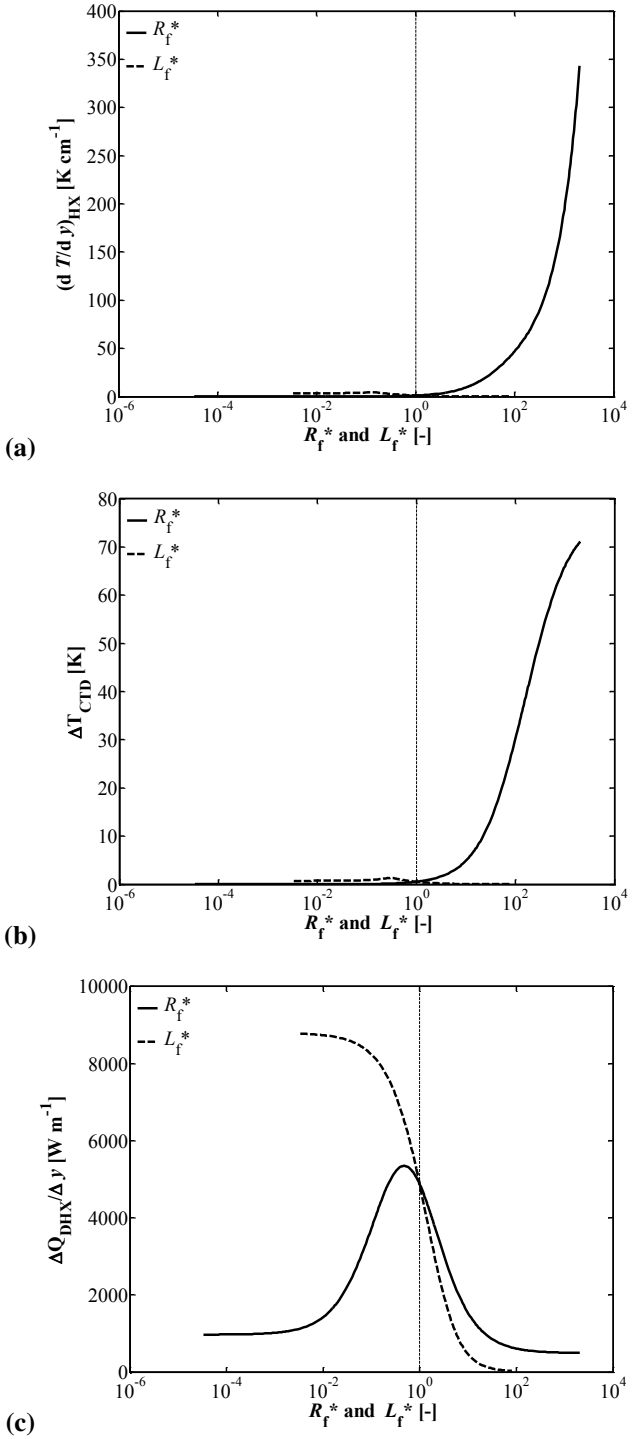


Figure 3.8: Effect of R_f (solid line) and L_f (dashed line) on the feedback gain of the (a) LTP, (b) CTD and (c) DHX models. The vertical dashed line indicates the position of the parameter nominal value.

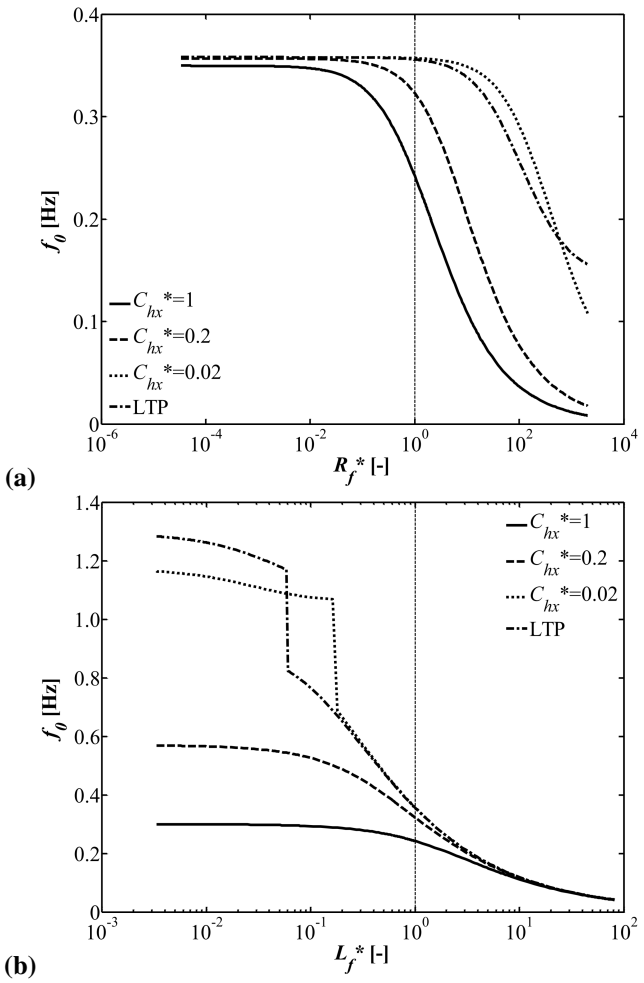


Figure 3.9: Effect of (a) R_{f} and (b) L_{f} on the marginal stability frequency f_0 on the exergetic efficiency η_{ex}, for the LTP model (dash-dot line) and DHX model at various C_{hx} values. The vertical dashed line indicates the position of the parameter nominal value.

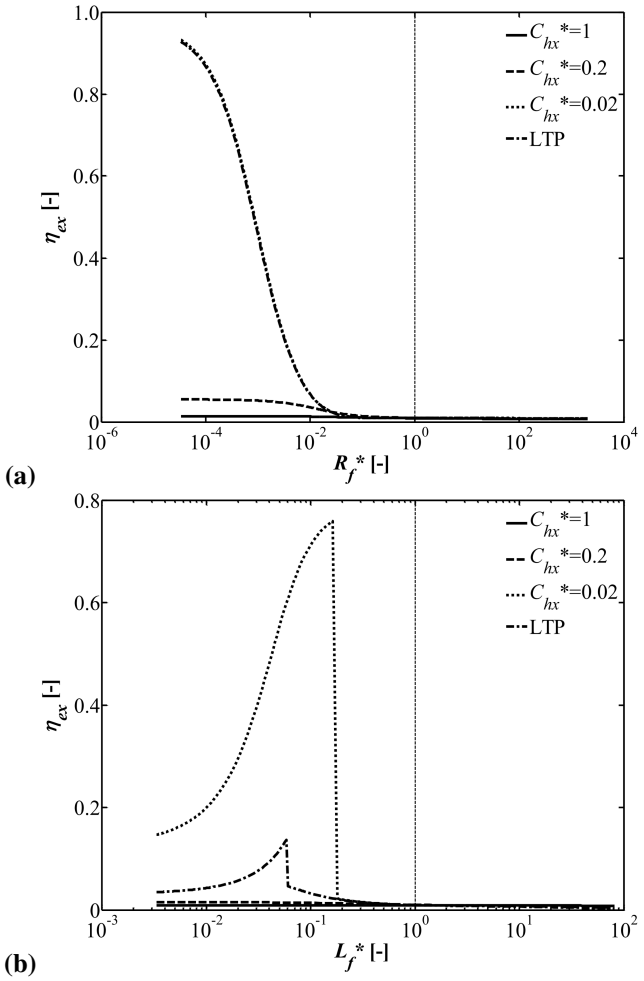


Figure 3.10: Effect of (a) R_f and (b) L_f on the exergetic efficiency η_{ex}, for the LTP model (dash-dot line) and DHX model at various C_{hx} values. Note in (a), the $C^*_{hx} = 0.02$ line is superimposed by the LTP line. The vertical dashed line indicates the position of the parameter nominal value.

efficiency η_{ex} are shown in Figs. 3.9 and 3.10, respectively. In both the LTP and DHX models the resulting frequencies calculated over the investigated ranges of R_f and L_f are representative of those observed in the NIFTE prototype, though lower values of C_{hx} in the DHX model lead to higher f_0, as well as higher η_{ex}. Indeed, the efficiencies predicted for 0.02 C_{hx} are not representative of the prototype for low values of R_f and L_f (consider that the maximum η_{ex} reported was 10% [2]). This is expected, as the oscillation amplitude associated with this heat storage capacitance is considerably smaller than observations on the prototype [58]. In addition a discontinuity in L_f appears at this value of C_{hx} (Fig. 3.9(b) and 3.10(b)). Finally, we also observe that the LTP model does not predict realistic values for η_{ex} at low values of R_f.

3.4.4 Further LTP and DHX model comparison

The load and the parameters that are associated with it (i.e., the liquid flow resistance R_l and inertia L_l) will be predefined by the fluid pumping application, which in turn will be determined by the pumping ability expected of the engine. Therefore, the designer is expected to have little control over these parameters once the NIFTE pump has been deployed. Nevertheless, it is useful to investigate the predicted behaviour of the NIFTE in the LTP and DHX models at loads that are lower and (more importantly) higher than nominal, as this may reveal important information relating to suitable uses of the device.

The effects of the feedback connection resistance R_f and inertia L_f on the marginal stability frequency f_0 of the LTP and DHX models with different loads are shown in Figs. 3.11 and 3.12, respectively. In both models, increased R_f or L_f lead to lower f_0, consistent with experimental observations. At low feedback inertia L_f and low load inertia L_l (Fig. 3.11(b), dotted line), the f_0 values predicted by the LTP model are unrepresentative of the actual device. Furthermore, when required to operate with high loads (associated with large values of R_l and/or L_l) the predicted f_0 from the DHX model is low, insensitive to changes in R_f and almost independent of variations in L_f. This has important implications on the ability of the feedback tube and valve to regulate the frequency behaviour of the device in these conditions.

The corresponding results for the exergetic efficiency η_{ex} of the NIFTE LTP and DHX models is shown in Fig. 3.13 and 3.14, respectively. When connected to loads with low load resistance R_l, the exergetic efficiency η_{ex} is almost zero. This is expected since little power can be dissipated in the load R_l. In loads with high R_l, η_{ex} is generally also high, and in the DHX model η_{ex} is seen to improve with an increase in R_f, though not L_f. Importantly, we find that except at high R_l, the feedback connection R_f and L_f again have

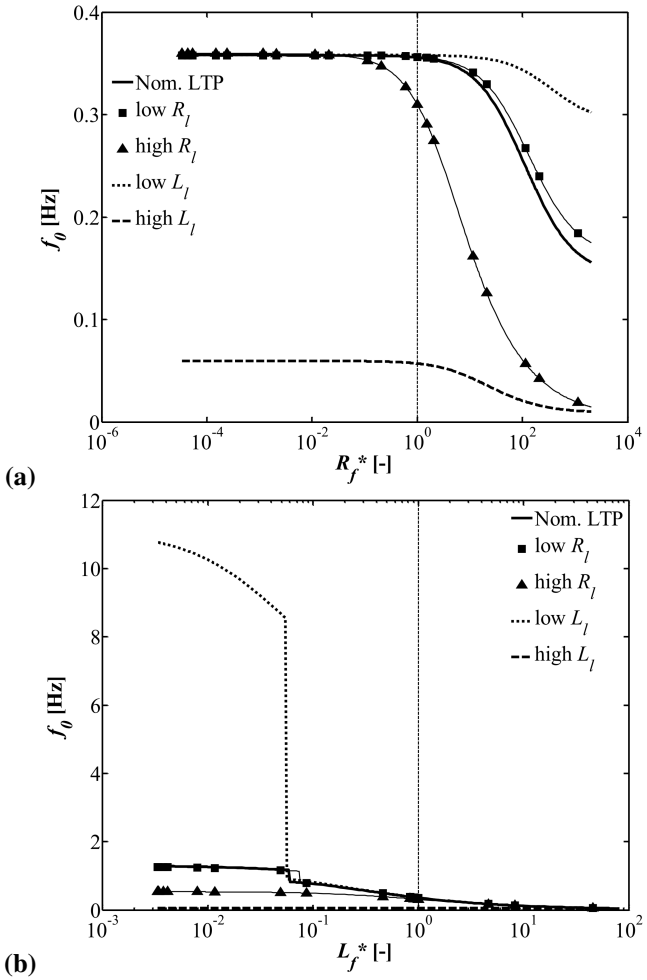


Figure 3.11: Effect of (a) R_f and (b) L_f on the marginal stability frequency f_0 for the LTP model at nominal values (black solid line), low R_l (square symbol), high R_l (triangle symbol), low L_l (dotted black line) and high L_l (dashed black line). The vertical dashed line indicates the position of the parameter nominal value.

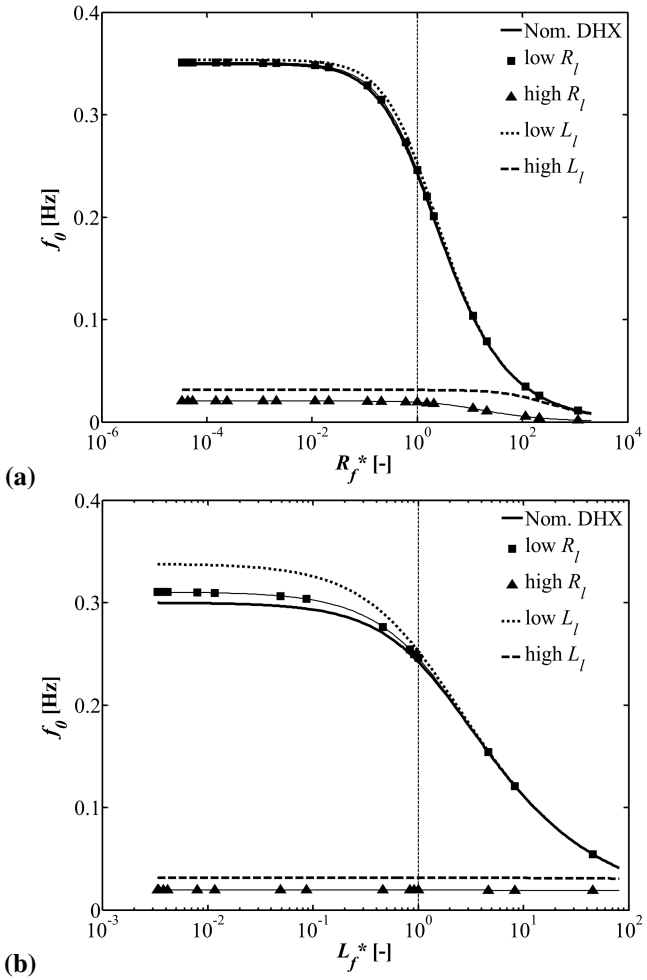


Figure 3.12: Effect of (a) R_f and (b) L_f on the marginal stability frequency f_0 for the DHX model at nominal values (black solid line), low R_l (square symbol), high R_l (triangle symbol), low L_l (dotted black line) and high L_l (dashed black line). The vertical dashed line indicates the position of the parameter nominal value.

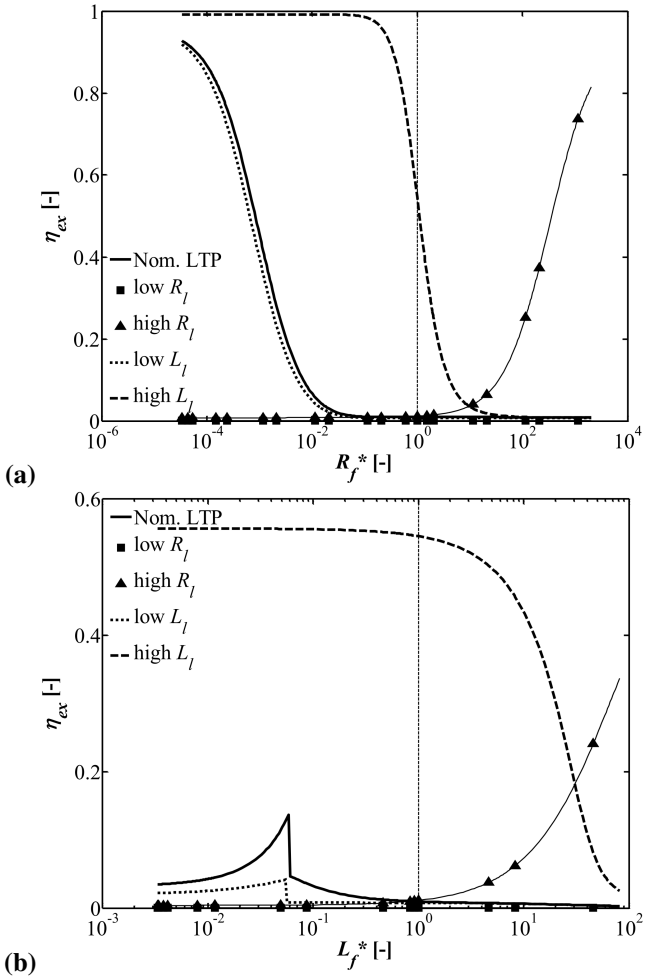


Figure 3.13: Effect of (a) R_f and (b) L_f on the exergetic efficiency η_{ex} for the LTP model at nominal values (black solid line), low R_l (square symbol), high R_l (triangle symbol), low L_l (dotted black line) and high L_l (dashed black line). The vertical dashed line indicates the position of the parameter nominal value.

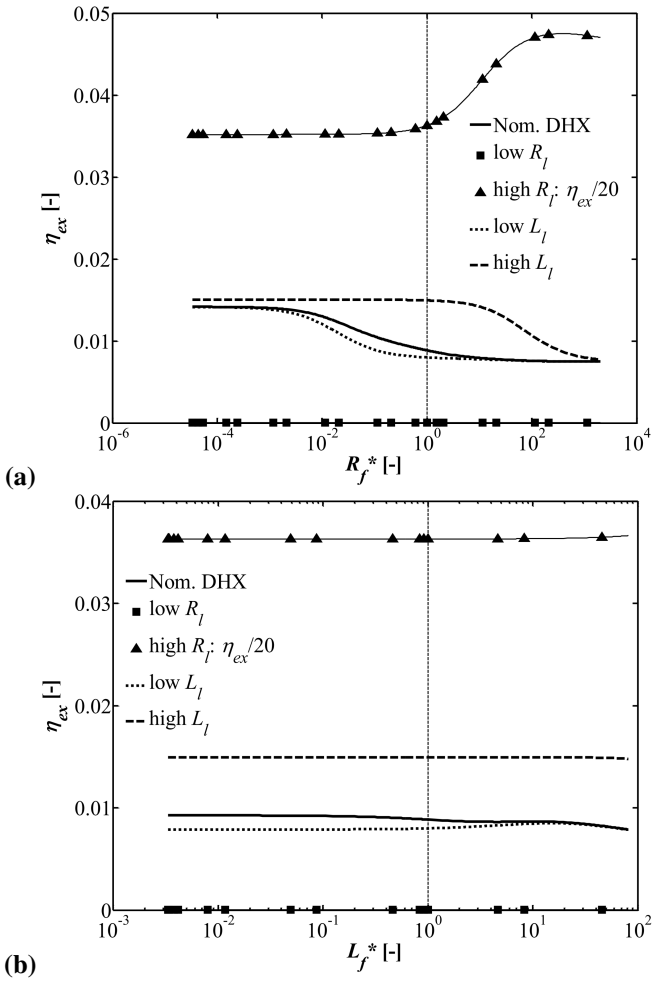


Figure 3.14: Effect of (a) R_f and (b) L_f on the exergetic efficiency η_{ex} for the DHX model at nominal values (black solid line), low R_l (square symbol), high R_l (triangle symbol), low L_l (dotted black line) and high L_l (dashed black line). The vertical dashed line indicates the position of the parameter nominal value.

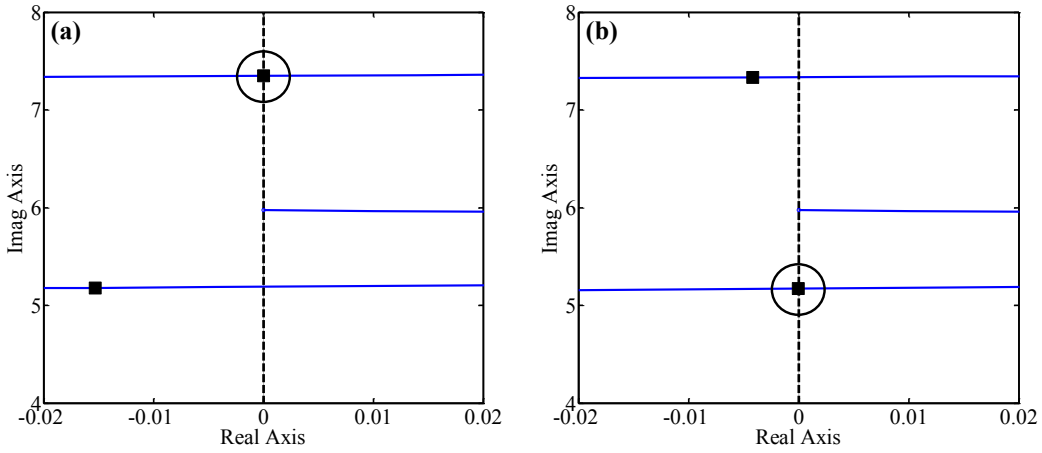


Figure 3.15: Root locus of the closed loop poles for the LTP model on the Argand diagram, showing the shift in the dominant (purely imaginary) marginal pole (circled) with a change in parameter L_f, from (a) $L_f = 2.78 \times 10^5\,\mathrm{kg\,m^{-4}}$ to (b) $L_f = 2.87 \times 10^5\,\mathrm{kg\,m^{-4}}$. N.B.: There are 5 poles in total; the rest are not shown and lie in the stable left-hand side of the diagram, with a negative real part.

little effect on the predicted η_ex from the DHX model compared to the effects of the load resistance R_l and inertia L_l (Figs. 3.14(a) and (b)). Finally, it may also be concluded from this figure that the revised DHX model is more robust than the LTP equivalent to the appearance of discontinuities in f_0, and subsequently η_ex.

3.4.5 Discontinuity in the marginal stability frequency f_0

As mentioned in Section 3.4.1, a discontinuity in the marginal stability frequency is observed when varying the feedback connection inertia L_f (see Fig. 3.6(b)) in both the LTP and CTD models. In the DHX model this behaviour is observed only at the lowest C_hx of 0.02 C_hx (see Fig. 3.9(b)). Discontinuities in f_0 are observed in all three models when perturbing the parameters relating to the power cylinder (hydrostatic capacitance C_p and fluid inertia L_p) and the feedback connection inertia L_f, as noted in Table 3.5.

It was stated in Chapter 2 that the closed loop transfer function of the LTP model has five poles: one real and two complex conjugate pairs. At marginal stability one pair of poles lies on the imaginary axis, and all other poles have negative real parts. The y-value at which the poles cross the imaginary axis corresponds to the angular frequency of marginal stability oscillation. Close inspection of the discontinuity results leads to the observation that the discontinuity arises from the fact that the dominant pair of poles, that is, the pair of

poles that cross the imaginary axis first as the gain is increased, changes for a given set of conditions. For example, the change in the dominant pole pair that leads to the discontinuity shown in Fig. 3.15 arises due to a change in feedback connection inertia L_f from $2.78 \times 10^5\,\mathrm{kg\,m^{-4}}$ to $2.87 \times 10^5\,\mathrm{kg\,m^{-4}}$.

This is the first time that this discontinuous behaviour has been observed and reported for the NIFTE. Previous NIFTE models [2, 34, 35], in which inertia was excluded, contained only three poles in the CLTF (i.e., only one conjugate pole pair), which could not lead to the discontinuous behaviour that has been observed here. The discontinuous behaviour was only possible with the inclusion of the inertive components, leading to the existence of five poles (i.e., two conjugate pole pairs). Though it has not been reported experimentally as yet, possibly due to the required variations from the device's nominal parameters, the emergence of the possibility of discontinuous behaviour to variations in the device's parameters is clearly both interesting and important for the engineering design of such devices.

Discontinuities were observed in all three models as the hydrostatic capacitance C_p and inertia L_p in the power cylinder were varied. Furthermore, changes in the feedback connection inertia parameter L_f lead to discontinuities in the LTP and CTD models, whereas no discontinuity was found in the DHX model inside the investigated parameter range. In order to determine whether discontinuities presented themselves at parameter extremes in the DHX model, all parameters were perturbed beyond their normal investigated ranges in Table 3.3, where no discontinuities were found outside the stated ranges. Table 3.5 summarises the deviations from the nominal values at which the discontinuities occurred for each model. Clearly, Table 3.5 demonstrates that the DHX model is more robust to this behaviour than the other two models.

Table 3.5: The extent by which C_p, L_p and L_f need to be perturbed by in order to observe a discontinuity in the marginal stability plot in each of the three models: LTP, CTD and DHX

	LTP	CTD	DHX
C_p^*	10	6.1	25
L_p^*	0.06	4.9	0.25
L_f^*	10	0.18	No discontinuity

3.5 Summary of chapter findings

The linear temperature profile (LTP) model with inertia was compared to previous investigations carried out on the NIFTE thermofluidic oscillator [2, 34, 35] in which all inertial effects were neglected. When

comparing predictions from the inertive LTP model with those from a non-inertive LTP model, significant differences are found. Further, the predictions from the non-inertive model diverge significantly from experimental observations. We conclude that inertia may constitute an important factor in the modelling of this system. Specifically, the effects of: (i) fluid flow drag (resistance) and inertia in the load; as well as (ii) feedback valve drag, on the marginal gain (minimum temperature difference between the source and sink heat exchangers necessary for operation), frequency and exergetic efficiency of the NIFTE are investigated. Increases in load resistance and inertia have little effect on the gain and oscillation frequency, except at high values of resistance and inertia, when there is an increase in gain and decrease in frequency. These observations are not in accordance with corresponding non-inertive model predictions. Moreover the gain and frequency predictions in the absence of inertia are quantitatively un-physical. Of interest to the designer is the finding that decreasing the feedback valve resistance or increasing the load inertia lead to increases in efficiency, while an increase in load resistance leads to an in increase in efficiency until a maximum is reached, after which the efficiency decreases again. When the non-inertive model was developed, certain approximations were made which are shown not to be true generally in describing the system over a range of conditions.

Two models for the two-phase heat transfer in the NIFTE were compared the inertive LTP model; one involving a constant temperature difference (CTD) between the heat exchangers and the working fluid, and the other allowing for a dynamic heat exchange (DHX) process to take place between the two by accounting for the heat capacity of the heat exchanger blocks. The effects of the flow resistance and inertia in the liquid feedback connection (tube and valve) on the marginal stability oscillation frequency and resulting exergetic efficiency of the device were studied. The CTD model predicted similar (and realistic, when compared to a prototype pumping device) oscillation frequencies to the LTP and DHX models. However, it predicted considerably higher (and unrealistic) exergetic efficiencies than those measured experimentally. This was attributed to the lack of a thermal resistance in the CTD model.

The effects of the heat storage parameter (related to the heat capacity of the heat exchangers) on the oscillation frequency and exergetic efficiency of the DHX model were also investigated. The selected nominal value was found to make realistic predictions of the NIFTE behaviour. When the heat exchanger capacity parameter was sufficiently low, relating to unrealistic oscillation amplitudes, the DHX model presented discontinuities in the frequency and efficiency when parameters associated with the power cylinder were

varied. In fact, discontinuities in the system performance were observed in all three models when perturbing the hydrostatic capacitance and inertia in the power cylinder, and in the LTP and CTD models also when perturbing the inertia in the feedback connection. Importantly, the DHX model was observed to be more robust with respect to the appearance of these discontinuities. Finally, it was found that the feedback connection had a reduced ability to regulate the operation frequency in high load conditions, and a reduced ability to regulate the resulting efficiency in low load conditions.

In conclusion, it is found that the introduction of inertia in the modelling of the NIFTE device is essential to make realistic performance predictions over a range of configurations. In addition to this, though the LTP and DHX models predict the frequency of oscillation well, both overestimate the exergetic efficiency. This is attributed to the neglect of other thermal losses in the NIFTE device, which are identified in Chapter 4.

4 Thermal Losses in the NIFTE

In Chapter 2, three models for the NIFTE were developed and presented known as the linear temperature profile (LTP), constant temperature difference (CTD) and dynamic heat exchanger (DHX). A parametric study was carried out on the LTP, CTD and DHX models in Chapter 3 investigating, in particular, the predicted oscillation frequencies, exergetic efficiencies and necessary conditions in the heat exchangers for sustained operation. It was found that all three models predicted the oscillation frequency well. The CTD model predicted a temperature difference between the heat exchangers and the working fluid of 0.2 K, which is unrealistically low, and exegetic efficiencies that were, consistently over a wide range of conditions, far greater than those observed experimentally in the NIFTE prototype. The LTP model predicted an acceptable temperature gradient in the heat exchangers and the DHX model predicted an acceptable power requirement to achieve sustained oscillations. Despite this, both the LTP and DHX models predicted efficiencies that were often significantly greater than those attained by the NIFTE prototype. It is possible that this can be attributed to loss mechanisms observed in the prototype that have not been taken into account in either model. In Ref. [2] possible losses were suggested to arise from: (i) the periodic condensation and re-evaporation of the working fluid, either on the inner surfaces of the engine due to temperature gradients or from droplet nucleation; and (ii) the irreversible alternating heat exchange between the reciprocating vapour-liquid phases and the solid walls of the engine.

In this chapter the LTP and DHX models, orignially presented in Chapter 2 are extended to take into account some of the losses suggested by Smith [2]. Results from the modified (and original) inertive LTP and DHX models are compared to experimental data from the NIFTE prototype in an effort to determine a model that can most reliably and correctly predict the NIFTE behaviour. Much of the results presented here has been published in Ref. [51]

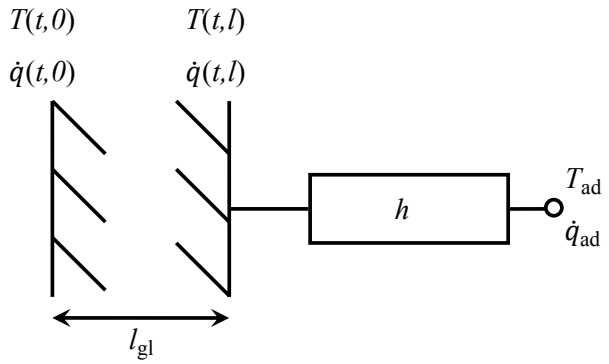


Figure 4.1: Illustration of the unsteady thermal loss impedance Z_{TL} due to irreversible heat transfer, which includes both the convective evaporation/condensation heat transfer loss associated with the heat transfer coefficient h, and the unsteady conduction heat transfer loss through the solid wall with thickness l_{gl}.

4.1 Loss mechanisms

Although the LTP and DHX models have been shown to predict the frequency of oscillation of the NIFTE prototype well, both models significantly overestimate its efficiency. Two loss mechanisms were not included in these models, which are expected to affect detrimentally the accuracy of their predictions [2], in particular with respect to efficiency. These losses are identified as:

(i) Shuttle loss: the loss of exergy arising from the *irreversible* alternating heat transfer between the working fluid and the solid walls of the power cylinder, as a consequence of the vertical oscillation of the vapour-liquid interface and the reciprocating 'washing' motion of the internal surfaces of the power cylinder by the liquid power piston (i.e. heat storage in the power cylinder walls during the high pressure/temperature expansion and discharge stroke, and re-introduction of heat from the walls during the low pressure/temperature compression and suction stroke); and,

(ii) Entrance and retrograde condensation losses: the loss of exergy due to the alternating parasitic condensation and re-evaporation of the working fluid vapour, either onto the inner walls and surfaces of the vapour region or via droplet nucleation caused by the dry[1] properties of the selected working fluid, *n*-pentane, with a timing that counteracts the operation of the device as a whole and is out of phase with the ongoing thermodynamic cycle (i.e. vapour condensation during the

[1] Characterised by exhibiting a positive saturation vapour curve.

positive-displacement expansion and discharge stroke, and re-evaporation of the condensate during the positive-displacement compression and suction stroke).

The shuttle loss mechanism would tend to cause a pressure (and work) loss approximately in phase with the displacement of the liquid level in the power cylinder (i.e. P_{p}), whereas the entrance and retrograde condensation losses would tend to cause a pressure (and work) loss approximately in phase with the evaporation/condensation of working fluid over the HHX/CHX in the displacer cylinder (i.e. U_{th}) and the pressurisation of the vapour volume (i.e. P_{ad}).

4.2 Accounting for thermal losses

It was suggested in Ref. [2] that a first-order linear analogy incorporating an 'effective' thermal resistance and an 'effective' thermal capacitance of the walls of the power cylinder can be used to account for the above losses. A simple circuit representation (see Fig. 5.29, p. 205 in Ref. [2]) of a single thermal resistor in series with a single thermal capacitor was placed in parallel to the adiabatic capacitance in order to account for both the shuttle loss and the entrance condensation. However, it is not possible to account for the combined effects of shuttle loss and entrance condensation with a single electrical component, because, as stated previously and also in Ref. [2], the shuttle pressure loss must appear in phase with P_{p}, not in phase with P_{ad} as is suggested by the thermal loss arrangement in Ref. [2]. In addition, the lumping of the resistive and capacitive effects of the thermal response of the wall into single electrical R-C components is associated with a simplification of unknown magnitude, and need not be done. In any case, no results were actually generated or reported in this source relating to this arrangement.

Although the shuttle loss mechanism was judged in Ref. [2] as being both the more important and the more pronounced thermal loss mechanism of the two, the current effort focusses on the description of the entrance condensation losses as a means by which the efficiencies achieved by the NIFTE prototype can be more closely predicted by the models. The schematic shown in Fig. 4.1 was drawn to indicate how the present modelling formulation aims to account for this loss mechanism. The exergy (work) losses due to the parasitic phase change and associated irreversible cyclic heat transfer that occurs within the nominally adiabatic vapour volume during the evaporation/condensation of working fluid over the HHX/CHX in the displacer cylinder is determined by a complex thermal loss impedance Z_{TL}. In the remainder of this section

we discuss the evaluation of this impedance.

4.2.1 Conduction

The overall conjugate heat transfer process in question includes convection between the fluid and inner surfaces of the device, and conduction through the solid walls, which are not assumed to be adiabatic nor isothermal, but whose temperature is allowed to respond to the heat exchange process. In the solid domain, the solution can be derived from the one-dimensional unsteady heat diffusion equation,

$$\frac{\partial T}{\partial t} = \alpha_{\mathrm{gl}} \frac{\partial^2 T}{\partial x^2} \,, \tag{4.1}$$

where $\alpha_{\mathrm{gl}} = k_{\mathrm{gl}}/\rho_{\mathrm{gl}} c_{\mathrm{gl}}$ is the thermal diffusivity, k_{gl} is the thermal conductivity, ρ_{gl} is the density and c_{gl} is the specific heat capacity of the wall material, which is glass [2, 34].

This partial differential equation can be solved by taking Laplace transforms. For an isothermal boundary condition at the *outer* wall (at $l = 0$, on the outside of the device, $T(t, l = 0) = \text{constant}$; refer to Fig. 4.1) the solution of Eq. (4.1) in the Laplace domain is,

$$Z_{\mathrm{ISO}}(s) = \frac{1}{n k_{\mathrm{gl}}} \tanh\left(n l_{\mathrm{gl}}\right) \,, \tag{4.2}$$

and conversely for an adiabatic outer wall boundary condition (at $l = 0$, on the outside of the device, $\dot{q}(t, l = 0) = 0$) the corresponding solution is,

$$Z_{\mathrm{AD}}(s) = \frac{1}{n k_{\mathrm{gl}}} \coth\left(n l_{\mathrm{gl}}\right) \,, \tag{4.3}$$

where $Z_i(s)$ is the solid impedance defined as $Z_i(s) = \hat{T}(s)/\hat{\dot{q}}(s)$, $\hat{T}(s)$ and $\hat{\dot{q}}(s)$ are the temperature and heat flux fluctuations in the Laplace domain, $n = (s/\alpha_{\mathrm{gl}})^{0.5}$ and l_{gl} is the solid wall thickness [59, 60].

It is found from evaluating n at a given frequency $\omega = 2\pi f$, given a Laplace variable $s = \mathrm{j}\omega$ describing a pure oscillation at this frequency, that,

$$n = \frac{1 + \mathrm{j}}{\delta_{\mathrm{gl}}} \,, \tag{4.4}$$

where the thermal diffusion lengthscale,

$$\delta_{\mathrm{gl}} = \sqrt{\frac{2\alpha_{\mathrm{gl}}}{\omega}} = \sqrt{\frac{\alpha_{\mathrm{gl}}}{\pi f}}, \tag{4.5}$$

is the characteristic length scale of the diffusion problem in the solid.

From Eqs. (4.2) and (4.3), the ratio between this lengthscale and the thickness of the material $l_{\mathrm{gl}}/\delta_{\mathrm{gl}}$ gives an indication of the thermal coupling between both boundaries (inner and outer wall) of the solid. It also determines the lag between temperature fluctuations and heat flux at the wall.

4.2.2 Phase-change convection

Returning to the thermal loss due to the periodic condensation and re-evaporation on the inner walls of the vapour volume, and assuming small fluctuations about the time-mean saturation temperature T_0 (and pressure P_0), the phase-change convective heat transfer that describes this process is,

$$\dot{S}_{\mathrm{th}}(t) \approx \frac{\dot{Q}(t)}{T_0} = \frac{hA_{\mathrm{gl}}}{T_0}\left[T(t, l = l_{\mathrm{gl}}) - T_{\mathrm{ad}}(t)\right], \tag{4.6}$$

where $\dot{Q}$ is the rate of heat transferred from the inner wall surface whose temperature is $T(t, l = l_{\mathrm{gl}})$ to the vapour phase which is at temperature $T_{\mathrm{ad}}(t)$, h is the heat transfer coefficient and A_{gl} is the surface area of the inner wall where the condensation/evaporation occurs.

Using the coupling equations, Eqs. (2.22) and (2.23) in Eqs. (4.2) and (4.6), the total impedance due to thermal losses for an isothermal boundary conditions is,

$$Z_{\mathrm{ISOTL}} = a\tanh\left(bs^{0.5}\right) + c, \tag{4.7}$$

where the thermal loss parameters a, b and c are given by $a = \rho_{\mathrm{g},0}T_0\Delta s_{\mathrm{fg}}\alpha_{\mathrm{gl}}^{0.5}/A_g(\mathrm{d}T/\mathrm{d}P)_{\mathrm{sat}}k_{\mathrm{gl}}$, $b = l_{\mathrm{gl}}/\alpha_{\mathrm{gl}}^{0.5}$, and $c = \rho_{\mathrm{g},0}T_0\Delta s_{\mathrm{fg}}/hA_{\mathrm{gl}}(\mathrm{d}T/\mathrm{d}P)_{\mathrm{sat}}$. Similarly, the impedance due to thermal losses for an adiabatic boundary condition, from Eqs. (4.3) and (4.6), is,

$$Z_{\mathrm{ADTL}} = a\coth\left(bs^{0.5}\right) + c, \tag{4.8}$$

where parameters a, b and c are the same as those given for the isothermal boundary condition. The thermal loss impedances Z_{TL} given in Eqs. (4.7) and (4.8) can be incorporated in the LTP and DHX models.

4.2.3 Linear temperature profile (LTP)

Firstly, using the equation for the thermal resistance in the heat exchangers, Eq. (2.25), and the relations in Sections 2.3.1 and 4.2, an electrical circuit representing the linear temperature profile model including the thermal loss impedance ($\mathrm{LTP_{TL}}$) is developed. The electrical circuit network representing the inertive LTP NIFTE with the thermal loss impedance can be seen in Fig. 4.2(a).

At this stage a transfer function for the NIFTE, which relates an input to an output of the system [57], can be written in order to solve the system. The transfer function for the NIFTE can be found by considering the circuit in Fig. 4.2(a) and using Kirchoff's voltage and current laws [58]. In modelling the NIFTE, the input is taken to be P_{th}, which represents the pressure associated with the temperature of the heat exchangers T_{hx} ($= P_{\mathrm{th}}(\mathrm{d}T/\mathrm{d}P)_{\mathrm{sat}}$). The output is taken to be the pressure in the displacer cylinder P_{d}, which directly relates to the height of the vapour-liquid interface in the displacer cylinder, y_{d} ($= P_{\mathrm{d}}/\rho_{\mathrm{wf}}g$, refer Section 2.3.1). Hence, the forward-loop transfer function $G_{\mathrm{LTP_{TL}}}(s)$ for the $\mathrm{LTP_{TL}}$ model is,

$$G_{\mathrm{LTP_{TL}}}(s) = -\frac{\alpha_{\mathrm{LTP_{TL}}}\delta_{\mathrm{LTP_{TL}}}\beta_{\mathrm{LTP_{TL}}}\gamma_{\mathrm{LTP_{TL}}}}{1 + s^2 C_{\mathrm{d}} L_{\mathrm{d}}}\,, \tag{4.9}$$

where $\alpha_{\mathrm{LTP_{TL}}}$, $\delta_{\mathrm{LTP_{TL}}}$, $\beta_{\mathrm{LTP_{TL}}}$ and $\gamma_{\mathrm{LTP_{TL}}}$ are four sub-systems, shown in Fig. 4.2(a), which are a function of the electrical component impedances and are given in Table 4.2.

The total impedance of the circuit representing the $\mathrm{LTP_{TL}}$ model (Fig. 4.2(a)), is required to determine the forward-loop transfer function in Eq. (4.9), and this is found from combining impedance contributions in series and parallel as appropriate, such that,

$$Z_{\mathrm{TOT,LTP_{TL}}} \equiv \frac{P_{\mathrm{th}}}{U_{\mathrm{th}}} = R_{\mathrm{th}} + ({Z_{\mathrm{TL}}}^{-1} + ((sC_{\mathrm{ad}} + (Z_{\mathrm{l}} + ((Z_{\mathrm{f}} + Z_{\mathrm{d}})^{-1} + {Z_{\mathrm{p}}}^{-1})^{-1})^{-1})^{-1})^{-1})^{-1}\,, \tag{4.10}$$

where Z_{TL} is the thermal loss given by Eqs. (4.7) and (4.8), $Z_{\mathrm{l}} = R_{\mathrm{l}} + sL_{\mathrm{l}}$, $Z_{\mathrm{p}} = sL_{\mathrm{p}} + 1/sC_{\mathrm{p}}$, $Z_{\mathrm{f}} = R_{\mathrm{f}} + sL_{\mathrm{f}}$ and $Z_{\mathrm{d}} = sL_{\mathrm{d}} + 1/sC_{\mathrm{d}}$, are the impedances associated with the load, power cylinder, feedback and displacer cylinder, respectively. These impedances are a function of the parameters defined in Table 4.1.

In order to close the set of equations and solve the system, an additional relation between the input P_{th} and output P_{d} is required. This feedback relation is demonstrated in Fig. 2.5. In the $\mathrm{LTP_{TL}}$ model, the feedback constant $k_{\mathrm{LTP_{TL}}}$ is found from the imposed linear temperature gradient in the heat exchangers, such that $P_{\mathrm{th}} = k_{\mathrm{LTP_{TL}}} P_{\mathrm{d}}$ (shown in Fig. 4.2(a)), where $k_{\mathrm{LTP_{TL}}} = (\mathrm{d}T_{\mathrm{hx}}/\mathrm{d}y)/\rho_{\mathrm{wf}} g(\mathrm{d}T/\mathrm{d}P)_{\mathrm{sat}}$. Thus, it can be seen that the feedback gain $k_{\mathrm{LTP_{TL}}}$ is proportional to the temperature gradient in the heat exchangers, $\mathrm{d}T_{\mathrm{hx}}/\mathrm{d}y$. At the point of marginal stability, that is the condition in a linear system at which continuous sustained oscillations are observed, the feedback gain will give an indication of the minimum temperature gradient in the heat exchangers required to achieve this state.

4.2.4 Dynamic heat exchanger (DHX)

An electrical circuit representing the $\mathrm{DHX_{TL}}$ model can be formed by converting from a current input system to a voltage input system using the Norton-Thévenin theorem, and using the relations developed in Sections 2.3.1 and 4.2. The conversion creates the voltage source $P_{\mathrm{th}} = k_{\mathrm{DHX_{TL}}} P_{\mathrm{d}}/s$, which includes the feedback constant $k_{\mathrm{DHX_{TL}}}$. The circuit is shown in Fig. 4.2(b).

The forward-loop transfer function in the DHX model, $G_{\mathrm{DHX_{TL}}}(s)$, relating P_{th} (the pressure input representing the volumetric flow-rate in U_{th}) to output P_{d} is,

$$G_{\mathrm{DHX_{TL}}}(s) = -\frac{\alpha_{\mathrm{DHX_{TL}}} \delta_{\mathrm{DHX_{TL}}} \beta_{\mathrm{DHX_{TL}}} \gamma_{\mathrm{DHX_{TL}}}}{1 + s^2 C_{\mathrm{d}} L_{\mathrm{d}}}\,, \tag{4.11}$$

where $\alpha_{\mathrm{DHX_{TL}}}$, $\delta_{\mathrm{DHX_{TL}}}$, $\beta_{\mathrm{DHX_{TL}}}$ and $\gamma_{\mathrm{DHX_{TL}}}$ are four sub-systems, shown in Fig. 4.2(b), which are a function of the electrical component impedances and are given in Table 4.2.

For this model, the total impedance is,

$$Z_{\mathrm{TOT,DHX_{TL}}} \equiv \frac{P_{\mathrm{th}}}{U_{\mathrm{th}}} = R_{\mathrm{th}} + (sC_{\mathrm{hx}})^{-1} + (Z_{\mathrm{TL}}{}^{-1} + ((sC_{\mathrm{ad}} + (Z_{\mathrm{l}} + ((Z_{\mathrm{f}} + Z_{\mathrm{d}})^{-1} + Z_{\mathrm{p}}{}^{-1})^{-1})^{-1})^{-1})^{-1})^{-1}\,. \tag{4.12}$$

As with the LTP, the solution of the DHX model requires an additional relation between P_{th} and P_{d}. In the $\mathrm{DHX_{TL}}$ model, the feedback gain $k_{\mathrm{DHX_{TL}}}$ appearing in the feedback relation $P_{\mathrm{th}} = k_{\mathrm{DHX_{TL}}} P_{\mathrm{d}}/s$ is given by $k_{\mathrm{DHX_{TL}}} = (\mathrm{d}\dot{Q}_{\mathrm{hx}}/\mathrm{d}y)/\rho_{\mathrm{wf}} g \rho_{\mathrm{g,0}} \Delta s_{\mathrm{fg}} T_0 C_{\mathrm{hx}}$. It can be seen that the feedback gain is proportional to the power gradient in the heat exchangers, $\mathrm{d}\dot{Q}_{\mathrm{hx}}/\mathrm{d}y$. At the point of marginal stability, the feedback gain in

DHX model gives an indication of the minimum power required to achieve sustained oscillations.

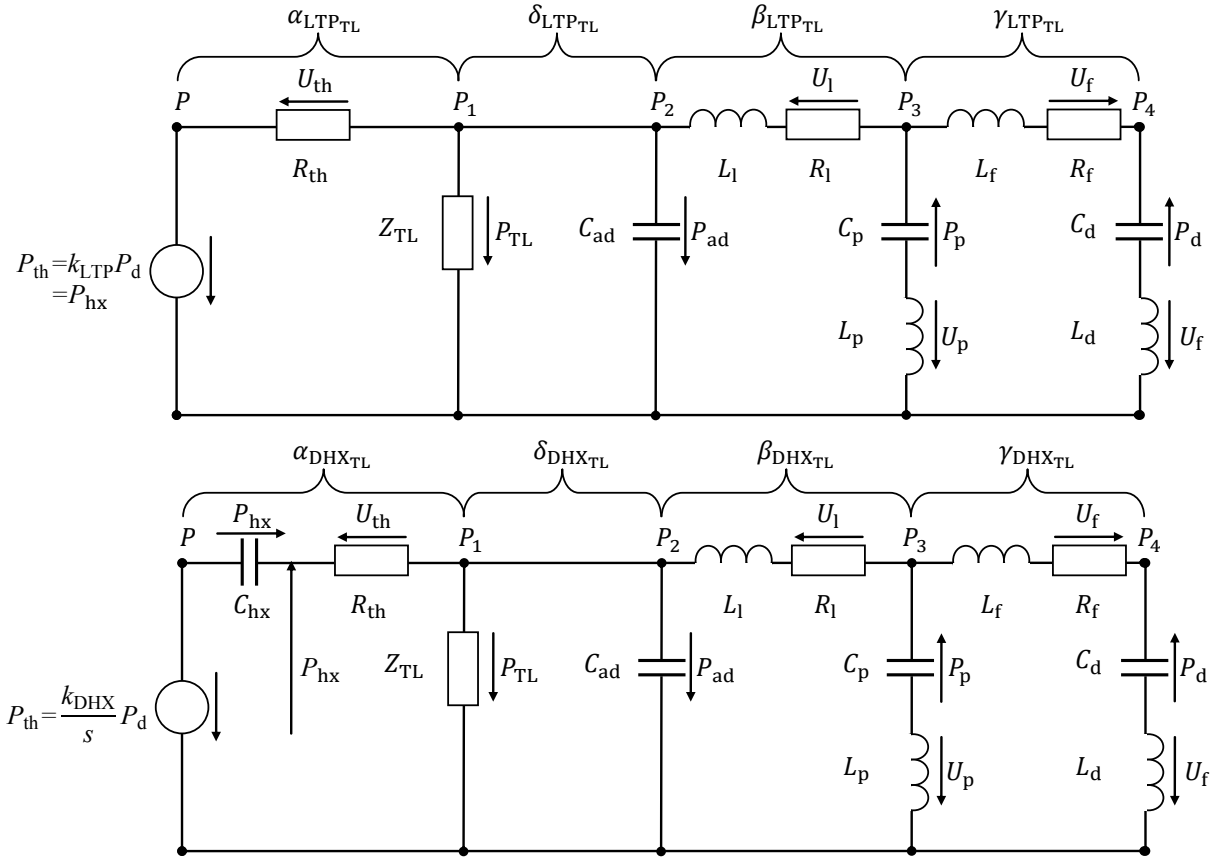


Figure 4.2: Electrical circuit representations of the NIFTE (see Fig. 1.7) for the: (a) $\mathrm{LTP_{TL}}$; and (b) $\mathrm{DHX_{TL}}$ models, where k_j corresponds to the feedback gain for model 'j', R_i to a resistance, C_i to a capacitance, L_i to an inductance, P_i to a pressure and U_i to a volumetric flow-rate. Subscript 'hx' refers to the heat exchangers, 'th' to the thermal domain, 'TL' to the unsteady thermal loss, 'ad' to the adiabatic vapour volume, 'l' to the load, 'p' to the power cylinder, 'd' to the displacer cylinder, and 'f' to the feedback line and valve.

4.3 Redefining feedback and load resistances

In the studies carried out in Chapter 3, the definition of the feedback resistance R_{f} and load resistance R_{l} was based upon the major head losses due to flow through a pipe, that is losses due to the wall friction. However, the feedback and load tubes in the prototype are short in length, so minor head losses from the valves are expected to have a greater contribution to the total head losses relative to the major head losses

from viscous effects [53]. We therefore amend our previous definition for the resistances and only consider the minor head losses due to valve constriction.

Hence, the pressure drop across the feedback valve P_f can be related to the bulk (volumetric area-averaged) liquid velocity u_f through the feedback tube [53] via,

$$P_\mathrm{f} = k_\mathrm{v}(\xi)\left[\frac{1}{2}\rho_\mathrm{wf}u_\mathrm{f}^2\right] = k_\mathrm{v}(\xi)\left[\frac{1}{2}\rho_\mathrm{wf}\left(\frac{U_\mathrm{f}}{A_\mathrm{f}}\right)^2\right], \tag{4.13}$$

where k_v is the (dimensionless) loss coefficient, which is a function of valve opening ξ, ρ_wf is the density of the working fluid in the liquid phase, and the fluid velocity u_f can be written in terms of the volumetric flow-rate U_f and the cross-sectional area of the feedback tube A_f.

Now, to form a linear form of Eq. (4.13), we can differentiate this with respect to U_f,

$$\frac{\mathrm{d}P_\mathrm{f}}{\mathrm{d}U_\mathrm{f}} = k_\mathrm{v}(\xi)\,\frac{\rho_\mathrm{wf}U_\mathrm{f}}{A_\mathrm{f}^2}\,. \tag{4.14}$$

Assuming there are only small perturbations around the time-averaged volumetric flow-rate in the feedback, U_f (on the right-hand side of Eq. (4.14)) is taken to be the time-averaged volumetric flow-rate in the feedback $\overline{U}_\mathrm{f}$ and the differential on the left-hand side is taken to the ratio of the fluctuations, such that,

$$\frac{P_\mathrm{f}}{U_\mathrm{f}} = k_\mathrm{v}(\xi)\,\frac{\rho_\mathrm{wf}\overline{U}_\mathrm{f}}{A_\mathrm{f}^2}\,, \tag{4.15}$$

where R_f is the resistance to flow due to the valve in the feedback tube. Comparing Eq. (4.15) to the characteristic equation for a resistor in Eq. (2.1), and using the aforementioned analogies between the fluid and the electrical domains, where pressure is represented by voltage and volumetric flow-rate is represented by current, the resistance (in the electrical domain) to flow through the feedback valve is,

$$R_\mathrm{f} \equiv \frac{P_\mathrm{f}}{U_\mathrm{f}} = k_\mathrm{v}(\xi)\,\frac{\rho_\mathrm{wf}\overline{U}_\mathrm{f}}{A_\mathrm{f}^2}\,. \tag{4.16}$$

The fluid flow through the load line can be dealt with in a similar way to the fluid flow through the

feedback connection, such that the resistance to flow due to the valve in the load can be found from,

$$\frac{P_\mathrm{l}}{U_\mathrm{l}} = k_\mathrm{v}(\xi)\,\frac{\rho_\mathrm{w}\overline{U}_\mathrm{l}}{A_\mathrm{l}^2} \equiv R_\mathrm{l}\,, \tag{4.17}$$

where ρ_w is the density of the pumped fluid (in the case of the prototype, water), $\overline{U}_\mathrm{l}$ is the mean volumetric flow-rate in the load, and A_l is the cross-sectional area of the load tube. Therefore, the resistance due to flow through the load valve is $R_\mathrm{l} = k_\mathrm{v}\rho_\mathrm{w}\overline{U}_\mathrm{l}/A_\mathrm{l}^2$. In both R_f and R_l above, k_v is a dimensionless valve loss coefficient, which is a function of valve opening ξ.

Table 4.1: Electrical analogies in the NIFTE and relations for resistances (R_i), capacitances (C_i) and inductances (L_i). Note that $\overline{U}_i$ denotes the time-averaged volumetric flow-rate, U, in component i.

Electrical Element	**Thermal-Fluid Effect**	**Parameter Expression**
Resistance (R)	Thermal resistance	$R_\mathrm{th} = \rho_{\mathrm{g},0}T_0\Delta s_\mathrm{fg}/hA_\mathrm{s}(\mathrm{d}T/\mathrm{d}P)_\mathrm{sat}$
	Load flow resistance (viscous/pressure drag)	$R_\mathrm{l} = k_\mathrm{v}(\xi)\rho_\mathrm{w}\overline{U}_\mathrm{l}/A_\mathrm{l}^2$
	Feedback valve flow resistance (drag)	$R_\mathrm{f} = k_\mathrm{v}(\xi)\rho_\mathrm{wf}\overline{U}_\mathrm{f}/A_\mathrm{f}^2$
Capacitance (C)	Vapour compressibility	$C_\mathrm{ad} = V_{\mathrm{g},0}/\gamma P_0$
	Power cylinder hydrostatic capacitance	$C_\mathrm{p} = A_\mathrm{p}/\rho_\mathrm{wf}g$
	Displacer cylinder hydrostatic capacitance	$C_\mathrm{d} = A_\mathrm{d}/\rho_\mathrm{wf}g$
	Heat exchanger heat storage capacitance	$C_\mathrm{hx} = m_\mathrm{al}c_\mathrm{al}(\mathrm{d}T/\mathrm{d}P)_\mathrm{sat}/\rho_{\mathrm{g},0}\Delta s_\mathrm{fg}T_0$
Inductance (L)	Load inertia (fluid mass)	$L_\mathrm{l} = \rho_\mathrm{w}l_\mathrm{l}/A_\mathrm{l}$
	Power cylinder inertia	$L_\mathrm{p} = \rho_\mathrm{wf}l_\mathrm{p}/A_\mathrm{p}$
	Displacer cylinder inertia	$L_\mathrm{d} = \rho_\mathrm{wf}l_\mathrm{d}/A_\mathrm{d}$
	Feedback tube inertia	$L_\mathrm{f} = \rho_\mathrm{wf}l_\mathrm{f}/A_\mathrm{f}$
Thermal loss	Exergy loss	$a = T_0\rho_{\mathrm{g},0}\Delta s_\mathrm{fg}\alpha_\mathrm{gl}^{0.5}/A_\mathrm{g}(\mathrm{d}T/\mathrm{d}P)_\mathrm{sat}k_\mathrm{gl}$
	Exergy loss	$b = l_\mathrm{gl}/\alpha_\mathrm{gl}^{0.5}$
	Condensation loss	$c = \rho_{\mathrm{g},0}T_0\Delta s_\mathrm{fg}/hA_\mathrm{gl}(\mathrm{d}T/\mathrm{d}P)_\mathrm{sat}$

Table 4.2: Transfer functions for the $\mathrm{LTP_{TL}}$ and $\mathrm{DHX_{TL}}$ models shown in Fig. 4.2.

	$\alpha = \frac{P_1}{P}$	$\delta = \frac{P_2}{P_1}$	$\beta = \frac{P_3}{P_2}$	$\gamma = \frac{P_4}{P_3}$
$\mathrm{LTP_{TL}}$	$1 - \frac{R_\mathrm{th}}{Z_{\mathrm{TOT,LTP_{TL}}}}$	1	$1 - Z_\mathrm{l}(\frac{1}{\alpha_\mathrm{LTP}Z_{\mathrm{TOT,LTP_{TL}}}} - \frac{1}{Z_\mathrm{TL}} - sC_\mathrm{ad})$	$1/(1 + \frac{Z_\mathrm{f}}{Z_\mathrm{d}})$
$\mathrm{DHX_{TL}}$	$1 - \frac{R_\mathrm{th}+1/sC_\mathrm{hx}}{Z_{\mathrm{TOT,DHX_{TL}}}}$	1	$1 - Z_\mathrm{l}(\frac{1}{\alpha_\mathrm{DHX}Z_{\mathrm{TOT,DHX_{TL}}}} - \frac{1}{Z_\mathrm{TL}} - sC_\mathrm{ad})$	$1/(1 + \frac{Z_\mathrm{f}}{Z_\mathrm{d}})$

4.4 Results

The LTP and DHX models including and excluding the thermal loss parameter (impedance Z_{TL}) are compared to the experimental data from Ref. [2], where the effects of varying the feedback resistance R_{f} and load resistance R_{l} are investigated, as summarised in Tables 4.5 and 4.4. The majority of the electrical parameters defined in Table 4.1 are evaluated at the configuration of the experimental setup given in Ref. [2], known as the nominal values for the parameters. However there were some parameters whose values could not be easily ascertained; these are discussed in Section 4.4.1, below.

4.4.1 Parameter uncertainties

Firstly, a comparison is made between the values of the electrical parameters of the NIFTE as defined in Table 4.1. The results of the comparison are summarised in Table 4.3, which shows the values presented by Smith [2] and those calculated independently here, based on the experimental configuration and setup of the NIFTE prototype that is described in great detail in Ref. [2]. Since the model presented in Ref. [2] neglected the effects of inertia, no values for the inductances due inertia are given and therefore no comparison can be made. Further to this, the heat exchanger capacitance C_{hx} is a new parameter only included in the original DHX model, and subsequently also the $\mathrm{DHX_{TL}}$ models. The uncertainties relating to its value are discussed further in Section 4.4.1.

A small discrepancy can be identified between the thermal resistance parameters suggested in Ref. [2] and those re-calculated here from Eq. (2.25), as shown in Table 4.3. On comparing these two values for R_{th} we have concluded that there is little difference in the predicted results (e.g. oscillation frequency) for the NIFTE, both from the LTP and the DHX models. Hence, our re-calculated value for the thermal resistance of $R_{\mathrm{th}} = 4.80 \times 10^{8}\ \mathrm{kg\,m^{-4}\,s^{-1}}$ is used throughout in this work. There is also a small discrepancy in the value for the hydrostatic capacitance in the power cylinder C_{p}, though the difference is less than 1 % and therefore deemed negligible. No definite value for the feedback connection resistance R_{f} or hydrostatic capacitance in the displacer cylinder C_{d} is presented in Ref. [2]. Instead, a range is provided for the latter, which is given in Table 4.3, from which a weighted average is taken for the value of C_{d}. Our re-calculated value for C_{d} falls within the provided range.

The two main parameters which can be easily controlled in the NIFTE device are the feedback and

load resistances. Both of these parameters depend on the position of the respective valves in these components, which affects the loss coefficient $k_v(\xi)$. The value for the (fixed) load resistance R_l used in a set of experiments described in Ref. [2] in which R_l was fixed and the feedback resistance R_f was varied has been determined experimentally. This value is provided in Ref. [2] and is discussed further in the relevant Section 4.4.1. In reporting a second set of experiments with a varying load resistance R_l and with a fixed feedback resistance R_f, no information is given about the valve position or concerning the value for R_f. This is dealt with in Section 4.4.1. The final parameters which are investigated further are the thermal loss parameters a and c, which were found in Section 4.2 to relate to the thermal loss impedance Z_{TL}. These parameters are discussed in Section 4.4.1.

Table 4.3: Comparison of parameter values presented in Ref. [2] and the values of the parameters in Table 2.2 considered here as best estimates for the *nominal* experimental configuration of the NIFTE prototype.

Parameter	**Values from Ref. [2]**	**Estimated Value**	**Units**
R_f	none given [*]	2.62×10^7	$\mathrm{kg\,m^{-4}\,s^{-1}}$
R_l	1.55×10^9	9.76×10^9	$\mathrm{kg\,m^{-4}\,s^{-1}}$
R_{th}	8.00×10^8	4.80×10^8	$\mathrm{kg\,m^{-4}\,s^{-1}}$
C_p	7.38×10^{-8}	7.43×10^{-8}	$\mathrm{m^4\,s^2\,kg^{-1}}$
C_d	7.59×10^{-8} to 2.15×10^{-7} [†]	8.36×10^{-8}	$\mathrm{m^4\,s^2\,kg^{-1}}$
C_{ad}	3.70×10^{-9}	2.24×10^{-9}	$\mathrm{m^4\,s^2\,kg^{-1}}$
C_{hx} (DHX only)	n/a	3.78×10^{-9}	$\mathrm{m^4\,s^2\,kg^{-1}}$
L_p	n/a	3.77×10^5	$\mathrm{kg\,m^{-4}}$
L_d	n/a	1.58×10^5	$\mathrm{kg\,m^{-4}}$
L_f	n/a	4.74×10^6	$\mathrm{kg\,m^{-4}}$
L_l	n/a	1.51×10^7	$\mathrm{kg\,m^{-4}}$

[*] No value for the feedback resistance was stated in Ref. [2], and one could not be recalled in recent communication [61].

[†] The value of the hydrostatic capacitance in the displacer was taken as a weighted average between these two presented values, though the exact value used was not stated.

Load resistance R_l

For a set of experiments with varying feedback resistance R_f, the load resistance is given as $R_l = 1.55 \times 10^9$ $\mathrm{kg\,m^{-4}\,s^{-1}}$ in Ref. [2]. From personal communication with the author [61], it was noted that only

the evaporation and outwards displacement phase of the NIFTE operation was taken into account in determining this value of R_l, neglecting (in fact, discounting) the condensation and suction phase. Using the experimental data given in Ref. [2], an average of the resistances during both phases of the NIFTE operation can be taken. The resulting average load resistance R_l is found to be 9.08×10^8 kg m^{-4} s^{-1}. At the same time a load valve opening of $\xi = 10$ % corresponds to an R_l value of 9.76×10^8 kg m^{-4} s^{-1}. Given that this value falls in between the value presented in Ref. [2] and our re-calculated average, it is deemed a suitable value for the load resistance R_l, and is used for all runs with varying feedback resistance R_f, the results of which are presented in Sections 4.4.2 and 4.4.2.

Table 4.4: Data from experiments with a varying R_l reported in Ref. [2], where R_l is the load resistance, $\omega_0 = 2\pi f_0$ is the angular frequency and f_0 is the oscillation frequency.

R_l [kg m^{-4} s^{-1}]	ω_0 [rad s^{-1}]	f_0 [Hz]
0.32	0.83	0.13
0.33	0.84	0.13
0.34	0.86	0.14
0.40	0.84	0.13
0.46	0.81	0.13
0.48	0.80	0.13
0.51	0.77	0.12
0.57	0.74	0.12
0.73	0.69	0.11
0.84	0.64	0.10
1.19	0.56	0.09
2.40	0.39	0.06

Feedback resistance R_f

Experimental data relating to the NIFTE operation on varying the feedback valve resistance R_f with all other parameters being constant, including the hydrostatic capacitance in the displacer cylinder C_d and the load resistance R_l [61], are given in Ref. [2] and summarised in Table 4.5. The minimum opening (maximum closing) of the feedback valve over this set of experiments corresponding to the largest reported value of $R_f C_d$ in Ref. [2] has been found to be $\xi \sim 41.4$ %. This calculation was based on the definition of R_f in Table 4.1, a loss coefficient $k_v(\xi)$ evaluated from a data-based correlation provided in Ref. [62], a value for the mean volumetric flow-rate in the feedback tube $\overline{U}_f$ of 8.8 L h^{-1} (from the known oscillation frequency

f_0, and the amplitude $\hat{y}_d$ and cross-sectional area A_d of the displacer cylinder; $\overline{U}_f = 4A_d f_0 \hat{y}_d/\pi$), and our value of C_d as reported in Table 4.3.

It was noted in Ref. [61] that the experimental data points for $R_f C_d$ in Ref. [2] were scaled by an arbitrary constant of proportionality while obeying an inverse relationship to the valve opening ξ. In the present study the points have been scaled to reflect a minimum feedback valve opening of $\xi = 40$ %, while obeying the ratios reported in Ref. [2]. The revised scaled values for $R_f C_d$ are given in Table 4.5 and deviate from the points given in Ref. [2] by approximately 15 %.

In a second set of experiments data was generated over a range of load resistances R_l, and at a constant but unknown position of the feedback valve [61]. The frequency of oscillation ω_0 at a load resistance of $R_l = 1.55\times10^9$ kg m^{-4} s^{-1} is reported in Ref. [2] (see Table 4.4) as being 0.48 rad s^{-1}. The value of $R_f C_d$ that corresponds to this ω_0 in Table 4.5 has been used to find the feedback resistance, $R_f = 2.62\times10^7$ kg m^{-4} s^{-1}, and corresponds to a feedback valve opening of $\xi = 33$ %. This (constant) value for the feedback valve resistance R_f is used in all runs performed with a varying load resistance R_l.

Table 4.5: Data from experiments with a varying R_f reported in Ref. [2], where R_f is the feedback resistance, C_d is the hydrostatic capacitance in the displacer cylinder, $\omega_0 = 2\pi f_0$ is the angular frequency, τ is the period and η_{ex} is the device exergetic efficiency. The re-scaled $R_f C_d$ values are based on a minimum feedback valve opening of $\xi = 40$ %.

$R_f C_d$ [s]	**Re-scaled** $R_f C_d$ [s]	ω_0 [rad s^{-1}]	τ [s]	η_{ex} [%]
0.43	0.53	1.11	5.6	0.37
0.62	0.66	0.89	7.1	1.12
0.82	0.88	0.78	8.1	1.40
1.01	1.15	0.72	8.6	1.40
1.21	1.37	0.65	9.2	1.60

Thermal loss parameters a and c

In this study, the potential of including the thermal loss, through a thermal loss impedance Z_{TL}, into the models to account for the discrepancies in the predicted efficiencies is investigated. From the definitions of the thermal loss parameters a and c (given in Table 4.1), it can be seen that these parameters depend on the area available for heat transfer and phase change over the walls, A_{gl}. The exact area that participates in this process is unknown, and so we use the maximum possible extent for A_{gl}, given the known geometry of the

prototype NIFTE, in order to calculate the thermal loss parameters a and c.

Heat exchanger capacitance C_{hx}

The ability of the heat exchanger blocks to store energy, described by parameter C_{hx}, is proportional to the mass m_{al} (and thus also the height) of the heat exchangers that participate in the phase-change heat transfer process. As described in Section 2.3.2, a typical value for the height of the heat exchangers that is washed by liquid $\hat{y}_{C_{\mathrm{hx}}}$ was estimated by video observation at about 7 mm. Nevertheless, there remains an uncertainty in estimating the 'active' heat exchanger height. The uncertainty arises due to the fact that it is possible that only a fraction of the total 7 mm height of the heat exchangers exhibits strong temperature changes during heat transfer process.

Two values of C_{hx} are investigated, corresponding to the cases: (i) 1/2 of the washed heat exchanger height $\hat{y}_{C_{\mathrm{hx}}}$ participates in the heat exchange process, which is equivalent to a heat exchanger height of 3.5 mm; and, (ii) 1/4 of the washed heat exchanger height $\hat{y}_{C_{\mathrm{hx}}}$ participates in the heat exchange process, equivalent to a heat exchanger height of 1.75 mm. The values of C_{hx} are given in Table 4.6. Case (ii) is taken to be the nominal value for heat exchanger capacitance $\widetilde{C}_{\mathrm{hx}}$.

Table 4.6: Investigated ranges and nominal values for the parameters defined in Table 2.2.

Parameter	**Investigated Range (Nominal Value)**	**Units**
R_{f}	6.57×10^{5} to 2.17×10^{9} (2.62×10^{7})	$\mathrm{kg\,m^{-4}\,s^{-1}}$
R_{l}	1.26×10^{6} to 1.40×10^{9} (9.76×10^{9})	$\mathrm{kg\,m^{-4}\,s^{-1}}$
R_{th}	(4.80×10^{8})	$\mathrm{kg\,m^{-4}\,s^{-1}}$
C_{p}	(7.43×10^{-8})	$\mathrm{m^{4}\,s^{2}\,kg^{-1}}$
C_{d}	(8.36×10^{-8})	$\mathrm{m^{4}\,s^{2}\,kg^{-1}}$
C_{ad}	(2.24×10^{-9})	$\mathrm{m^{4}\,s^{2}\,kg^{-1}}$
C_{hx} (DHX only)	(9.46×10^{-10} & 1.89×10^{-9})	$\mathrm{m^{4}\,s^{2}\,kg^{-1}}$
L_{p}	(3.77×10^{5})	$\mathrm{kg\,m^{-4}}$
L_{d}	(1.58×10^{5})	$\mathrm{kg\,m^{-4}}$
L_{f}	(4.74×10^{6})	$\mathrm{kg\,m^{-4}}$
L_{l}	(1.51×10^{7})	$\mathrm{kg\,m^{-4}}$
a	7.52×10^{7} to 8.76×10^{7} (8.06×10^{7})	$\mathrm{kg\,m^{-4}\,s^{-1.5}}$
b	(4.31×10^{0})	$\mathrm{s^{-0.5}}$
c	2.94×10^{7} to 3.43×10^{7} (3.15×10^{7})	$\mathrm{kg\,m^{-4}\,s^{-1}}$

4.4.2 Comparison with experimental data

In Section 4.4.2, the LTP and DHX models, including and excluding the thermal loss impedance Z_{TL} are compared with respect to the following performance indicators: (i) oscillation frequency f_0; and (ii) exergetic efficiency η_{ex}. The models are compared to experimental data obtained from Ref. [2], which are also summarised in Tables 4.5 and 4.4. In Section 4.4.3 we proceed further by comparing and discussing the thermodynamic cycles that arise in these models.

Varying load resistance R_{l}

The effect of varying the load resistance R_{l} on the frequency of oscillation f_0 of the NIFTE is shown in Fig. 4.3(a). Since the inclusion of the thermal loss impedance Z_{TL} was found to have little effect on the frequencies predicted by the LTP model and by the DHX model, results are shown here of the frequencies predicted by the LTP or DHX models, in both cases without the thermal loss impedance Z_{TL}. These results are also representative of the $\mathrm{LTP_{TL}}$ and $\mathrm{DHX_{TL}}$ models. Also shown in this plot are experimental data from the NIFTE prototype, with a hot heat exchanger temperature of 65 °C and 90 °C [2]. Note that the plotted values of the load resistance R_{l}, including those from the experiments, are normalised to the nominal value $\widetilde{R}_{\mathrm{l}}$ of the load resistance, such that $R_{\mathrm{l}}{}^{*} = R_{\mathrm{l}}/\widetilde{R}_{\mathrm{l}}$.

The general trend from the model predictions is for an increase in R_{l} to lead to a monotonic decrease in oscillation frequency f_0, which is expected to occur as an increase in resistance in the load will lead to a decrease in velocity through the load, and therefore a decrease in frequency of oscillation. This is in agreement with the trend observed in the experimental results. Further to this is can be seen that the experimental points lie between the two C_{hx} values used in the DHX model: the nominal value $\widetilde{C}_{\mathrm{hx}}$ (dashed line) and $2\widetilde{C}_{\mathrm{hx}}$ (dotted line). Although the LTP model predicts the correct trend, it estimates frequencies about two times those observed experimentally.

The effect of varying the load resistance R_{l} on the exergetic efficiency of the NIFTE device η_{ex} is shown in Fig. 4.3(b). In the DHX model, the gradual increase in load resistance R_{l} leads to a continuous increase in the predicted efficiencies η_{ex}. In the LTP model, on the other hand, a maximum efficiency is observed at $R_{\mathrm{l}}{}^{*} = 0.4$. This maximum has important implications, as it would seem to suggest that the NIFTE device in its defined configuration has an ‘optimal’ load with which it will exhibit its best performance in

terms of efficiency. In fact, this is difficult to conclude from these results because the feedback resistance is being kept constant over the set of results, whereas in a practical scenario this would have been adjusted as the load changed to match the new load. All models predict efficiencies less than 0.6 %, which is lower compared to those observed experimentally in the experiments with the varying feedback resistance R_f, which are presented and discussed in Section 4.4.2 below.

Varying feedback resistance R_f without thermal loss

The inertive LTP and DHX models excluding the thermal loss impedance Z_TL, previously presented in Chapter 2, are compared in this section to the experimental data for the NIFTE pump prototype from Ref. [2]. The effects of the feedback valve resistance R_f (and consequently of the time constant $R_\mathrm{f}C_\mathrm{d}$) on the oscillation frequency f_0 and the exergetic efficiency η_ex predicted by the LTP and DHX models are shown in Fig. 4.4(a) and (b), respectively. The experimental data is outlined in Table 4.5. All parameters are set to their nominal values as defined in Table 4.6, with the exception of the feedback valve resistance R_f which is varied. The results are presented as a function of the varying time constant $R_\mathrm{f}C_\mathrm{d}$, though it is important to note that the results were generated by varying the feedback resistance parameter R_f with a *constant* displacer cylinder capacitance C_d.

Frequency:

From the experimental results in Table 4.5 it can be seen that the practical NIFTE device operates at a frequency in the range $f_0 = 0.1 - 0.2$ Hz. Figure 4.4(a) shows that both the LTP and DHX models predict the correct qualitative trend for the frequency f_0, whereby an increase in the feedback resistance R_f always leads to a decrease in frequency f_0. Again, this trend is expected, as with increasing the resistance in the load, increasing the resistance in the feedback tube leads to an overall decrease in the velocity through the feedback tube, and therefore decrease in oscillation frequency. The DHX model at the nominal value of heat exchanger capacitance $\widetilde{C}_\mathrm{hx}$ (recall that this reflects an active heat exchanger height amplitude $\hat{y}_{C_\mathrm{hx}}$ of 1.75 mm) is associated with a slightly better prediction of the magnitude of the frequency f_0 compared to those of the DHX model with twice the nominal heat exchanger capacitance $2\widetilde{C}_\mathrm{hx}$ and those of the LTP model. Specifically, the nominal DHX model with $C_\mathrm{hx} = \widetilde{C}_\mathrm{hx}$ underpredicts the experimentally obtained frequencies f_0 by $\sim 20 - 35$ % over the range of investigated $R_\mathrm{f}C_\mathrm{d}$, while the DHX model with $C_\mathrm{hx} = 2\widetilde{C}_\mathrm{hx}$ underpredicts the experimental f_0 by $35 - 45$ % and the LTP model overpredicts the same data by $45 - 80$ %.

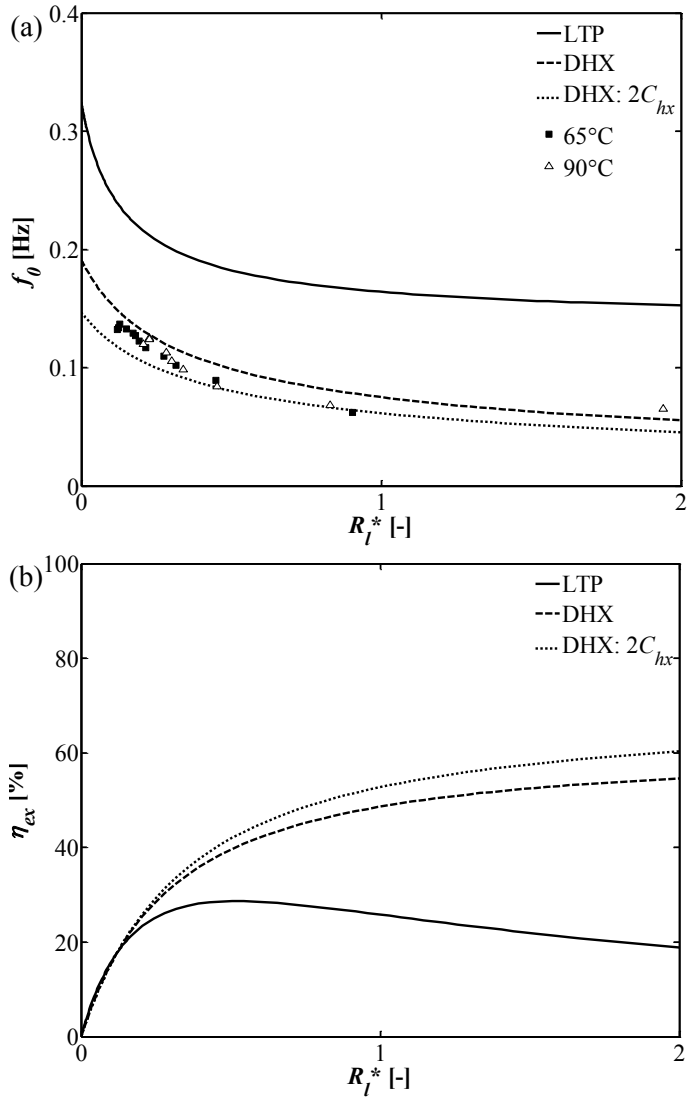


Figure 4.3: The effect of load resistance R_l on the: (a) frequency of oscillation (operation) f_0; and (b) exergetic efficiency η_ex. Results are shown from the LTP model (solid line), nominal DHX model (dashed line), and DHX model with twice the nominal heat exchanger capacitance value $2\widetilde{C}_\mathrm{hx}$ (dotted line). Also shown are experimental data points from a NIFTE water pump prototype.

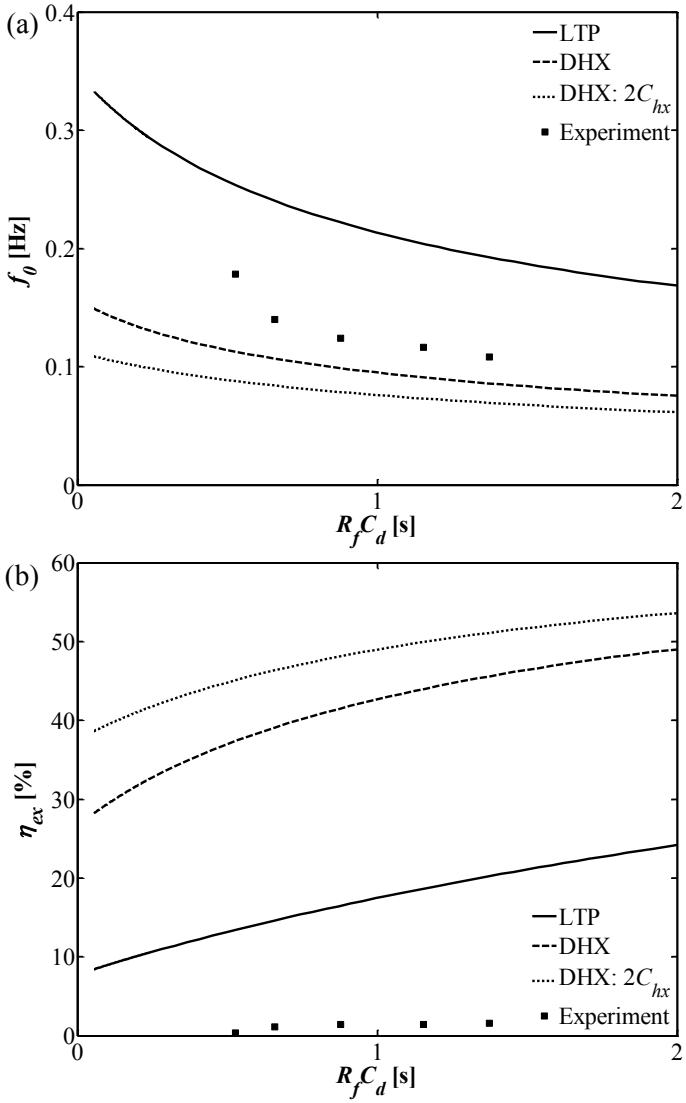


Figure 4.4: The effect of the timescale parameter $R_{\mathrm{f}}C_{\mathrm{d}}$ at constant displacer hydrostatic capacitance C_{d} on the predictions of the NIFTE: (a) frequency f_0; and (b) exergetic efficiency η_{ex}. Showing results from the LTP model (solid line), nominal DHX model (dashed line), and DHX model with $2\widetilde{C}_{\mathrm{hx}}$ (dotted line).

Frequency predictions from the LTP and DHX models are given in Chapter 3 (e.g. Fig. 3.6(a)), where a trend for the frequency similar to that in Fig. 4.4(a) is shown. It is noted that the frequencies predicted by the DHX model in Fig. 4.4 are dampened compared to the range of values presented in Chapter 3. The most significant difference between the two models is the definition for the load resistance R_{l}. Initially, this was associated with pressure drop due to laminar flow in a pipe, while in the present work this is associated

with pressure drop through a valve and results in an increase in the value of the nominal load resistance $\widetilde{R}_\mathrm{l}$ by 2 orders of magnitude compared to the value used in Chapter 3. The higher resistance in the load is expected to slow down the NIFTE device.

Efficiency:

The corresponding variation of the exergetic efficiency η_ex predicted by the LTP and DHX NIFTE models, over the same range of $R_\mathrm{f}C_\mathrm{d}$, is compared to experimental data in Fig. 4.4(b). Both the LTP and DHX models indicate that an increase in feedback resistance R_f leads to an increase in the NIFTE efficiency η_ex. This is the same trend observed in the experimental results made available in Ref. [2], and is expected to occur. As mentioned, an increase in resistance in the feedback, or load, leads to a decrease in oscillation frequency. This in turn leads to a longer exposure time of the working fluid to the heat exchangers. As more heat is able to transfer to the working fluid instead of lost through the surroundings, it is expected that there will be a higher efficiency observed, Although both models capture this trend, they both significantly overestimate the exergetic efficiency of the device η_ex. In particular, the LTP model predicts an efficiency 11 times the experimentally obtained value, whilst the DHX model predicts an efficiency 30 times that obtained experimentally.

Varying feedback resistance R_f with thermal loss

The thermal loss impedances Z_TL that have been defined in Section 4.2 with isothermal or adiabatic boundary conditions on the *outside* of the NIFTE vapour region are included into the linear temperature profile model ($\mathrm{LTP_{TL}}$) and dynamic heat exchanger model ($\mathrm{DHX_{TL}}$). The effects of varying the feedback resistance R_f on the model frequency and efficiency predictions when the thermal loss impedances Z_TL are inserted into the NIFTE models are shown in Figs. 4.5 and 4.6, for the isothermal or adiabatic boundary condition cases respectively. On comparing the two figures, it can be concluded that the models predict similar oscillation frequencies and exergetic efficiencies irrespective of the boundary condition type used. Now, from Eq. (4.5) the ratio of the solid wall thickness to the diffusion lengthscale is found to be $l_\mathrm{gl}/\delta_\mathrm{gl} = 3$. A ratio greater than 1 would imply that the temperature and heat flux fluctuations on the inner surfaces in contact with the working fluid in the vapour region penetrate only certain distance into the solid wall. In this case, the characteristic distance of penetration is 1/3 of the thickness of the wall. As such, it would be expected that the choice of the boundary condition on the outside of the device will have a less significant role to

play in determining the conditions on the inside wall surface that is in contact with the working fluid, hence the similarities in the predictions shown in Fig. 4.5 and 4.6.

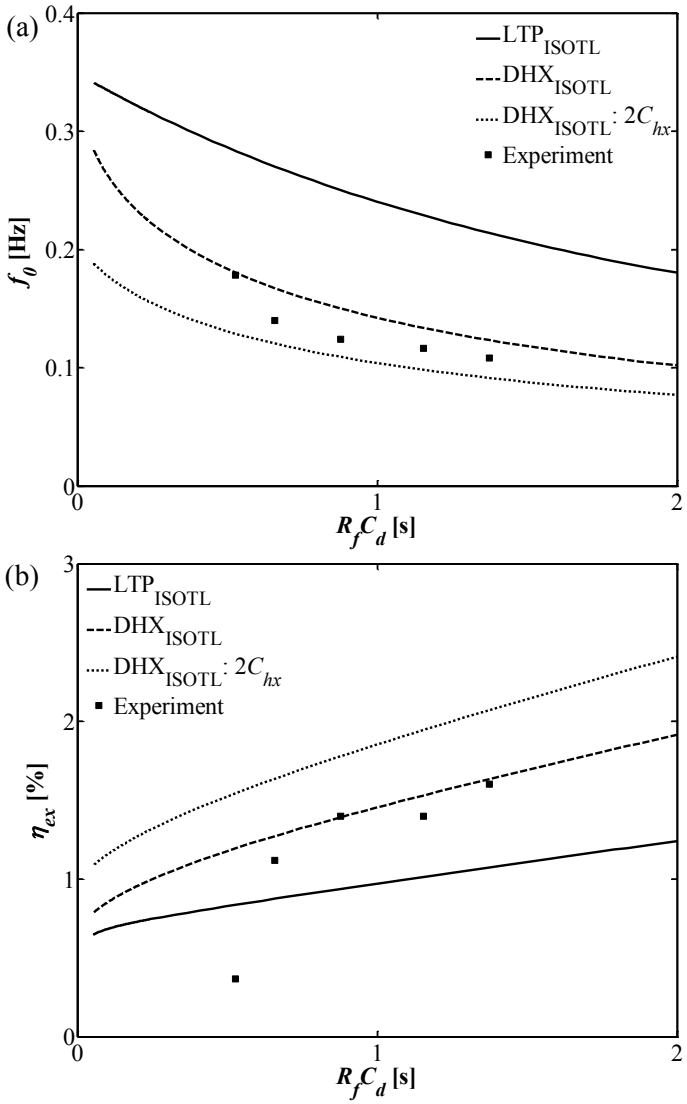


Figure 4.5: The effect of the timescale parameter $R_{\mathrm{f}}C_{\mathrm{d}}$ at constant displacer hydrostatic capacitance C_{d} on the predictions of the NIFTE: (a) frequency f_0; and (b) exergetic efficiency η_{ex}. Showing results for the revised models featuring the unsteady thermal loss impedance Z_{TL} with an *isothermal* boundary condition, namely $\mathrm{LTP}_{\mathrm{ISOTL}}$ (solid line), $\mathrm{DHX}_{\mathrm{ISOTL}}$ (dashed line), and $\mathrm{DHX}_{\mathrm{ISOTL}}$ with $2\widetilde{C}_{\mathrm{hx}}$ (dotted line).

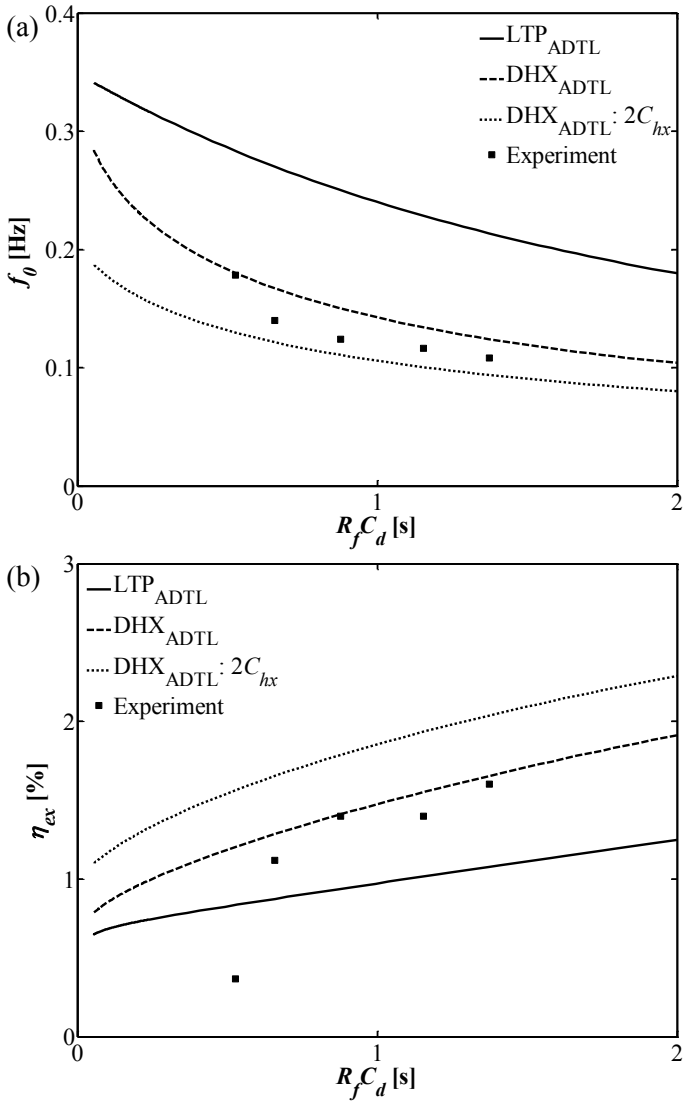


Figure 4.6: The effect of the timescale parameter $R_{\mathrm{f}}C_{\mathrm{d}}$ at constant displacer hydrostatic capacitance C_{d} on the predictions of the NIFTE: (a) frequency f_0; and (b) exergetic efficiency η_{ex}. Showing results for the revised models featuring the unsteady thermal loss impedance Z_{TL} with an *adiabatic* boundary condition, namely $\mathrm{LTP}_{\mathrm{ADTL}}$ (solid line), $\mathrm{DHX}_{\mathrm{ADTL}}$ (dashed line), and $\mathrm{DHX}_{\mathrm{ADTL}}$ with $2\widetilde{C}_{\mathrm{hx}}$ (dotted line).

Frequency:

Figures 4.5(a) and 4.6(a) show the oscillation frequency f_0 predicted by the models with the isothermal and adiabatic boundary conditions respectively, as the feedback resistance R_{f} is varied. On comparison to the predictions from the same models but without the thermal loss, shown in Fig. 4.4(a), the inclusion of

the thermal loss impedance Z_{TL} has little effect on oscillation frequency predicted by the LTP model. On the other hand, though the inclusion of this impedance in the DHX model does result in a slightly better prediction of the oscillation frequency f_0, with the experimental data points now lying between the model results from the nominal $\widetilde{C}_{\mathrm{hx}}$ (dashed line) and $2\widetilde{C}_{\mathrm{hx}}$ (dotted line).

Furthermore, it is useful to return to an assumption made in Ref. [2] with regards to the role of the shuttle losses in the operation of the NIFTE. Specifically, it was assumed in Ref. [2] that shuttle losses in the passive parts of the heat transfer region do not to significantly affect the *dynamics* of the oscillator. From the findings of the present work, we can conclude that this assumption is reasonable.

Efficiency:

The corresponding exergetic efficiency η_{ex} results from the $\mathrm{LTP_{TL}}$ and $\mathrm{DHX_{TL}}$ models are shown in Figs. 4.5(b) and 4.6(b). The thermal loss impedance Z_{TL} has a significant effect on the evaluated efficiencies, compared to those predicted by the same models while neglecting thermal losses, shown in Fig. 4.4(b). From Figs. 4.5 and 4.6 it can be seen that both the $\mathrm{LTP_{TL}}$ and $\mathrm{DHX_{TL}}$ models predict efficiencies with the correct trend, whereby a higher feedback resistance leads to a higher efficiency as demonstrated experimentally. In addition to this, both models predict efficiency values in the same order of magnitude as the experimental results. The $\mathrm{LTP_{TL}}$ model underestimates the efficiencies, while the $\mathrm{DHX_{TL}}$ model predicts the experimental data better, not only in terms of efficiency but also while simultaneously matching the measured frequency operation without adjustments to any of the parameters.

Focussing on the experimental data points in Figs. 4.5(b) and 4.6(b), it can be seen that the first data point at the lowest value of $R_{\mathrm{f}}C_{\mathrm{d}}$ deviates from the general trend, in particular with respect to the exergetic efficiency η_{ex}. Now, the overlap amplitude of the liquid level over the heat exchangers $\hat{y}_{C_{\mathrm{hx}}}$ is expected to change with the operating condition of the device, i.e. as R_{f} is varied, in response to the change in the total oscillation amplitude of the liquid level $\hat{y}_{\mathrm{d}}$ in the displacer cylinder in which the heat exchangers are located. Similarly, the oscillation amplitude of the liquid level in the power cylinder $\hat{y}_{\mathrm{p}}$ will also be affected. Together, these changes will affect the values of the heat exchanger capacitance C_{hx} and of the thermal loss impedance Z_{TL}. Simple numerical experimentation has shown that of these two developments the change in the capacitance C_{hx} is the greatest, and also, that the output of the DHX model in terms of the investigated performance indicators has the greatest sensitivity to this parameter. In the results shown thus far, results are presented for the DHX model with a single value for the heat exchanger capacitance C_{hx} (and a single

value of the thermal loss impedance Z_{TL}). A modelling attempt more able to capture this practical aspect could involve a *varying* C_{hx} as $R_{\mathrm{f}}C_{\mathrm{d}}$ is changed, yet it is difficult to predict a functional relationship between these two parameters without access to more detailed information on the running of the prototype, which is proprietary and not openly available. Nevertheless, qualitatively we expect that with an increase in $R_{\mathrm{f}}C_{\mathrm{d}}$ and the (known, e.g. from Figs. 4.5(a)) related decrease in the frequency f_0, we would have: (i) a greater $\hat{y}_{\mathrm{d}}$, giving rise to; (ii) a greater $\hat{y}_{C_{\mathrm{hx}}}$, and thus; (iii) a greater C_{hx}, and finally; (iv) a higher η_{ex}; exactly as observed in Figs. 4.5 and 4.6.

Further discussion:

Madhawa Hettiarachchi et al. [48] performed an excellent modelling study of an organic rankine cycle (ORC) engine operating with *n*-pentane across a temperature difference of approximately 60 K between the heat source and sink. The authors reported exergetic efficiencies of up to ~ 14 %, a value that is an order of magnitude higher than the exergetic efficiency currently predicted by the NIFTE models with heat loss and observed by the NIFTE prototype. At the same time: (i) the $30-65$ kW "Green Machine" by ElectraTherm is quoted by the manufacturer as having an exergetic efficiency of ~ 35 % when running with a hot water inlet temperature of 100 °C and a 20 °C cold water inlet temperature [20]; while (ii) ENERBasque's 25 kW "Prometheus" is quoted as having an exergetic efficiency of $32-34$ % when running with hot water at $90-95$ °C and cold water at $15-25$ °C [21], and $26-27$ % when running with hot water at 85 °C and the same cold water temperature.

It is important to point out that the NIFTE has a much simpler construction and should be a far more affordable solution than the systems proposed in Refs. [20, 21, 48], both in terms of capital costs and in terms of operating costs, including maintenance. Furthermore, the NIFTE is a much smaller system than the ElectraTherm and ENERBasque ORCs and it can be expected that certain performance benefits can come from scale-up, thanks to loss minimisation from the lower surface to volume ratios of larger machines. Even so, it is clear that there is a need to improve the performance of the early NIFTE prototype reported in Ref. [2], in particular with respect to efficiency and also in terms of power output, if this technology is to become of broader interest. Our results indicate that, with careful engineering design [43], much higher efficiencies are indeed possible. The present effort highlights a further important aspect of design, that of loss minimisation. Predictions without the thermal loss impedance result in considerably higher exergetic efficiencies, with the DHX at $\sim 30-50$ % and the LTP at $\sim 10-25$ %.

Finally, for the best fluid pumping performance, a high frequency f_0 and a high efficiency η_{ex} are desired, as the volumetric flow-rate pumped per unit heat available to the NIFTE is proportional to the product of f_0 (oscillation frequency) and η_{ex} (exergetic efficiency). From the trends of the experimental data for the NIFTE (c.f. Fig. 4.5), it can be seen that a high η_{ex} is achieved at low f_0. A compromise needs to be made between high efficiency and high flow-rate in the load.

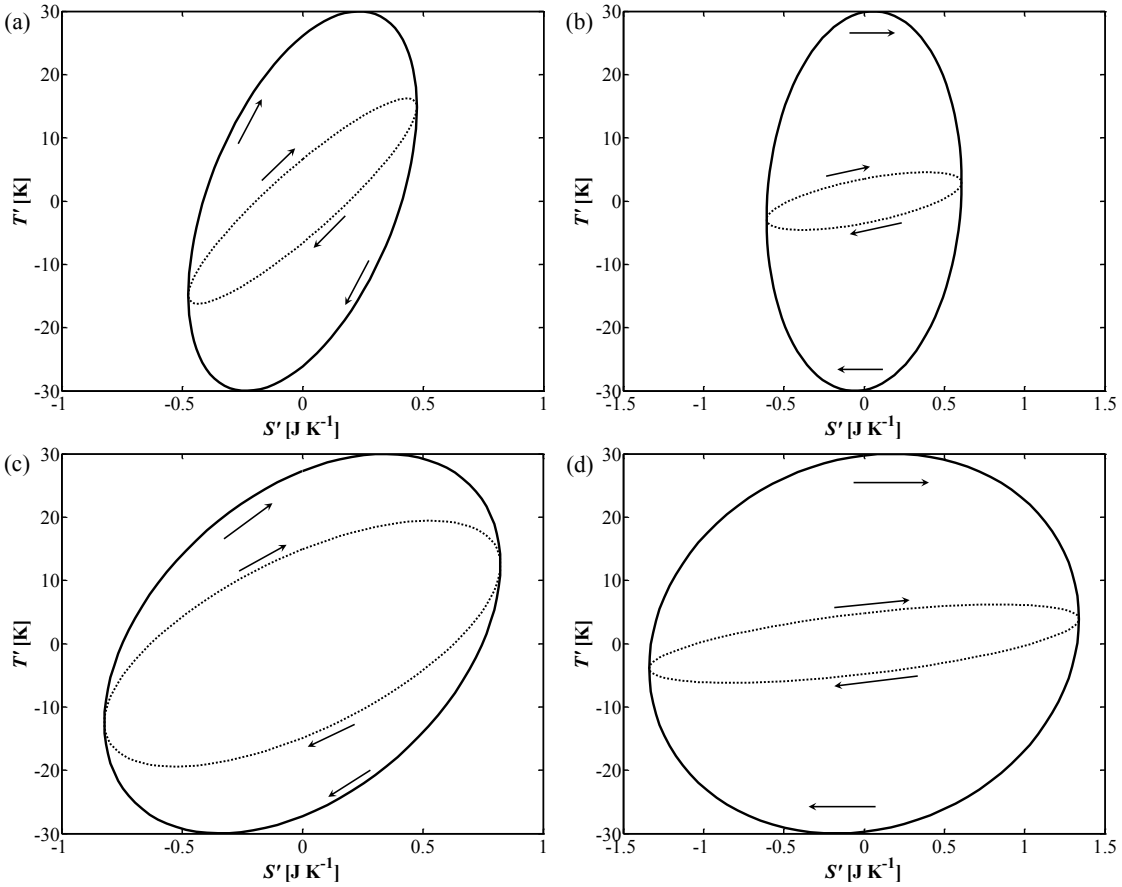


Figure 4.7: Linearised T–S cycle diagrams for the NIFTE predicted by the: (a) LTP model; (b) LTP_{TL} model; (c) nominal DHX model; and, (d) DHX_{TL} model, where the prime $(\cdot)'$ denotes the fluctuation around the time-averaged value of variable $(\cdot)$. The solid black lines represent the net exergy made available to the device, and the dotted black lines represent the net exergy gained by the working fluid. The difference between the two cycles amounts to the exergy (useful work) destruction at the boundary between the working fluid and the heat exchangers, due to irreversible heat transfer.

4.4.3 Thermodynamic cycle diagrams

The temperature-entropy (T–S) diagram for the NIFTE can be used to determine the exergy loss in the device [43]. A number of T–S diagrams from the linearised NIFTE models are shown in Fig. 4.7. Diagrams representing the LTP model with and without the thermal loss impedance Z_{TL} can be seen in Fig. 4.7(a) and (b), respectively, and diagrams from the DHX model with and without the thermal loss impedance Z_{TL} in Fig. 4.7(c) and (d). In these plots, the black solid line represents the temperature of the heat exchangers (T_{hx}) and the black dotted line represents the temperature of the working fluid (T_{ad}). The difference in area between the solid line and the dotted line represents the power loss due to irreversible heat transfer [43]. In the LTP and DHX models in the absence of the thermal loss impedance Z_{TL}, this difference is attributed to the thermal resistance R_{th} in the heat exchangers that governs the heat transfer across the finite temperature difference between the heat exchanger blocks and the working fluid. In the $\mathrm{LTP}_{\mathrm{TL}}$ and $\mathrm{DHX}_{\mathrm{TL}}$ models that contain the thermal loss impedance Z_{TL}, the difference is attributed to R_{th} as well as the thermal loss impedance Z_{TL} that governs the parasitic heat transfer across the finite temperature difference between the surfaces of the vapour region and the working fluid. Therefore the difference in areas between the two cycles gives an indication of the efficiency of the device [43].

It can be seen that the dotted line encompasses a smaller fraction of the area inscribed by the solid black line in the $\mathrm{LTP}_{\mathrm{TL}}$ model (in Fig. 4.7(b)) than is the case with the LTP model with no thermal loss impedance Z_{TL} (in Fig. 4.7(a)). This greater exergy loss in the $\mathrm{LTP}_{\mathrm{TL}}$ correspondents to the lower efficiency predictions discussed in Section 4.4.2 following the inclusion of the thermal loss impedance Z_{TL}. A similar trend is shown in the DHX model diagrams, whereby the $\mathrm{DHX}_{\mathrm{TL}}$ model with the thermal loss impedance Z_{TL} (Fig. 4.7(d)) shows a larger exergy loss than the DHX model wihout the thermal loss (Fig. 4.7(c)). A shift in phase angle and a change in shape of the Lissajous ovals between the models including and excluding the thermal loss impedance Z_{TL} (in both the LTP and DHX) can be attributed to a change in the relative phase and oscillation amplitude of the temperature and entropy. The inclusion of the thermal loss impedance Z_{TL} leads to a lower working fluid temperature amplitude (T'_{ad}). These observations support the conclusion of Markides and Smith [43] that the underlying reason for the improvement in efficiency is an increase in the working fluid temperature amplitude relative to that made available to it by the heat source and sink, as it undergoes the thermodynamic cycle.

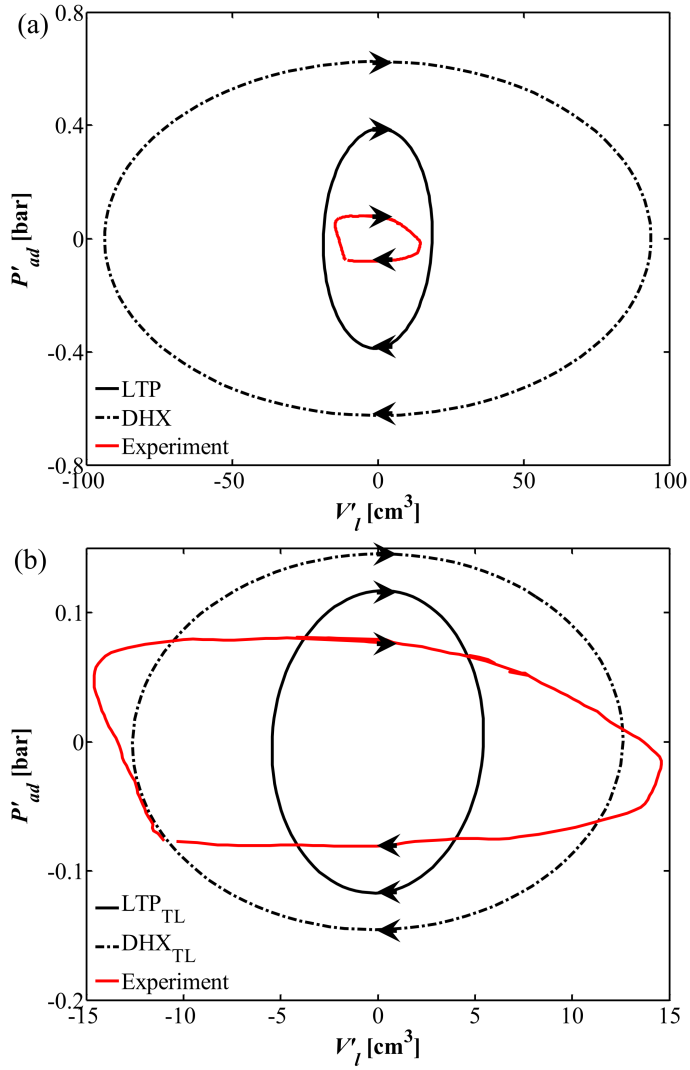


Figure 4.8: Linearised P_{ad}–V_l diagrams for the NIFTE predicted by the LTP and DHX models: (a) excluding; and, (b) including, irreversible unsteady thermal loss effects. Comparison with a corresponding experimental P_{ad}–V_l diagram (red cycle) from a NIFTE prototype, taken from Ref. [2].

Finally, Fig. 4.8 shows a pressure-volume diagram relating the pressure fluctuation in the adiabatic vapour volume P'_{ad} to the volume displacement in the load V'_l for the LTP and DHX models. Figure 4.8(a) shows diagrams generated with the models without the thermal loss impedance Z_{TL} and Fig. 4.8(b) shows diagrams generated with Z_{TL}. The model predictions are compared to direct measurements from Ref. [2]. It is important to note that, since the models are linear, a relation between any two time-varying quan-

tities/properties will take the form of an ellipsoid. As such, these models will not be able to match the experimental data perfectly, but only to first-order. As before, the inclusion of the thermal loss impedance Z_{TL} leads to better agreement with experimental data, with the $\mathrm{DHX_{TL}}$ model showing the best agreement with the experiments. The $\mathrm{LTP_{TL}}$ plot is contained entirely within the experimental envelope, which is representative of the underestimation in the efficiency previously mentioned in Section 4.4.2.

4.5 Summary of chapter findings

Two first-order linear dynamic models for the Non-Inertive-Feedback Thermofluidic Engine (NIFTE) have been developed, each with a different description of the heat transfer between the heat exchangers and the working fluid. These models are known as the linear temperature profile (LTP) and dynamic heat exchanger (DHX). A thermal loss impedance which accounts for exergy losses due to parasitic conjugate heat transfer and phase change in the vapour volume of the NIFTE is developed and incorporated into the LTP and DHX models. Results from a parametric study varying the feedback resistance and load resistance on the LTP and DHX models, including and excluding the thermal loss impedance, are presented and compared to experimental data from an early NIFTE prototype, as reported by Smith [2].

When varying the load resistance, the thermal loss impedance has little effect on the frequencies predicted by the LTP and DHX models including and excluding the thermal loss impedance. The models show that an increase in load resistance leads to a decrease in oscillation frequency, agreeing with the trend observed experimentally. The LTP model predicts frequencies twice those observed experimentally, whereas the DHX model matches the experimental data for oscillation frequency well. The DHX model predicts improved exergetic efficiencies in respose to higher load resistances, whereas the LTP model predicts a maximum efficiency is observed at a load resistance ~ 40 % its nominal value.

It is found further that the LTP and DHX models without the thermal loss impedances predict the trend of experimental data for variations in the feedback resistance well, with an increase in feedback resistance leading to a decrease in oscillation frequency. Experimentally, the NIFTE is shown to operate at frequencies of $0.1 - 0.2$ Hz, which the LTP and DHX models including and excluding the thermal loss impedance are shown to capture without parameter fitting. Moreover, it is found that the DHX model including the thermal loss impedance shows predictions that most closely match the experiments.

In addition, the NIFTE prototype demonstrated efficiencies of up to about 1.5 % when the feedback resistance was varied. The LTP and DHX models neglecting the thermal loss impedance capture the trend of increasing efficiency with increasing feedback resistance. However, the LTP and DHX models that do not account for the thermal losses overestimate the efficiency by 11 and 30 times, respectively. The inclusion of the thermal loss impedance improves the predictions for the exergetic efficiency of both the LTP and DHX models, with little difference between the isothermal and adiabatic boundary conditions applied on the outside of the device. The LTP model with the thermal loss underestimates the measured exergetic efficiency and therefore does not allow for additional losses to be included.

From the results it can be concluded that the DHX model with the addition of the thermal loss impedance is the best model to predict the frequency and exergetic efficiency of the NIFTE. However, the NIFTE prototype is shown to operate with lower efficiencies compared to other devices using the same working fluid and similar working conditions. Therefore further work needs to be done in optimising the device configuration to achieve a higher efficiency and power (pumping) output.

5 Working Fluid Investigation

Several parametric studies have been carried out on the NIFTE, however all these studies investigate the configuration of the device, keeping the conditions and the working fluid the same, that is *n*-pentane at ambient pressure and temperature. There are currently numerous publications on working fluid selection for Organic Rankine Cycles (ORCs) [45–48]. A review on 35 working fluids for ORCs presented by Chen et al. showed that there are no best working fluids for different heat source temperatures. However, the critical temperature of the fluid and the slope of the vapour saturation curve of the fluid are important criteria to take into account when determining the type of cycle and operating temperature of the fluid. A study on the fluid selection for an ORC in a biomass power and heat plant has been carried out by Drescher and Brüggerman. Contrary to other low-grade heat driven ORCs, a higher maximum process temperature of 600 K is defined in this study, where the best working fluids were found to be in the alkylbenzene family [47]. A study carried out by Madhawa Hettiarachchi et al. investigated four working fluids for the use in an ORC with low-temperature (70 °C - 100 °C) geothermal heat sources. Here, ammonia was found to be the optimal working fluid for a cost-effective ORC, though PF5050 was found to have better physical and chemical characteristics.

In this chapter we will investigate the different thermodynamic properties that can effect the exergetic efficiency of the NIFTE. Following from this, 31 working fluids are selected from Ref [45], and the optimal working fluids for the NIFTE at a given configuration and different operation criteria is carried out. The experimentally validated model for the NIFTE, known as the dynamic heat exchanger model including thermal losses (DHX_{TL}) presented in Chapter 4 is used to investigate these working fluids. The method of solving the model is given in Chapter 4 and important efficiency definitions are given in Chapter 2. The work and results presented in this chapter has been published in Ref. [52].

5.1 Thermodynamic properties

The main focus of this study is to investigate the effect of varying the working fluid in the NIFTE $\mathrm{DHX_{TL}}$ model. The parameters for this model are shown in Table 4.1, where it can be seen that model depends on the following thermodynamic parameters of a working fluid; maximum pressure P_{max}, saturation temperature T_{sat}, change in entropy due to vaporisation Δs_{vap}, adiabatic index γ, vapour density ρ_{g}, liquid density ρ_{l} and the gradient along the saturation curve $(\mathrm{d}T/\mathrm{d}P)_{\mathrm{sat}}$ on a pressure-temperature diagram. The gradient along the saturation curve can be given by the Clausius-Clapeyron relation [6], $(\mathrm{d}P/\mathrm{d}T)_{\mathrm{sat}} = \Delta h_{\mathrm{vap}}/T_{\mathrm{sat}}\Delta v_{\mathrm{vap}}$. This relation holds true to systems where there are small deviations in temperature and pressure.

From the list of properties given above (from Table 2.2), a number of dependant variables are identified. To reduce the number of variables investigated, the following expressions are used,

$$\Delta h_{\mathrm{vap}} = T_{\mathrm{sat}}\Delta s_{\mathrm{vap}}, \tag{5.1}$$

$$\rho_{\mathrm{g}} = \left(\Delta v_{\mathrm{vap}} + \frac{1}{\rho_{\mathrm{l}}}\right)^{-1}. \tag{5.2}$$

The expressions in Eqs. (5.1) and (5.2) were compared to data from Ref. [63] for different working fluids. It was found that there was negligible difference between the results obtained from the left hand side of the equation to the right hand side.

5.2 Application scenarios

In Section 5.3, two scenarios are examined with regards to the operation of the NIFTE pumping device:

1. The maximum pressure that the device is working against (P_{max}) is set externally by the application, such that it is associated with a fixed 1 m, 10 m or 30 m head, while the minimum pressure (P_{min}) is associated with the device taking a liquid from ambient (atmospheric) pressure. The temperatures of the heat source and cold sink in this scenario are given by $T_{\mathrm{h}} = T(P_{\mathrm{max}})$ and $T_{\mathrm{c}} = T(P_{\mathrm{min}})$ at saturation conditions, respectively.

2. The temperature of the hot heat exchanger (T_{h}), which coincides with the maximum saturation tem-

perature of the working fluid T_{sat}, is set externally by the application to 60 °C, 80 °C or 100 °C, while the cold heat exchanger temperature (T_c) is set to ambient temperature (20 °C). In this case the pressures are given by $P_{max} = P(T_h)$ and $P_{min} = P(T_c)$ at saturation conditions.

In each one of these scenarios, which depend on the deployment (application) of the device, it is possible to evaluate the Carnot, and therefore the thermal efficiency η_{th} of the NIFTE.

5.3 Results and Discussion

In Sections 5.3.1 and 5.3.2 results are presented from parametric and sensitivity studies concerned with the effects of thermodynamic properties on the working fluid thermal efficiency η_{wf} and the NIFTE exergy efficiency η_{ex}, as defined in Sections 2.5.1 and 2.5.2. A further examination and comparison of the use of a number of working fluids in the NIFTE is performed in Section 5.3.3; specifically in the dynamic heat exchanger model of the NIFTE including thermal losses DHX_{TL} as outlined in Section 2.3.2, with respect to a set of important performance indicators.

5.3.1 Parametric and sensitivity study on η_{wf}

In Section 5.3.3, ammonia and R245ca are identified as promising working fluids for use in the NIFTE, at least for the specific practical applications of this technology investigated in this study. In addition, water is a common working fluid and *n*-pentane is the working fluid that was selected for use in a prototype of the NIFTE pump mentioned previously [2]. Therefore, in this section we investigate the ideal working fluid thermal efficiencies η_{wf} and corresponding working fluid exergy efficiencies $\eta_{wf,ex} = \eta_{wf}/\eta_{Carnot}$ for *n*-pentane, water, ammonia and R245ca. The two efficiencies are obtained by evaluating Eq. (2.39) as a function of the saturation temperature during heat addition T_{sat}, which fixes the change in volume due to vaporisation $\Delta v_{vap}(T_{sat})$, but also the saturation pressure at this temperature P_{max} and hence the change in entropy due to vaporisation $\Delta s_{vap}(P_{max})$. Recall, from Section 2.5.1, that in obtaining the expression in Eq. (2.39) for the working fluid efficiency η_{wf} no information regarding the NIFTE cycle or the associated device was provided, thus, this efficiency is not directly related to the NIFTE. Instead, this efficiency measure applies to a generic positive-displacement, two-phase unsteady heat engine, and is the maximum thermal efficiency obtained by a hypothetical ideal heat engine cycle in which the total useful work done is

by positive-displacement pumping into a load due to phase change, ignoring any parasitic power dissipated in valves or lost due to heat transfer across finite temperature differences during heat transfer. Similarly, the same can said for the working fluid exergy efficiency measure $\eta_{\mathrm{wf,ex}}$.

The results are shown in Fig. 5.1, where the working fluid thermal efficiency η_{wf} for each fluid is plotted as a function of the heat addition saturation temperature T_{sat} (Fig. 5.1(a)) and the corresponding dimensionless temperature ratio that is defined as the ratio of the saturation temperature to the critical temperature $T_{\mathrm{r}} = T_{\mathrm{sat}}/T_{\mathrm{crit}}$ (Fig. 5.1(b)). From these plots it is possible to determine which fluid has the highest potential to convert heat to work for a given heat source temperature, and when expansion is allowed into the ambient environment and specifically down to atmospheric pressure. Maximum ideal thermal efficiency values of up to about 15% for ammonia, and about 13-14% for the rest of the fluids can be observed at the highest temperatures, as expected. In fact, for all fluids shown, η_{wf} increases monotonically at progressively higher T_{sat}, except near the critical point (when T_{r} approaches unity) where a maximum in η_{wf} is observed[1]. The highest thermal efficiency is attained by ammonia near its critical temperature of 405.40 K (132.25 °C). Above this temperature R245ca takes over as the fluid with the greatest thermal efficiency, near its own critical temperature of 447.57 K (174.42 °C), and beyond which water is the only working fluid that can undergo a subcritical power cycle. One notes also that at the zero efficiency point the four curves do not collapse to the same temperature, whether dimensional or normalised. This would be expected from the different saturation temperatures at atmospheric pressure (which is in fact the heat rejection temperature) for the different fluids. It is interesting to observe, however, that the two organic fluids and the two hydrogen-bond fluids appear as two separate bands in the dimensionless temperature plot.

It was stated above, and previously in Section 2.5.1, that the ideal cycle that gives rise to η_{wf} requires that following isothermal phase-change expansion and subsequent expansion into its surrounding environment which is at atmospheric pressure (considered the minimum pressure, $P_{\mathrm{min}} = P_{\mathrm{atm}}$), a cold sink exists at some suitable temperature T_{min}, that is not necessarily atmospheric, into which heat can be rejected to close the cycle. This means that each fluid will expand down to and then condense at the same low pressure $P_{\mathrm{min}} = P_{\mathrm{atm}}$ but *different* cold temperature $T_{\mathrm{min}} = T(P_{\mathrm{min}})$. One way to compare the performance of the working fluids given the different temperature difference across which they operate in the ideal cycle, is to

[1]Note that, as $T_{\mathrm{r}} \to 1$: $\Delta h_{\mathrm{vap}} \to 0$, $\Delta s_{\mathrm{vap}} \to 0$ and $\Delta v_{\mathrm{vap}} \to 0$, so the practical usefulness of such a cycle would be questionable.

define a working fluid exergy efficiency $\eta_{\text{wf,ex}}$, which is the working thermal fluid efficiency η_{wf} divided by the Carnot efficiency corresponding to the hot temperature T_{sat} that is the same for all fluids and the cold temperature $T(P_{\text{min}})$ which depends on the fluid, or,

$$\eta_{\text{wf,ex}} = \frac{\eta_{\text{wf}}}{\eta_{\text{Carnot}}} = \frac{[P_{\text{max}}(T_{\text{sat}}) - P_{\text{atm}}]\,\Delta v_{\text{vap}}(T_{\text{sat}}, P_{\text{max}})}{\Delta s_{\text{vap}}(T_{\text{sat}}, P_{\text{max}})\,[T_{\text{sat}}(P_{\text{max}}) - T_{\text{min}}(P_{\text{atm}})]}\,. \tag{5.3}$$

Referring to the thermodynamic cycle in Fig. 2.6, $P_{\text{max}}(T_{\text{sat}})$ or $T_{\text{sat}}(P_{\text{max}})$ (corresponding to Scenarios 1 or 2 in Section 5.2, respectively) are the maximum saturation pressure and temperature during the heat addition, vaporisation and expansion process from States 2 to 3, $v_{\text{vap}}(T_{\text{sat}}, P_{\text{max}})$ and $\Delta s_{\text{vap}}(T_{\text{sat}}, P_{\text{max}})$ are the volume and specific entropy changes during the same process, and P_{atm} and $T_{\text{min}}(P_{\text{atm}})$ are the minimum saturation pressure (taken as atmospheric pressure) and temperature during the heat rejection and condensation process from States 4 to 1.

The working fluid exergy efficiency $\eta_{\text{wf,ex}}$ is plotted as a function of the temperature ratio T_{r} in Fig. 5.1(c). From here it can be seen that $\eta_{\text{wf,ex}}$ decreases monotonically with increasing temperature, with the two organic fluids exhibiting the highest efficiencies for the same temperature ratio T_{r}. For all fluids, when the lowest allowable hot/heat addition temperature T_{sat} approaches the minimum/cold temperature (which is the saturation temperature at the lowest pressure that is taken here as atmospheric, i.e. when $T_{\text{sat}} \rightarrow T_{\text{min}}(P_{\text{atm}})$), the exergy efficiency $\eta_{\text{wf,ex}}$ approaches 100%. This point occurs at different values of $T_{\text{r}} = T_{\text{sat}}/T_{\text{crit}}$ independent of the fluid, as expected.

At this stage, having examined the ultimate efficiencies of each working fluid in an ideal two-phase/vapour cycle as a function of relevant external conditions, it becomes interesting and important to identify which specific thermodynamic properties of the working fluid play a dominant role in determining the working fluid thermal efficiency and in controlling the trends of this efficiency as a function of the conditions. In order to determine the most important properties, a parametric investigation is carried out on η_{wf}, as this is defined in Eq. (2.39), whereby each thermodynamic property in Eq. (2.39) is varied independently while all other properties are set to a 'nominal' value defined by a nominal value of the maximum saturation temperature $T_{\text{sat,nom}}$. The *independent* thermodynamic properties used are the: maximum pressure P_{max}, maximum saturation temperature T_{sat}, change in volume due to vaporisation Δv_{vap}, and change in entropy due to vaporisation Δs_{vap}. Recall that the minimum pressure P_{min} is taken as atmospheric pressure, P_{atm}.

The results from such a parametric study, carried out on the working fluid thermal efficiency η_{wf} and using n-pentane as the reference working fluid, are shown in Fig. 5.2.

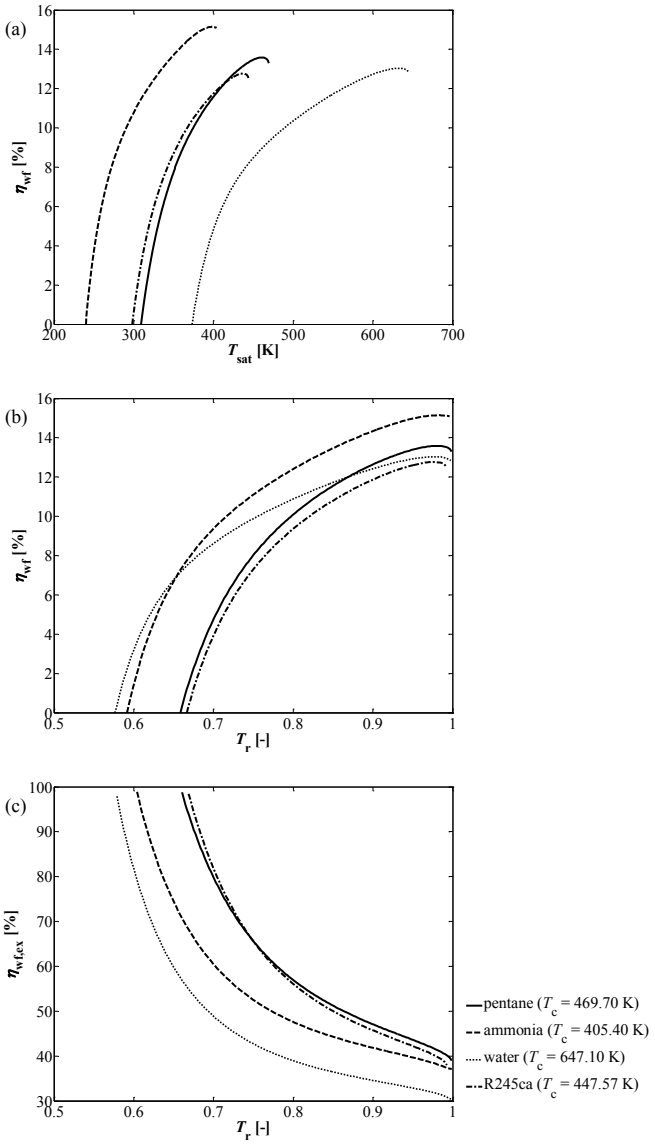


Figure 5.1: The working fluid thermal efficiency η_{wf} for n-pentane, ammonia, water and R245ca against: (a) the heat addition saturation temperature T_{sat}, and (b) the temperature ratio $T_{\mathrm{r}} = T_{\mathrm{sat}}/T_{\mathrm{crit}}$. (c) The working fluid exergy efficiency $\eta_{\mathrm{wf,ex}} = \eta_{\mathrm{wf}}/\eta_{\mathrm{Carnot}}$ against the temperature ratio T_{r}.

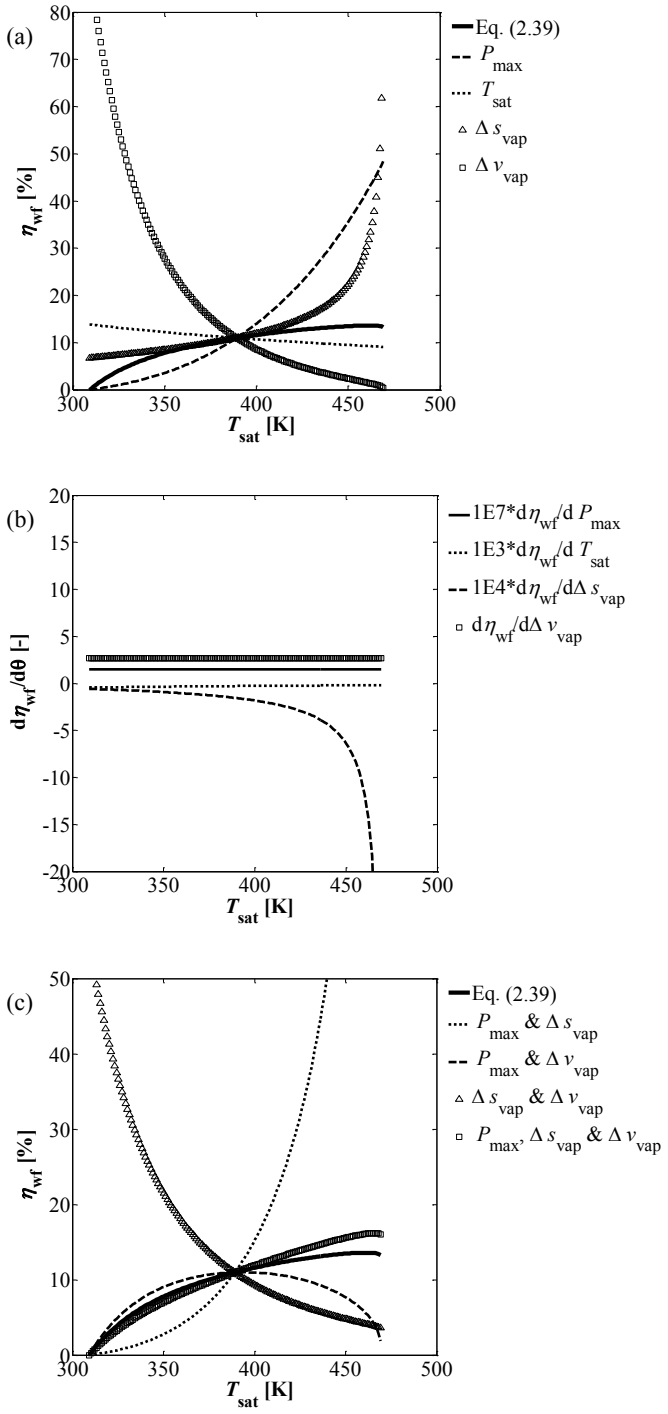


Figure 5.2: The working fluid thermal efficiency η_{wf} for *n*-pentane on varying the maximum pressure P_{max}, saturation temperature T_{sat}, change in entropy due to vaporisation Δs_{vap}, and change in volume due to vaporisation Δv_{vap}, where: (a) each thermodynamic property is varied individually, (b) the sensitivity of η_{wf} to each individual thermodynamic property θ is considered, and (c) combinations of the thermodynamic properties are varied.

The effect of varying each thermodynamic property on the working fluid thermal efficiency η_{wf}, whilst all remaining properties are set to their nominal values defined by a nominal saturation temperature $T_{sat,nom}$ = 393.15 K (120 °C), is shown in Fig. 5.2(a). The range of values spanned by the perturbed thermodynamic property, which are then inserted into the expression in Eq. (2.39) for η_{wf}, are obtained by spanning a given range of saturation temperatures T_{sat} from T_{sat} = 313.15 K to 473.15 K (40 °C to 200 °C), as indicated on the horizontal axis, and generating the corresponding thermodynamic property at that saturation temperature. From Fig. 5.2(a) it can be seen that varying the change in volume due to vaporisation $\Delta v_{vap}(T_{sat})$ over the chosen range of conditions (from T_{sat} = 313.15 K – 473.15 K, or 40 °C – 200 °C) leads to the greatest deviation of η_{wf} from the nominal value of the working fluid thermal efficiency $\eta_{wf,nom}$ = 11%, defined as the working fluid thermal efficiency evaluated at $T_{sat,nom}$. Varying the maximum pressure $P_{max}(T_{sat})$ leads to the second largest deviation from the nominal working fluid thermal efficiency $\eta_{wf,nom}$ over the majority of the temperature range investigated. Furthermore, it appears that as the saturation temperature approaches the critical temperature of *n*-pentane (469.70 K, or 196.55 °C), small changes in Δs_{vap} give rise to very significant improvements in η_{wf} relative to $\eta_{wf,nom}$. This may be expected, given that Δs_{vap} tends to zero as the temperature approaches the critical temperature of a fluid, which would cause the heat input into the ideal cycle in Fig. 2.6 to also tend to zero. The least significant thermodynamic property with regards to its effect on η_{wf} is the saturation temperature T_{sat}; varying T_{sat} independently with all other properties set to their nominal values, leads to very small deviations from $\eta_{wf,nom}$ of the order of a few % points.

The *local change* in the working fluid thermal efficiency, $\partial\eta_{wf}/\partial\theta$, with respect to each thermodynamic property of interest, θ, namely: P_{max}, T_{sat}, Δv_{vap} and Δs_{vap}, is shown in Fig. 5.2(b). This plot can be considered a sensitivity analysis on η_{wf}. One observes that η_{wf} is most sensitive to Δv_{vap} and not sensitive to T_{sat} over the investigated range of T_{sat}, which is consistent with previous findings from Fig. 5.2(a). Contrary to the conclusion drawn from Fig. 5.2(a), that changes to the maximum pressure $P_{max}(T_{sat})$ corresponding to T_{sat} = 313.15 K – 473.15 K (40 °C – 200 °C) resulted in the second most significant variation in η_{wf}, Fig. 5.2(b) reveals that in terms of local sensitivity (rate of change), η_{wf} is least sensitive to P_{max}, and is more sensitive to Δs_{vap}. This is because, within the range of investigated T_{sat}, $P_{max}(T_{sat})$ spans a larger range of values compared to $\Delta s_{vap}(T_{sat})$ and T_{sat}.

Going a step further, the simultaneous variation of a combination of (two and three) thermodynamic properties from: T_{sat}, P_{max}, Δs_{vap} and Δv_{vap}, and the effect of these variations on η_{wf} are investigated in

Fig. 5.2(c). It can be deduced that, although η_{wf} is most sensitive to changes in Δs_{vap} and Δv_{vap}, variations in Δv_{vap} simultaneously with P_{max} whilst all remaining parameters are set to their nominal values (dashed line), has the most representative effect on η_{wf}. On adding Δs_{vap} and varying the three variables simultaneously (square symbols), the working fluid thermal efficiency predictions are both in the correct order of magnitude and capture closely the full trend of η_{wf} from Eq. (2.39) with the correct values of all thermodynamic parameters, which gives the solid black line in Fig. 5.2(c). It is concluded that, Δv_{vap}, P_{max} and Δs_{vap} are the most important variables in determining the value of and variations in η_{wf}, and of these three Δv_{vap} and P_{max} together can most closely capture this behaviour. A high η_{wf} is associated with a high Δv_{vap}, a high value of P_{max} and a low value of Δs_{vap}, with the former two maximising the specific work output and the latter minimising the specific heat input in the cycle.

5.3.2 Parametric study on η_{ex}

The exergy efficiency of the NIFTE, η_{ex}, as predicted by the dynamic heat exchanger model including thermal loss DHX_{TL} is defined in Eq. (2.40). It can be seen that this expression is a function of both a selection of thermodynamic properties of the working fluid, but also of configuration and operation parameters of the engine (geometry, heat transfer, etc.). The DHX_{TL} model has been validated against experimental data from a NIFTE prototype with *n*-pentane as the working fluid taken from Ref. [2]. In this section we set the geometric and operational configuration of the NIFTE to that given in Chapter 4, select *n*-pentane as the working fluid, and carry out a parametric study on η_{ex}, specifically investigating the effects of the following *thermodynamic properties*: change in volume due to vaporisation Δv_{vap}, maximum pressure P_{max}, change in entropy due to vaporisation Δs_{vap}, liquid density ρ_{lq}, adiabatic index γ and saturation temperature T_{sat}, as they appear in Eq. (2.40). To carry out this study, each one of these thermodynamic properties is perturbed independently over a range corresponding to their values for a given saturation temperature range, T_{sat} = 293.15 K – 393.15 K (20 °C – 120 °C). All other properties are set to a constant 'nominal' value, defined as their value at a given nominal saturation temperature. Three nominal points are investigated: $T_{sat,nom}$ = 293.15 K (20 °C), $T_{sat,nom}$ = 333.15 K (60 °C) and $T_{sat,nom}$ = 393.15 K (120 °C). The effect of varying each property on the NIFTE DHX_{TL} exergy efficiency η_{ex} at the three nominal points is shown in Fig. 5.3, with results at the three selected nominal saturation temperatures shown in Fig. 5.3(a), (b) and (c). The corresponding nominal values of η_{ex} are: 0.7%, 3.5% and 3.2%, respectively.

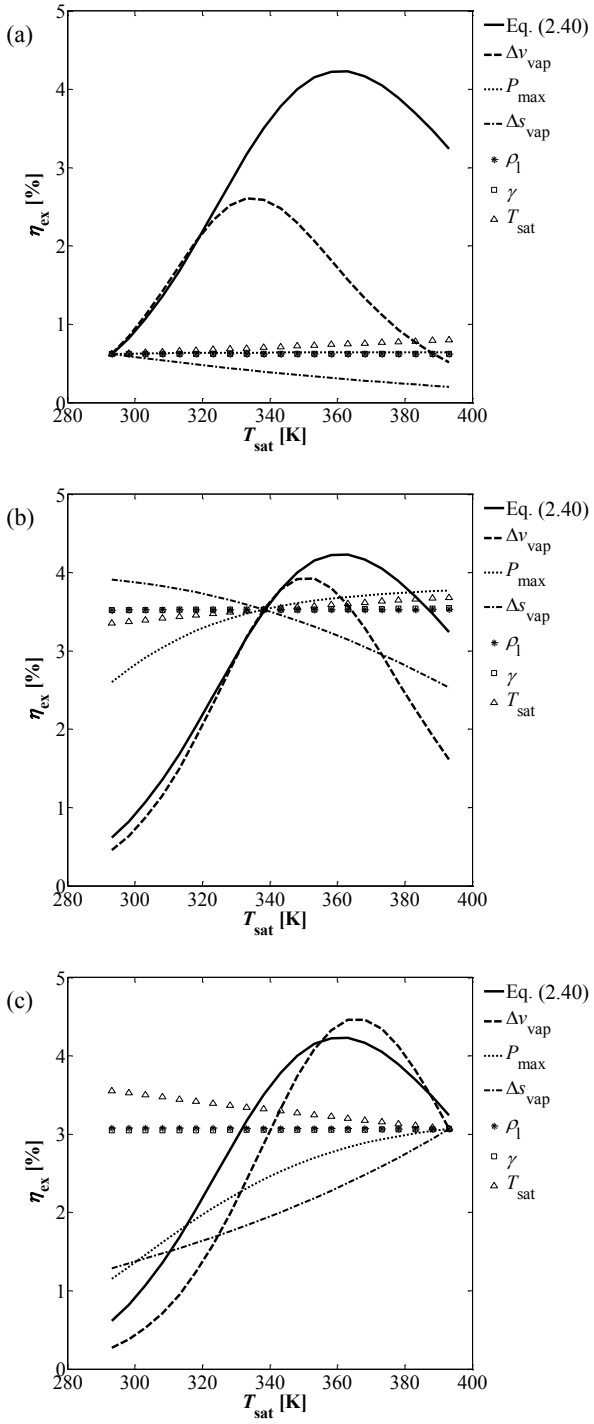


Figure 5.3: The exergy efficiency η_{ex} predicted by the DHX_{TL} model with *n*-pentane as the working fluid on varying the change in volume due to vaporisation Δv_{vap}, maximum pressure P_{max}, change in entropy due to vaporisation Δs_{vap}, liquid phase density ρ_{lq}, adiabatic index γ, and saturation temperature T_{sat}. The nominal values for the saturation properties are set to: (a) $T_{sat,nom} = 293.15\,K$, (b) $T_{sat,nom} = 333.15\,K$, and (c) $T_{sat,nom} = 393.15\,K$.

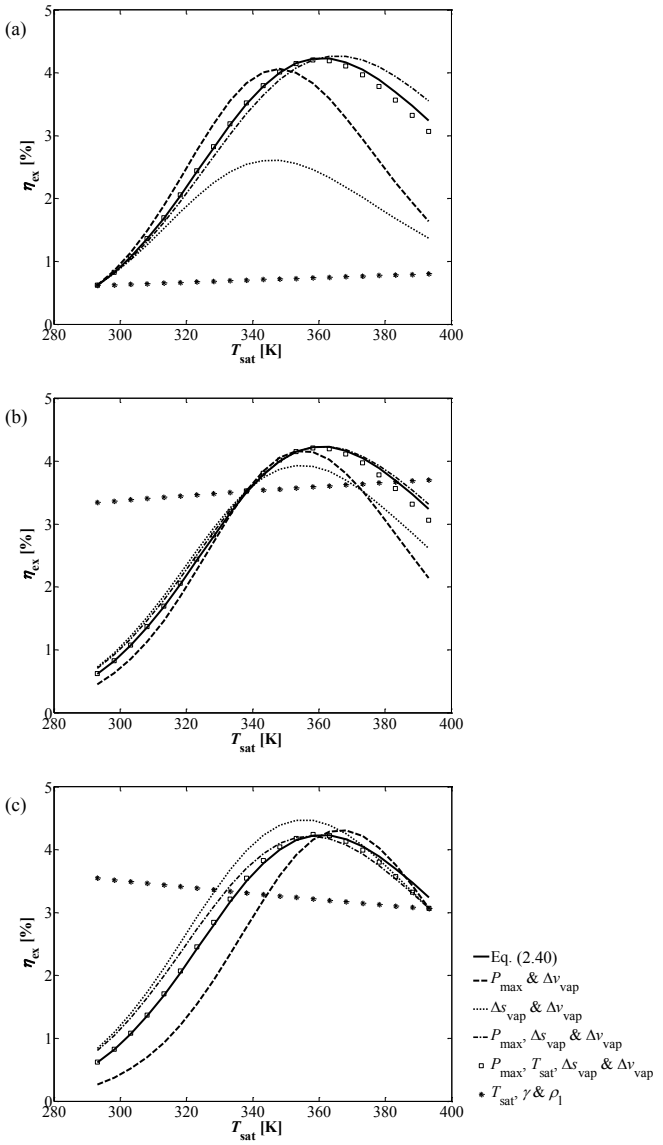


Figure 5.4: The exergy efficiency η_{ex} predicted by the DHX_{TL} model with *n*-pentane as the working fluid on varying combinations of the thermodynamic properties from the following list: change in volume due to vaporisation Δv_{vap}, saturation pressure P_{sat}, change in entropy due to vaporisation Δs_{vap}, liquid phase density ρ_{lq}, adiabatic index γ, and saturation temperature T_{sat}. The nominal values for the saturation properties are set to: (a) $T_{sat,nom} = 293.15\,K$, (b) $T_{sat,nom} = 333.15\,K$, and (c) $T_{sat,nom} = 393.15\,K$.

In all three plots (i.e. for all three nominal values of T_{sat} and η_{ex}), the thermodynamic property whose independent variations over the investigated range of T_{sat} lead to the greatest deviations in η_{ex} from its

nominal value is the change in volume due to vaporisation Δv_{vap}. This result is in agreement with the findings from the parametric study carried out on the working fluid thermal efficiency η_{wf} in Section 5.3.1. Changes in Δv_{vap} can account qualitatively for the general trend of η_{ex}, whereby a maximum is seen at an approximate saturation temperature of $T_{sat} \approx 360\,\text{K}$ ($\approx 90\,^{\circ}\text{C}$). This is a more complex relationship than that exhibited by η_{wf} as a function of variations to the same variable (Δv_{vap}) in Fig. 5.2(a), where the efficiency dropped monotonically at increasingly higher T_{sat} due to progressively reduced Δv_{vap}, and thus reduced displacement work done. The appearance of the maximum in η_{ex} arises here due to the inclusion of the thermal loss parameter in the DHX_{TL} model; the enhanced Δv_{vap} due to phase change (evaporation) of the working fluid at lower T_{sat} leads to higher work outputs, but this also competes with the increased thermal losses due to parasitic phase change in the *nominally* adiabatic vapour chamber ('ad' in Fig. 1.7). Eventually, at the lowest T_{sat}, the losses overcome the gains in useful work due to the larger Δv_{vap}.

Varying the maximum saturation pressure P_{max} and the change in entropy due to vaporisation Δs_{vap}, independently of each other, leads to the second largest variations in the exergy exergy efficiency of the NIFTE DHX_{TL} model. This is also in general agreement with the parametric study performed on η_{wf} shown in Section 5.3.1. The final three properties, ρ_{lq}, γ and T_{sat}, have a minimal effect on η_{ex}. Varying each one of these properties across the defined range leads to small deviations from the nominal exergy efficiency values.

The effect on η_{ex} of varying a combination of properties simultaneously, across the range of values defined by T_{sat} for the three nominal cases, is shown in Fig. 5.4. In all cases, varying Δv_{vap} and P_{max} simultaneously, whilst all other properties are set to their (constant) nominal values, gives a good prediction of η_{ex} from the full Eq. 2.40, both in magnitude and overall trend. Varying Δs_{vap} in addition to Δv_{vap} and P_{max} gives an even better prediction of η_{ex}, in excellent agreement with the parametric study in Section 5.3.1. As before, varying ρ_{lq}, γ and T_{sat} simultaneously does not lead to significant changes in η_{ex} relative to nominal. This suggests that, when selecting a working fluid for the NIFTE, these properties can be neglected, while prioritising a large Δv_{vap} and P_{max}, and small Δs_{vap}.

5.3.3 Working fluid comparison

In this final section, results are presented from a study in which the NIFTE DHX_{TL} model is run for 31 different working fluids, stated in Table 5.1, under the two scenarios given in Section 5.2; in the first

the maximum pressure the engine is working against is set by a hypothetical external application and the minimum pressure is set to ambient conditions, and in the second the saturation temperatures in the hot and cold heat exchangers are set by hypothetical external conditions. The working fluids that were chosen to be investigated were obtained from Ref. [45], where a review of working fluids for the conversion of low-grade heat by ORCs is investigated.

Table 5.1: List of working fluids investigated, ordered from top to bottom by decreasing exergy efficiency η_{ex} at a HHX and maximum saturation temperature T_{sat} of 333.15 K (or, 60 °C).

Working Fluid	Type of Fluid
R245ca	isentropic
R123	isentropic
FC4112	dry
R141b	isentropic
R245fa	isentropic
N-pentane	isentropic
R21	wet
N-butane	dry
R236ea	isentropic
R3110	isentropic
Isobutane	dry
RC318	dry
R142b	isentropic
R124	isentropic
R227ea	isentropic
Hexane	dry
R152a	wet
R134a	isentropic
R218	isentropic
Propane	dry
Benzene	isentropic
Propene	wet
R22	wet
R143a	wet
R125	wet
Ammonia	wet
Heptane	dry
R32	wet
Water	wet
Toluene	isentropic
Octane	dry

Scenario 1: Imposed external pressures

In this scenario the maximum and minimum temperatures in the cycle, which are also the temperatures of the HHX and CHX inside the NIFTE device, are set to be equal to the saturation temperatures at the maximum pressure imposed on the device in the load P_{max} and ambient from where the pumped medium is taken, for each particular working fluid. The effect of changing the maximum pressure that the NIFTE has to work against (pump into), P_{max}, is shown in Figs. 5.5 – 5.7. Specifically, the exergy efficiency η_{ex}, working fluid thermal efficiency η_{wf}, and thermal efficiency η_{th} for a NIFTE pumping device working against a 1 m, 10 m or 30 m head is shown in Figs. 5.5(a), 5.6(a) and 5.7(a), respectively. The working fluids are shown (in all figures) in descending order of η_{ex} for a device working against a 1 m head, from left to right. Furthermore, the corresponding oscillation frequencies f_0 of the NIFTE are shown in Figs. 5.5(b), 5.6(b) and 5.7(b), while a normalised measure of hydraulic/pumping power output (per unit heat input to the device) is shown in Figs. 5.5(c), 5.6(c) and 5.7(c).

Referring to Figs. 5.5(a), 5.6(a) and 5.7(a), for a given working fluid, increasing the maximum pressure/head leads generally to an overall increase in the exergy and thermal efficiencies predicted by the DHX_{TL} NIFTE model and an overall decrease in the working fluid thermal efficiency η_{wf}. The working fluid efficiency η_{wf} measure drops from about $\sim 95\%$ at 1 m head, to $\sim 75\%$ at 10 m, to $\sim 60\%$ at 30 m, while the predicted thermal efficiency of the NIFTE devise η_{th} increases from about $\sim 0.05\%$, to $\sim 0.4\%$, to $\sim 0.8\%$ for a particular geometrical and operational configuration of the device. The corresponding exergy efficiency η_{ex} increases from 3 – 4% at low heads (1 m), to 5 – 6% at intermediate and high heads (10 m – 30 m).

For a device working against a 1 m head, shown in Fig. 5.5(a), it is seen that the higher η_{ex} are dominated by wet and isentropic fluids. In agreement with the results from Ref. [48], ammonia is found to be the optimal working fluid for the lowest pressure case, at least in terms of η_{ex}. Larger-chain components tend to have a lower η_{ex}, which is a trend also seen in a system working against a 10 m head in Fig. 5.6(a). As the maximum pressure of the system increases, the larger-chain components tend to preform better, as seen in Fig. 5.7(a). The working fluid that maintains the highest thermal efficiency η_{th} over the range of investigated heads is propene. Also promising are: R22 and R134a at low heads, R143a and R32 at intermediate heads, and *n*-butane/isobutane at high heads; in fact, *n*-butane and R142b maintain a reasonable performance over

a wider range of heads from 1 m to 30 m.

The oscillation frequency f_0 predicted for a NIFTE device working against a 1 m head is shown in Fig. 5.5(b). This system variable is important, as it strongly affects the pumping operation and hence flow-rate capability of the device. This plot indicates that the choice of working fluid plays only a minor role in determining its operational frequency. This finding is confirmed at 10 m and 30 m heads, which are shown in Figs. 5.6(b) and 5.7(b), respectively, and is also in line with the results presented in Chapters 3 and 4 where changes in parameters lead to small changes in the predicted f_0. A comparison of the results for f_0 from all three maximum head settings in Figs. 5.5(b) – 5.7(b), reveals that increasing the maximum head leads to an overall increase in the operational frequency of the NIFTE. Specifically, the frequency increases from $f_0 \approx 0.075$ Hz at a head of 1 m to $f_0 \approx 0.1$ Hz at 30 m.

In addition, it is important to consider the normalised power output per unit heat input $f_0\eta_{ex}$ for a NIFTE device. This normalised work measure is shown in Figs. 5.5(c), 5.6(c) and 5.7(c) for a device working against a 1 m, 10 m and 30 m head, respectively. Increasing the head leads to a strong overall increase in $f_0\eta_{ex}$, as expected, since the system is working against a higher pressure, and more work is done in the load at high pressures. It is noted that working fluids that exhibit the highest normalised work $f_0\eta_{ex}$ (Figs. 5.5(c) – 5.7(c)) are strongly correlated to those that exhibit the highest exergy efficiency η_{ex}; this is a consequence of the very similar operational frequencies f_0 (Figs. 5.5(b) – 5.7(b)) predicted for the NIFTE for the various working fluids.

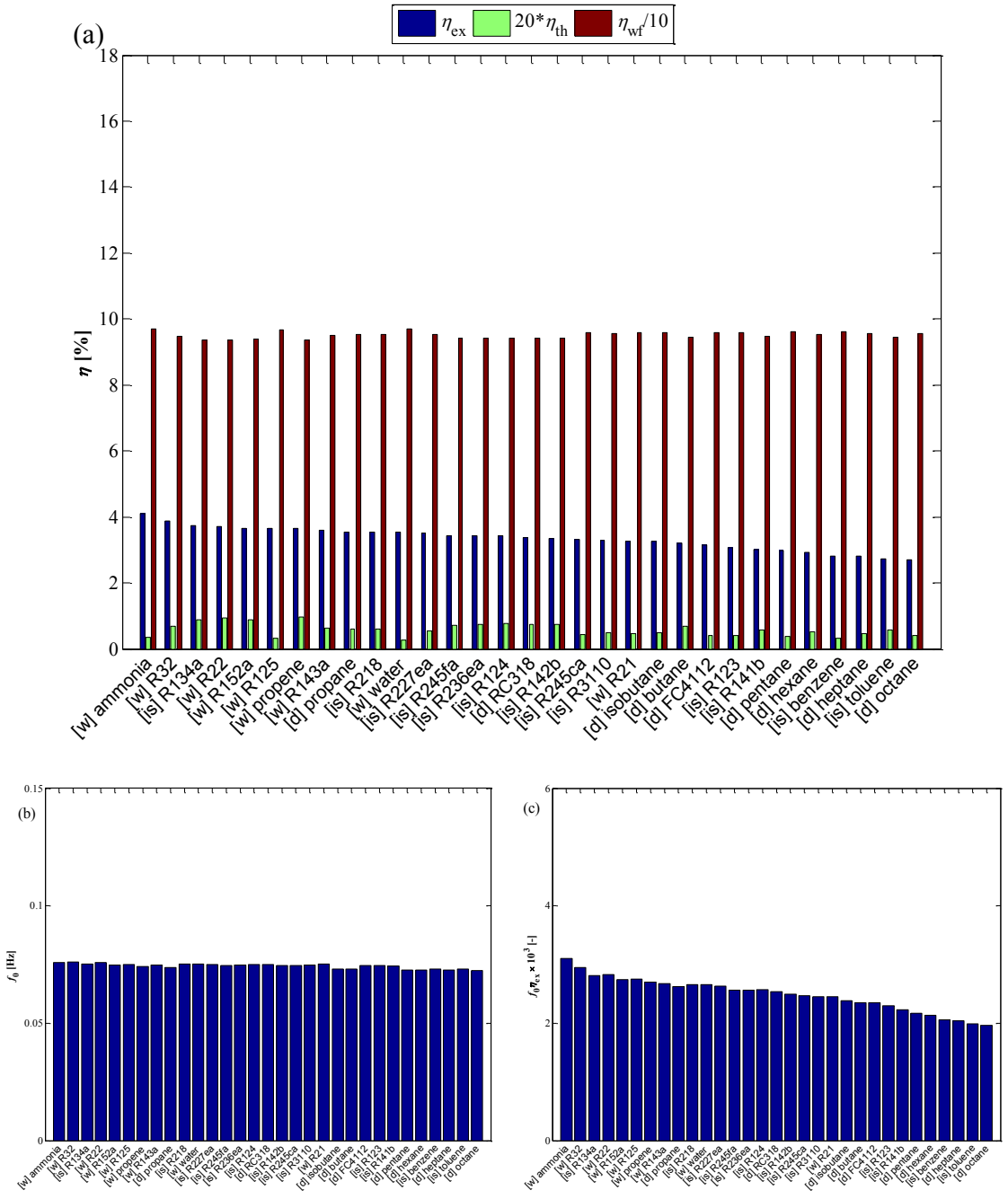


Figure 5.5: (a) Exergy efficiency η_{ex}, thermal efficiency η_{th} and working fluid efficiency η_{wf}, (b) oscillation frequency f_0, and (c) normalised power output per unit heat input $f_0\eta_{ex}$ for different working fluids and a system working against a 1 m head.

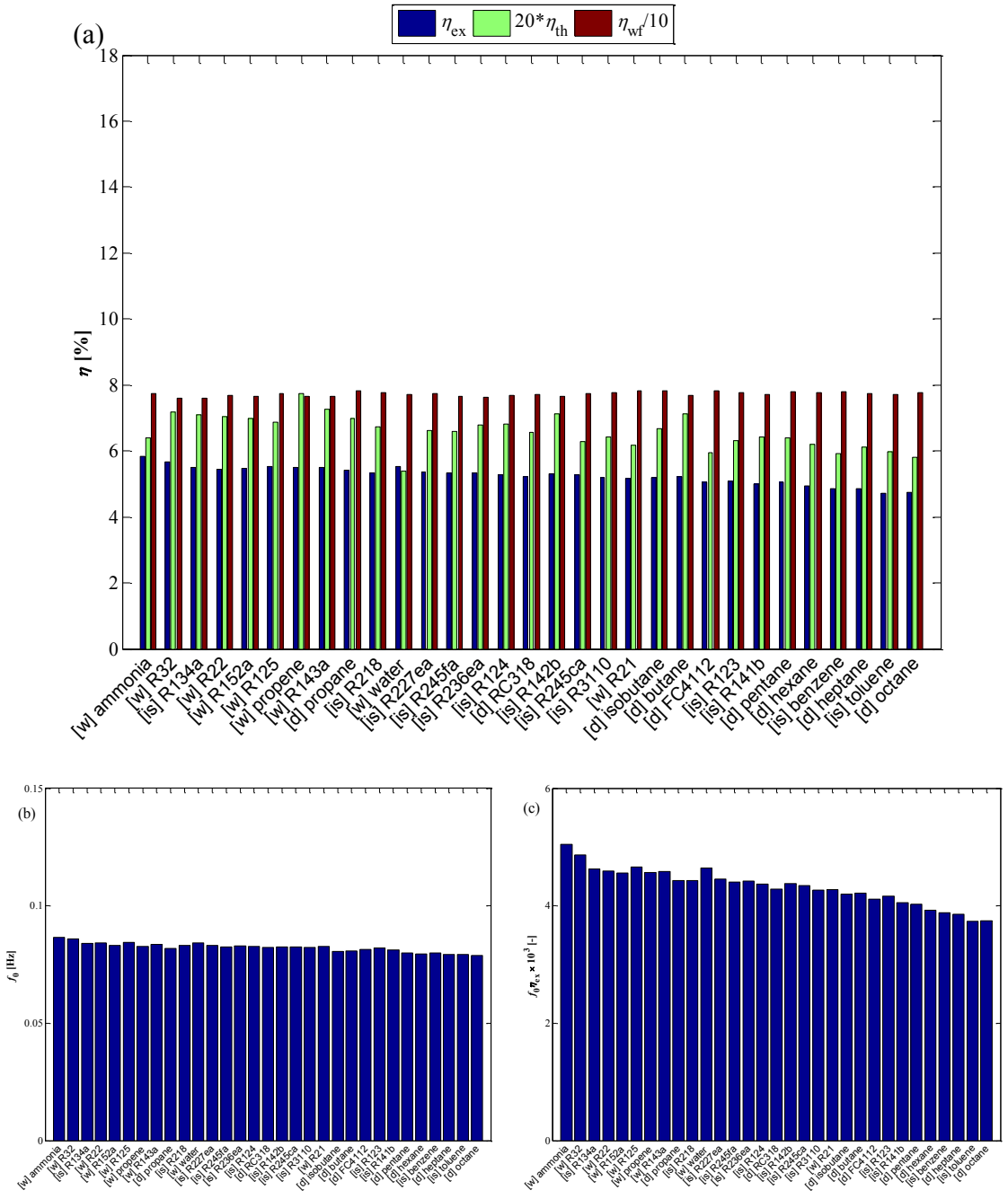


Figure 5.6: (a) Exergy efficiency η_{ex}, thermal efficiency η_{th} and working fluid efficiency η_{wf}, (b) oscillation frequency f_0, and (c) normalised power output per unit heat input $f_0\eta_{ex}$ for different working fluids and a system working against a 10 m head.

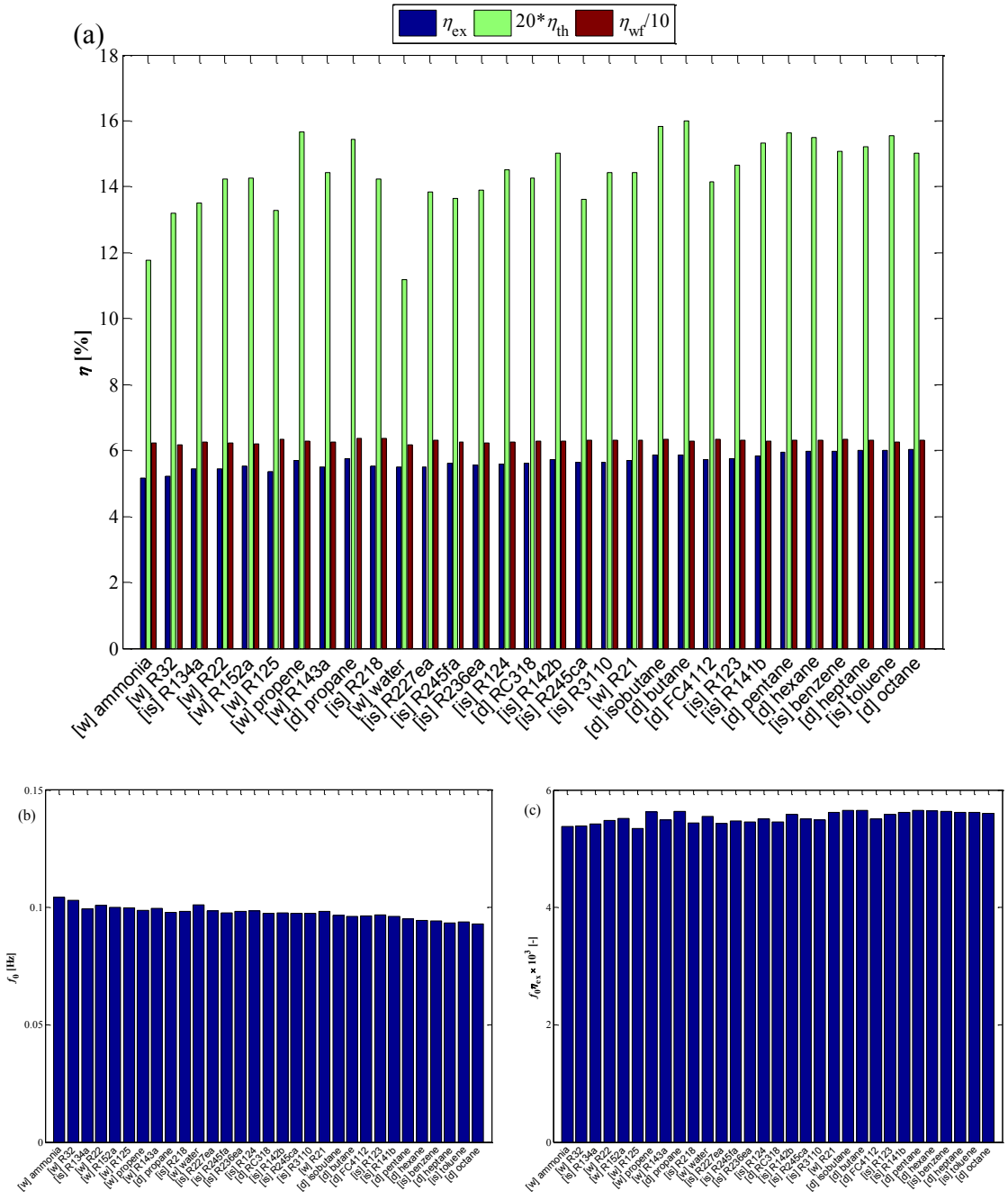


Figure 5.7: (a) Exergy efficiency η_{ex}, thermal efficiency η_{th} and working fluid efficiency η_{wf}, (b) oscillation frequency f_0, and (c) normalised power output per unit heat input $f_0\eta_{ex}$ for different working fluids and a system working against a 30 m head.

Scenario 2: Imposed external temperatures

The effect on the various efficiency measures of setting the hot heat exchanger (HHX) temperature, and thus also the maximum saturation temperature in the cycle during heat addition and evaporation T_{sat}, to 333.15 K, 353.15 K or 373.15 K (60 °C, 80 °C or 100 °C), while keeping the cold heat exchanger (CHX) and also heat rejection/condensation temperature fixed at 293.15 K (20 °C), is shown in Figs. 5.8 – 5.10. In this case, the maximum positive-displacement pressure and minimum suction pressures in the load are matched to the working fluid saturation pressures at the HHX and CHX temperatures in the device, respectively. Note that the HHX temperature exceeds the critical temperature for some working fluids. In these cases, no results for these fluids are presented.

In Fig. 5.8(a) the exergy (η_{ex}), working fluid (η_{wf}) and thermal (η_{th}) efficiencies for a NIFTE working with a HHX temperature of T_{sat} = 333.15 K (60 °C) are shown. The working fluids are shown in descending order of η_{ex} from left to right. A larger range of η_{ex} values are spanned for the investigated fluids compared to the scenario where the maximum cycle pressure is set (see Figs. 5.5 – 5.7). In this scenario of setting the HHX and CHX temperatures and allowing the pressures to vary for the various working fluids, the higher efficiencies are dominated by isentropic and dry working fluids, and there does not appear to be a clear correlation between component chain length and η_{ex} for a given temperature. The highest efficiency is displayed by R245ca (and less so, R123 and FC4112) at low temperatures (333.15 K, or 60 °C; Fig. 5.8(a)), *n*-pentane at intermediate and *n*-pentane/hexane higher ones (353.15 K and 373.15 K, or 80 °C and 100 °C; Fig. 5.9(a) and Fig. 5.10(a)). Interestingly, when the HHX temperature is increased, neither η_{ex} nor η_{th} show a general improvement; in many cases in fact, the efficiencies drop. A possible explanation for this finding is given below in Section 5.3.3.

The operational frequency f_0 of the NIFTE predicted for HHX temperatures of 333.15 K, 353.15 K and 373.15 K (60 °C, 80 °C and 100 °C) are shown in Figs. 5.8(b) – 5.10(b). For a given T_{sat}, a significantly larger variation in f_0 appears depending on the choice of the working fluid, compared to the case of setting the pressure P_{max}. This suggests that the externally imposed temperature in the HHX as set by the heat source, together with the selection of the working fluid have an important role to play in setting the maximum cycle pressure and determining the frequency of the device. As the HHX temperature increases, so does the overall value of f_0.

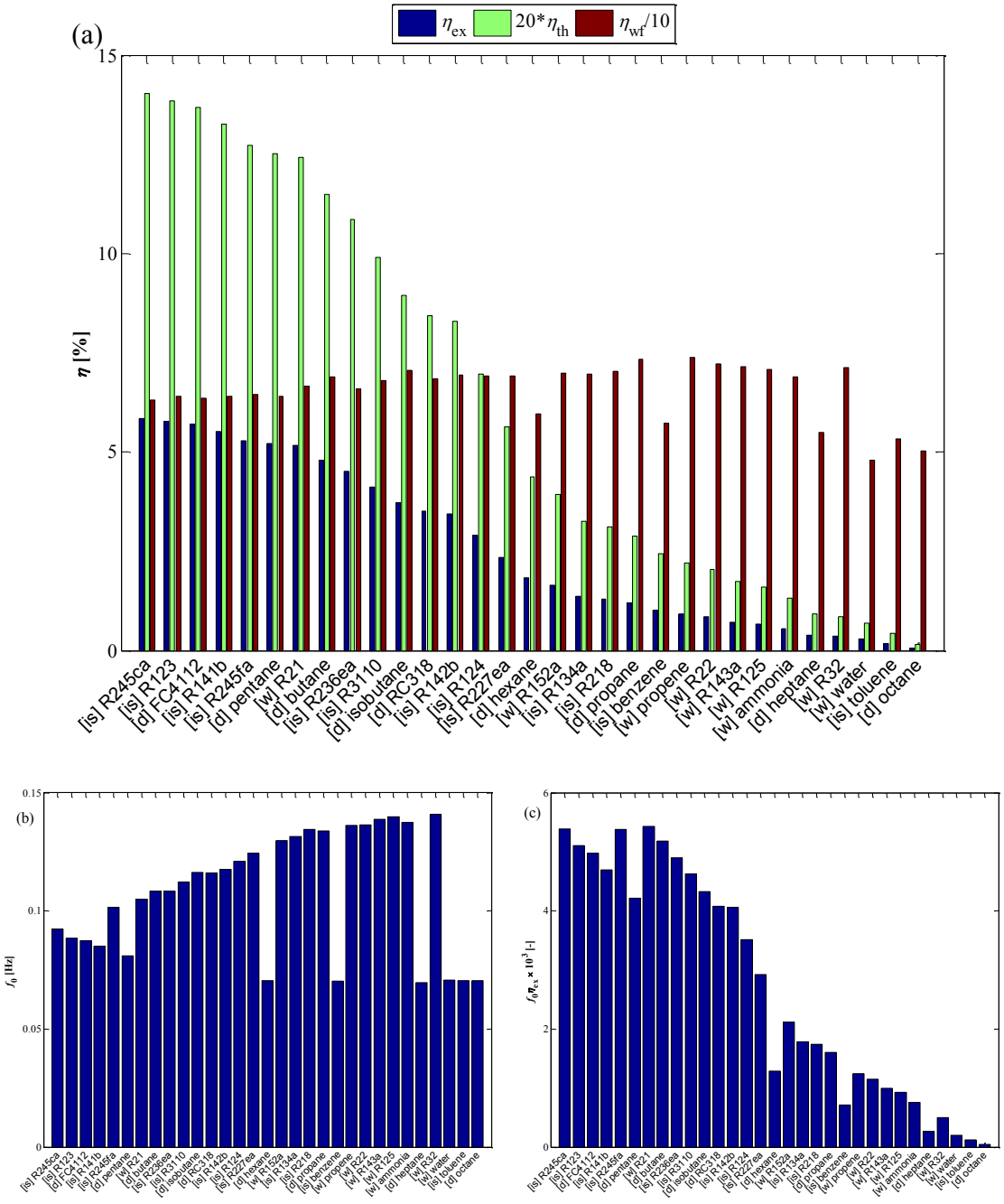


Figure 5.8: (a) Exergy efficiency η_{ex}, thermal efficiency η_{th} and working fluid efficiency η_{wf}, (b) oscillation frequency f_0, and (c) normalised power output per unit heat input $f_0\eta_{ex}$ for different working fluids and a system working with a hot heat exchanger temperature of 333.15 K.

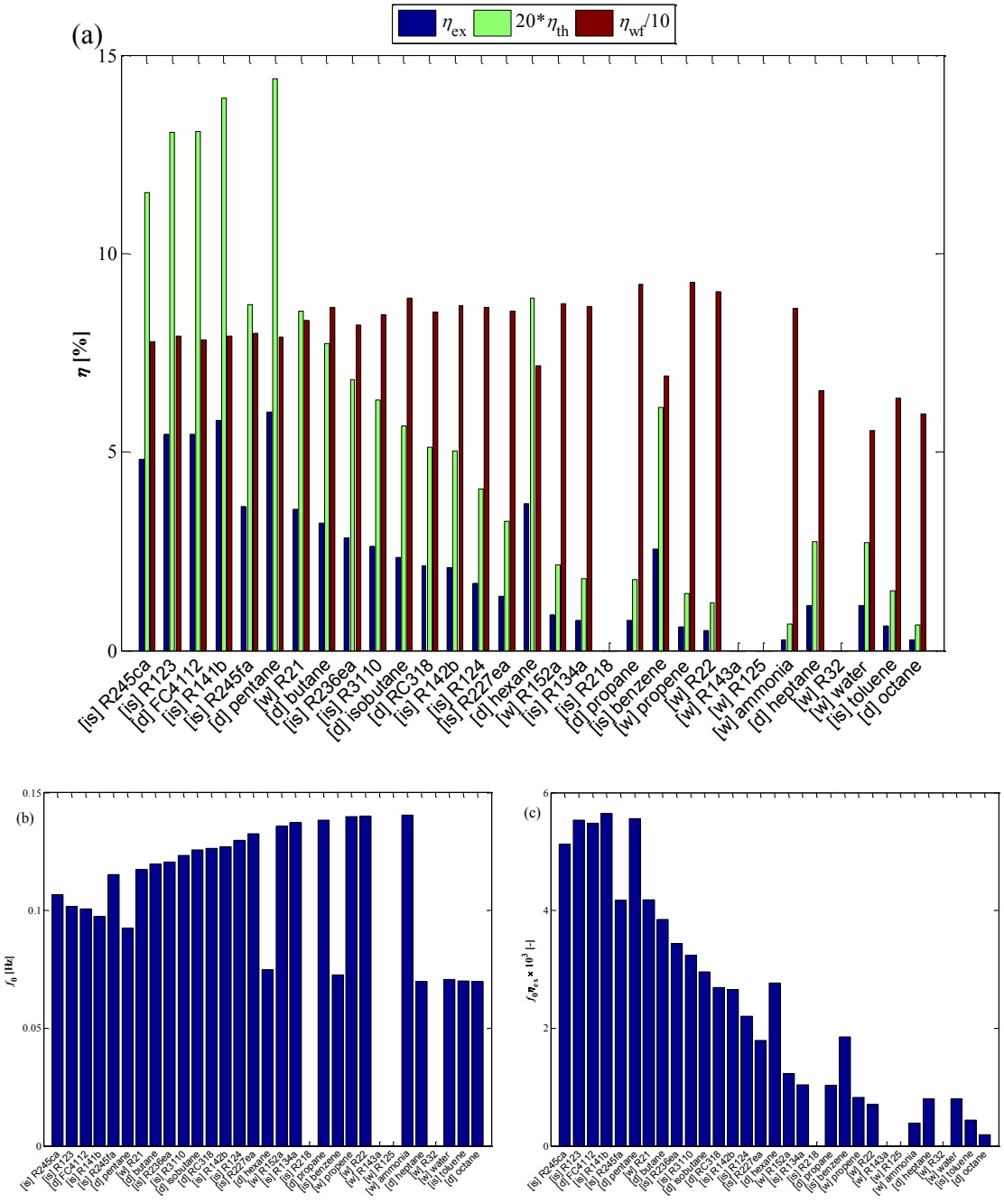


Figure 5.9: (a) Exergy efficiency η_{ex}, thermal efficiency η_{th} and working fluid efficiency η_{wf}, (b) oscillation frequency f_0, and (c) normalised power output per unit heat input $f_0\eta_{ex}$ for different working fluids and a system working with a hot heat exchanger temperature of 353.15 K.

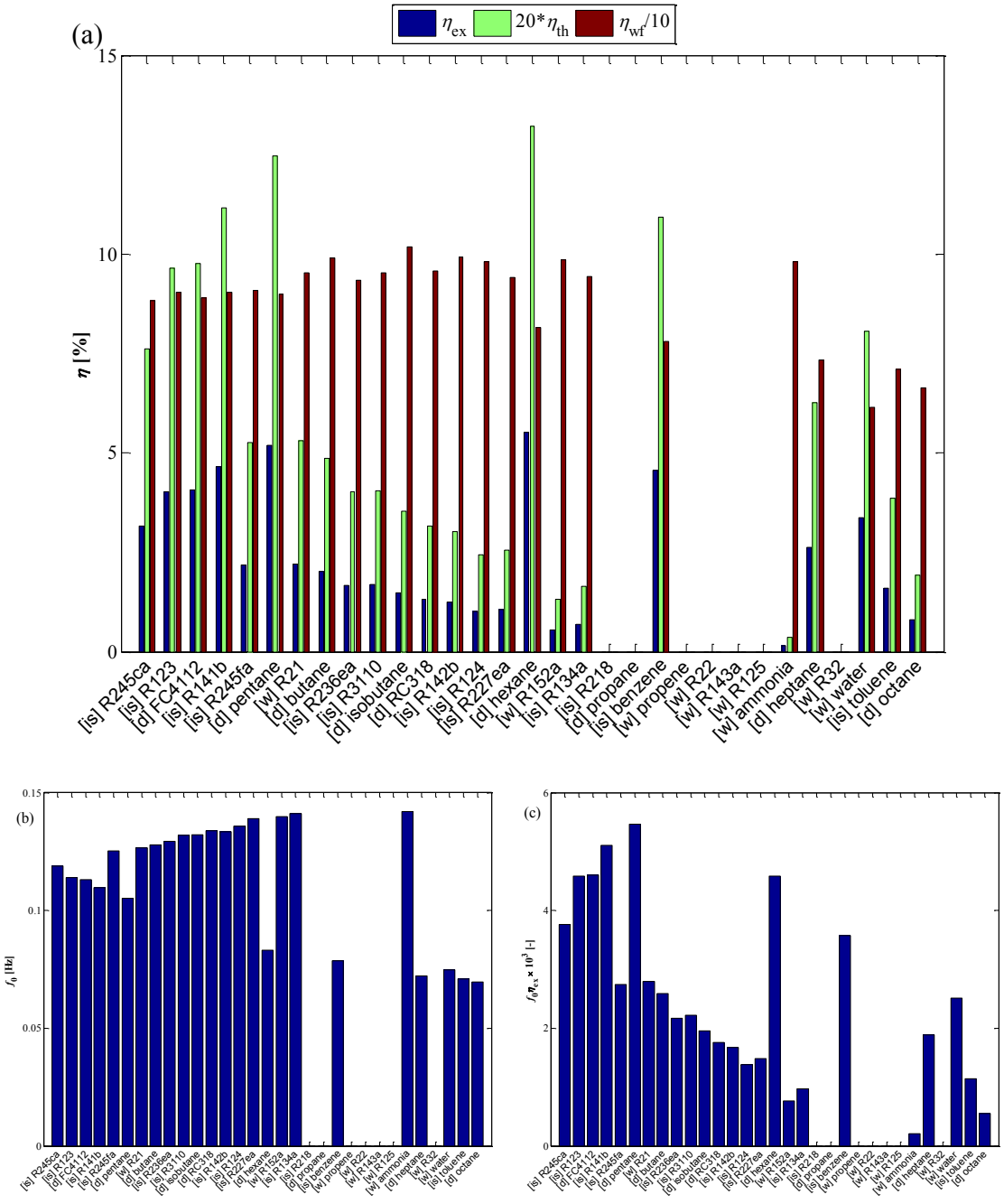


Figure 5.10: (a) Exergy efficiency η_{ex}, thermal efficiency η_{th} and working fluid efficiency η_{wf}, (b) oscillation frequency f_0, and (c) normalised power output per unit heat input $f_0\eta_{ex}$ for different working fluids and a system working with a hot heat exchanger temperature of 373.15 K.

Finally, it is important, as in the imposed pressure scenario above, to note that fluids associated with high NIFTE exergy efficiencies η_{ex}, generally, also exhibit the greatest normalised hydraulic/pumping power outputs per unit heat input $f_0\eta_{ex}$ (see Figs. 5.8(c) to 5.10(c)), due to the greater sensitivity of this performance indicator to η_{ex} compared to the operational frequency f_0. Additional fluids that show a strong performance with respect to the normalised power output $f_0\eta_{ex}$ are R245fa and R21 at low temperatures (333.15 K, or 60 °C; Fig. 5.8(c)) and R141b at intermediate and higher temperatures (353.15 K and 373.15 K, or 80 °C and 100 °C; Figs. 5.9(c) and 5.10(c)). In the case of R245fa and R21 one notes that these two working fluids are not only amongst those that exhibit relatively high exergy efficiencies η_{ex}, but also show a high frequency f_0 (see Figs. 5.8(b) – 5.10(b)).

Further result interpretation

Figure 5.11(a) shows, for all working fluids, the exergy efficiency η_{ex} predicted by the NIFTE DHX_{TL} model for HHX temperatures T_{sat} = 333.15 K, 353.15 K and 373.15 K (60 °C, 80 °C and 100 °C) against the corresponding saturation pressure $P_{max}(T_{sat})$, always with the CHX at 293.15 K (20 °C). The data collapse onto a single trend line, suggesting that the HHX temperature affects η_{ex} mostly through its effect on P_{max}. A maximum η_{ex} is found at $P_{max} \simeq 4$ bar, and amounts to 6%. It may be expected that more work will be done in the load at higher P_{max}, leading to increased η_{ex}. However, the thermal/condensation/feedback losses also increase at higher pressures and eventually counteract the increase in useful work. This is an important finding, with significant implications for the design and operation of these devices. It suggests that for a particular device arrangement, setting and application, there is an optimum efficiency (and thus power output; as suggested in the results from both application scenarios) that can be achieved by tuning the maximum saturation pressure via the selection of the right working fluid. Further improvements will only be possible by other changes to the device's design and/or construction.

The exergy efficiency η_{ex} predicted by the DHX_{TL} model for all working fluids is plotted against the corresponding saturation temperature of the fluids in Fig. 5.11(b) at a fixed head P_{max}. The efficiency increases at higher heads up to 30 m and then decreases again, in accordance with Fig. 5.11(a). Further, we observe that when working against 1 m and 10 m heads, an increase in T_{sat} (for a given P_{max}) leads generally to a reduced η_{ex}, while at 30 m and 100 m heads the trend reverses such that an increase in T_{sat} leads to an increased η_{ex}.

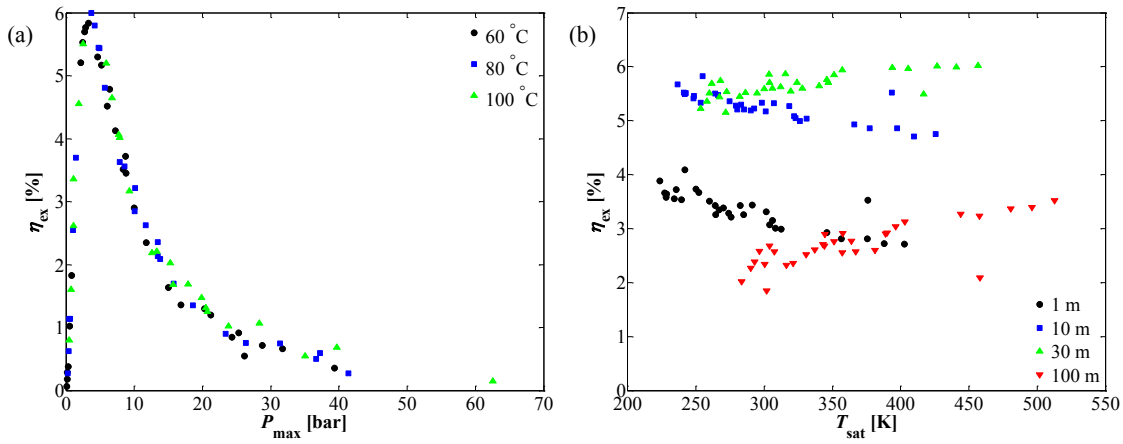


Figure 5.11: The exergy efficiency η_{ex} predicted by the DHX_{TL} model for: (a) a system working with a hot heat exchanger temperature of 60 °C, 80 °C and 100 °C, and a cold heat exchanger temperature of 293 K, against the maximum pressure for all working fluids, and (b) a system working against a 1 m, 10 m, 30 m and 100 m head, with a suction/supply pressure of 1 atm, against the maximum saturation temperature for all working fluids.

Finally, Fig. 5.12 shows, for a given heat source temperature T_{sat} (a,b) or pumping load pressure P_{max} (c,d): (i) the maximum efficiency that can be achieved by any investigated working fluid in an ideal cycle/process, and (ii) our best estimate of the efficiency of the nominal NIFTE device, again over all fluids. Although maximum η_{wf} of 14 – 15% are predicted over a reasonably broad range of conditions, the NIFTE attains thermal efficiencies η_{th} no higher than 1 – 2%, due to valve and thermal losses, thus indicating a clear and significant potential for improvement. The maximum NIFTE efficiency is achieved at a temperature of ~450 K (180°C) or pressure of ~ 6 bar. This maximum thermal efficiency corresponds to an exergy efficiency η_{ex} of ~6% (see Fig. 5.12(b,d)). By means of comparison, the experimental NIFTE pumping prototype described in Ref. [2] demonstrated an exergy efficiency 5× lower than this value (for the nominal configuration) with $\eta_{ex} = 1.12\%$. This was achieved with a 150 W (electrical/Joule) heating power supplied to the HHX, a cooling stream flow that allowed a CHX temperature of 4 °C and *n*-pentane as the working fluid [2]. As was the case previously, further improvements relative to this performance are possible by design and/or construction modifications that allow the minimisation of the stated loss mechanisms.

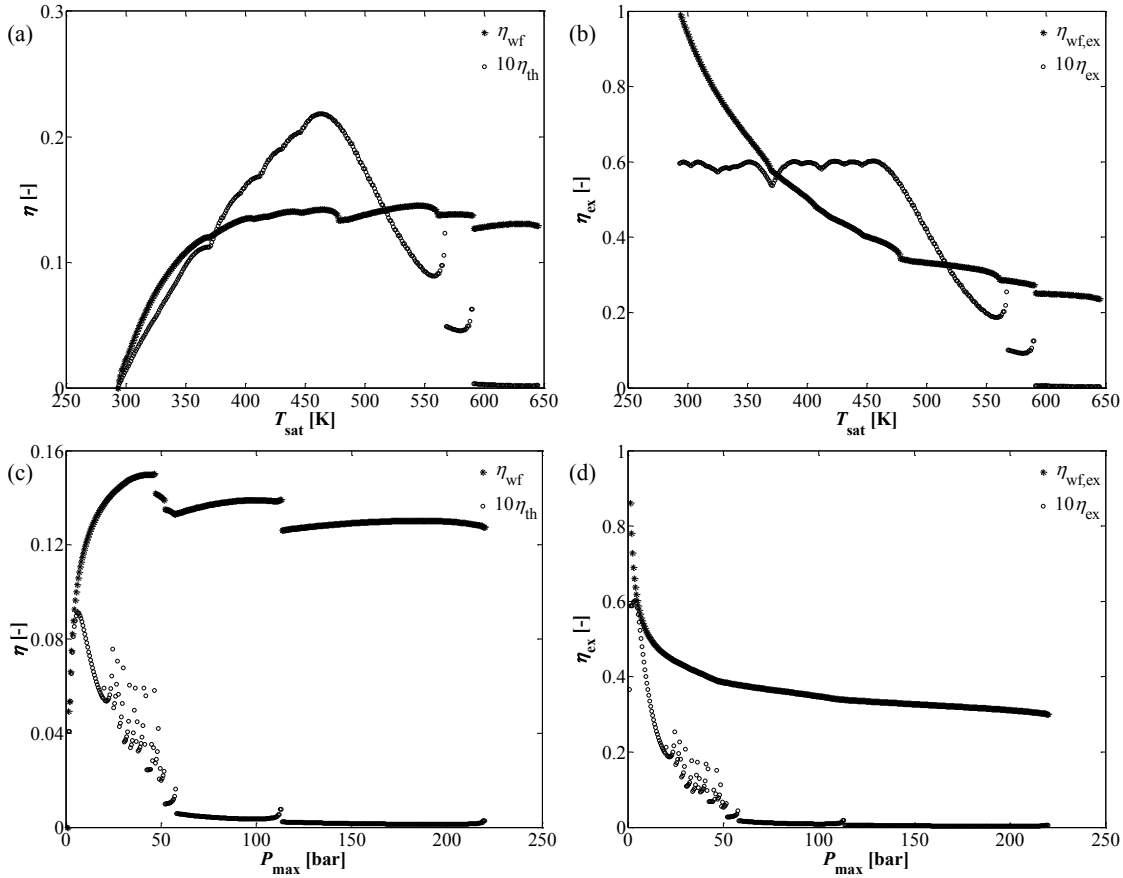


Figure 5.12: With the heat source (HHX) temperature T_{sat} set to some (variable) value and the heat sink (CHX) temperature set to 20 °C: (a) maximum ideal working fluid thermal efficiency η_{wf} over all working fluids tested in this study and NIFTE device thermal efficiency η_{th} (shown here multiplied by a factor of $\times 10$), and (b) maximum ideal working fluid exergy efficiency $\eta_{wf,ex}$ over all working fluids tested in this study and NIFTE device exergy efficiency η_{ex} (multiplied by a factor of $\times 10$). With the load pressure P_{max} set to some (variable) value and the suction/supply pressure set to 1 atm: (c) maximum ideal working fluid thermal efficiency η_{wf} over all working fluids tested in this study and NIFTE device thermal efficiency η_{th} (multiplied by a factor of $\times 10$), and (d) maximum ideal working fluid exergy efficiency $\eta_{wf,ex}$ over all working fluids tested in this study and NIFTE device exergy efficiency η_{ex} (shown here multiplied by a factor of $\times 10$).

5.4 Summary of chapter findings

The thermal efficiency of an idealised two-phase, positive-displacement cycle that can be attributed entirely to the thermodynamic properties of the working fluid was evaluated for select fluids: ammonia, *n*-pentane, water and R245ca. A maximum working fluid efficiency was observed as the temperature approached the

critical temperature of the working fluid. The effects of several thermodynamic properties on, firstly, the working fluid thermal efficiency η_{wf}, and then, the exergy efficiency η_{ex} of the NIFTE pumping engine were investigated. The latter study was confined to *n*-pentane, which was the working fluid used in an earlier experimental investigation of a prototype NIFTE pumping device. It was found that the change in specific volume change due to vaporisation Δv_{vap} was the most dominant property in terms of its ability to determine the magnitude and control the trends of these efficiencies. In addition to this, the maximum saturation pressure P_{max} and the specific entropy change due to vaporisation Δs_{vap} both had significant effects on these efficiencies. A simultaneous combination of Δv_{vap} and P_{max}, with all other properties held constant, captured the variations in η_{wf} and η_{ex} over the whole range of investigated saturation temperatures T_{sat} (maximum temperatures in the cycle, during the heat addition and vaporisation processes). In addition to this, a maximum was observed in η_{ex} at a maximum saturation temperature of around $T_{sat} \approx 360\,\mathrm{K}$ ($\approx 90\,^{\circ}\mathrm{C}$). This was determined to be due to the inclusion of a parasitic thermal loss parameter in the dynamic heat exchanger model, which introduced a competing effect to that of evaporation and condensation of the working fluid on the heat exchangers, occurring on the chamber walls of the nominally adiabatic vapour volume. Working fluids with large Δv_{vap}, small Δs_{vap} and large P_{max} were shown to allow better performance.

Proceeding further and using the dynamic heat exchanger NIFTE model with a thermal loss parameter $\mathrm{DHX_{TL}}$ model, thirty one pure component working fluids were investigated under two operating scenarios: (i) an externally imposed maximum operating pressure (head) in the load, and (ii) an externally imposed maximum operating temperature in the hot heat exchanger (HHX). In the first case, the $\mathrm{DHX_{TL}}$ model predicted similar oscillation/operational frequencies for all working fluids. In addition to this, the overall frequency increased as the maximum pressure increased. Similarly, the overall efficiency measures generally increased as the maximum head increased at low heads, particularly with larger chained components which performed better at a higher maximum system heads. At high heads, the opposite trend was observed, with the exergy efficiency showing a deterioration. R22 and R134a were identified as promising working fluids at low heads, R143a and R32 at intermediate heads, and *n*-butane/isobutane at high heads. *N*-butane and R142b maintained a reasonable performance over a range of heads 1 m – 30 m. For the scenario where the HHX temperature was set, it was noted that increasing T_{sat} also increased the overall oscillation frequency. When working against low heads (up to 10 m), an increase in T_{sat} (for a given P_{max}) led generally

to a reduction in exergy efficiency η_{ex}, while at high heads (above 30 m and up to 100 m) the trend reversed such that an increase in T_{sat} led to an improvement in η_{ex}. Dry and isentropic working fluids tended to allow for higher exergy efficiency predictions in this case. R245ca, R123, FC4112 and *n*-pentane, at lower temperatures (below 80 °C), and *n*-pentane/hexane at higher ones (above 80 °C), displayed high efficiencies. Finally, maximum ideal η_{wf} of 14 – 15% were predicted for the 'best' working fluid over a range of conditions, whereas the NIFTE attained thermal efficiencies no higher than 1 – 2% (exergy efficiencies ~6%) due to valve and thermal losses. This finding suggests that the working fluid can lead to a 5× efficiency improvement relative to the experimental NIFTE prototype described in Ref. [2], where an exergy efficiency of 1.12% was achieved.

6 Conclusions and Future Work

The linear temperature profile (LTP) model of the NIFTE with inertia was compared to previous investigations carried out on the NIFTE thermofluidic oscillator [2, 34, 35] in which all inertial effects were neglected. When comparing predictions from the inertive LTP model with those from a non-inertive LTP model, significant differences were found. Further, the predictions from the non-inertive model diverge significantly from experimental observations. It was concluded that inertia may be an important factor in the modelling of this system. The effects of: (i) fluid flow drag (resistance) and inertia in the load; as well as (ii) feedback valve drag, on the marginal gain (minimum temperature difference between the source and sink heat exchangers necessary for operation), frequency and exergetic efficiency of the NIFTE were then investigated. Increases in load resistance and inertia had little effect on the gain and oscillation frequency predicted by the inertive LTP model, except at high values of resistance and inertia, when there was an increase in gain and decrease in frequency. These observations were not in accordance with corresponding non-inertive model predictions. However the gain and frequency predictions in the absence of inertia were quantitatively un-physical. Of interest to the designer is the finding that decreasing the feedback valve resistance or increasing the load inertia led to a higher efficiency, while an increase in load resistance led to an increase in efficiency until a maximum was reached, after which the efficiency decreased again. When the non-inertive model was developed in Refs. [2, 34, 35], certain approximations were made which have been shown in the present work not to be true generally in describing the system over a range of conditions.

Two models for the two-phase heat transfer in the NIFTE were compared to the inertive LTP model; one involving a constant temperature difference (CTD) between the heat exchangers and the working fluid, and the other allowing for a dynamic heat exchange (DHX) process to take place between the heat exchangers and the working fluid by accounting for the heat capacity of the heat exchanger blocks. The effects of the

flow resistance and inertia in the liquid feedback connection (tube and valve) on the marginal stability oscillation frequency and resulting exergetic efficiency of the device were studied. The CTD model predicted similar (and realistic, when compared to a prototype pumping device) oscillation frequencies to the LTP and DHX models. However, it predicted considerably higher (and unrealistic) exergetic efficiencies than those measured experimentally. This was attributed to the lack of a thermal resistance in the CTD model.

The effects of the heat storage parameter (related to the heat capacity of the heat exchangers) on the oscillation frequency and exergetic efficiency of the DHX model were also investigated. The selected nominal value was found to allow realistic predictions of the NIFTE behaviour. When the heat exchanger capacity parameter was sufficiently low, relating to unrealistic oscillation amplitudes, the DHX model presented discontinuities in the frequency and efficiency when parameters associated with the power cylinder were varied. In fact, discontinuities in the system performance were observed in all three models when perturbing the hydrostatic capacitance and inertia in the power cylinder, and in the LTP and CTD models also when perturbing the inertia in the feedback connection. Importantly, the DHX model was observed to be more robust with respect to the appearance of these discontinuities. Finally, it was found that the feedback connection had a reduced ability to regulate the operation frequency in high load conditions, and a reduced ability to regulate the resulting efficiency in low load conditions.

In conclusion, it was found that the introduction of inertia in the modelling of the NIFTE device was essential to make realistic performance predictions over a range of configurations. In addition to this, though the LTP and DHX models predict the frequency of oscillation well, both overestimate the exergetic efficiency. This was attributed to the neglect of other thermal losses in the NIFTE device, which were identified in Chapter 4.

A thermal loss impedance which accounted for exergy losses due to parasitic conjugate heat transfer and phase change in the vapour volume of the NIFTE was developed and incorporated into the LTP and DHX models. Results from a parametric study varying the feedback resistance and load resistance on the LTP and DHX models, including and excluding the thermal loss impedance, were presented and compared to experimental data from an early NIFTE prototype, as reported by Smith [2]. When varying the load resistance, the thermal loss impedance was found to have little effect on the frequencies predicted by the LTP and DHX models including and excluding the thermal loss impedance. The models showed that an increase in load resistance led to a decrease in oscillation frequency, agreeing with the trend observed

experimentally. The LTP model predicted frequencies twice those observed experimentally, whereas the DHX model matched the experimental data for oscillation frequency well. The DHX model predicted improved exergetic efficiencies in response to higher load resistances, whereas the LTP model predicted a maximum efficiency at a load resistance ~ 40 % its nominal value.

It was further found that the LTP and DHX models without the thermal loss impedances predicted the trend of experimental data for variations in the feedback resistance well, with an increase in feedback resistance leading to a decrease in oscillation frequency. Experimentally, the NIFTE was shown to operate at frequencies of $0.1 - 0.2$ Hz, which the LTP and DHX models including and excluding the thermal loss impedance were shown to capture without parameter fitting. Moreover, it was found that the predictions form the DHX model including the thermal loss impedance most closely match the experimentally obtained values.

In addition, the NIFTE prototype demonstrated efficiencies of up to about 1.5 % when the feedback resistance was varied. The LTP and DHX models neglecting the thermal loss impedance captured the trend of increasing efficiency with increasing feedback resistance. However, the LTP and DHX models that did not account for the thermal losses overestimated the efficiency by 11 and 30 times, respectively. The inclusion of the thermal loss impedance improved the predictions for the exergetic efficiency of both the LTP and DHX models, with little difference between the isothermal and adiabatic boundary conditions applied on the outside of the device. The LTP model with the thermal loss underestimates the measured exergetic efficiency and therefore did not allow for additional losses to be included.

From the results it was concluded that the inertive DHX model with the addition of the thermal loss impedance was the best model to predict the oscillation frequency and exergetic efficiency of the NIFTE. However, the NIFTE prototype was shown to operate with lower efficiencies compared to other devices using the same working fluid and similar working conditions. Therefore further work needs to be done in optimising the device configuration to achieve a higher efficiency and power (pumping) output.

The thermal efficiency of an idealised two-phase, positive-displacement cycle that could be attributed entirely to the thermodynamic properties of the working fluid was evaluated for select fluids: ammonia, *n*-pentane, water and R245ca. A maximum working fluid efficiency was observed as the temperature approached the critical temperature of the working fluid. The effects of several thermodynamic properties on, firstly, the working fluid thermal efficiency η_{wf}, and then, the exergy efficiency η_{ex} of the NIFTE pumping

engine were investigated. The latter study was confined to *n*-pentane, which was the working fluid used in an earlier experimental investigation of a prototype NIFTE pumping device [2, 34, 35]. It was found that the change in specific volume change due to vaporisation Δv_{vap} was the most dominant property in terms of its ability to determine the magnitude and control the trends of these efficiencies. In addition to this, the maximum saturation pressure P_{max} and the specific entropy change due to vaporisation Δs_{vap} both had significant effects on these efficiencies. A simultaneous combination of Δv_{vap} and P_{max}, with all other properties held constant, captured the variations in η_{wf} and η_{ex} over the whole range of investigated saturation temperatures T_{sat} (maximum temperatures in the cycle, during the heat addition and vaporisation processes). In addition to this, a maximum was observed in η_{ex} at a maximum saturation temperature of around $T_{\text{sat}} \approx 360\,\text{K}$ ($\approx 90\,^{\circ}\text{C}$). This was determined to be due to the inclusion of a parasitic thermal loss parameter in the dynamic heat exchanger model, which introduced a competing effect to that of evaporation and condensation of the working fluid on the heat exchangers, occurring on the chamber walls of the nominally adiabatic vapour volume. Working fluids with large Δv_{vap}, small Δs_{vap} and large P_{max} were shown to allow better performance.

Proceeding further and using the dynamic heat exchanger NIFTE model with a thermal loss parameter DHX_{TL}, thirty one pure component working fluids were investigated under two operating scenarios: (i) an externally imposed maximum operating pressure (head) in the load, and (ii) an externally imposed maximum operating temperature in the hot heat exchanger (HHX). In the first case, the DHX_{TL} model predicted similar oscillation/operational frequencies for all working fluids. In addition to this, the overall frequency increased as the maximum pressure increased. Similarly, the overall efficiency measures generally increased as the maximum head increased at low heads, particularly with larger chained components which performed better at a higher maximum system heads. At high heads, the opposite trend was observed, with the exergy efficiency showing a deterioration. R22 and R134a were identified as promising working fluids at low heads, R143a and R32 at intermediate heads, and *n*-butane/isobutane at high heads. *N*-butane and R142b maintained a reasonable performance over a range of heads 1 m – 30 m. For the scenario where the HHX temperature was set, it was noted that increasing T_{sat} also increased the overall oscillation frequency. When working against low heads (up to 10 m), an increase in T_{sat} (for a given P_{max}) led generally to a reduction in exergy efficiency η_{ex}, while at high heads (above 30 m and up to 100 m) the trend reversed such that an increase in T_{sat} led to an improvement in η_{ex}. Dry and isentropic working fluids tended to allow

for higher exergy efficiency predictions in this case. R245ca, R123, FC4112 and *n*-pentane, at lower temperatures (below 80 °C), and *n*-pentane/hexane at higher ones (above 80 °C), displayed high efficiencies. Finally, maximum ideal η_{wf} of 14 – 15% were predicted for the 'best' working fluid over a range of conditions, whereas the NIFTE attained thermal efficiencies no higher than 1 – 2% (exergy efficiencies ~6%) due to valve and thermal losses. This finding suggests that the working fluid can lead to a 5× efficiency improvement relative to the experimental NIFTE prototype described in Ref. [2], where an exergy efficiency of 1.12% was achieved.

In closing, it is estimated that, with optimised designs and well selected working fluids, the NIFTE technology may be capable of thermal efficiencies in the range of 1 – 5 % when operating with low-grade heat at temperatures between 50 and 100 °C, with current best performance of approximately 1.5% at 80 °C.

6.1 Future work

6.1.1 Experimental data

In order to validate the models presented in this thesis, experimental data was used from Ref. [2]. Although this data was useful, it was limited and in order to validate the current models further with higher certainty, and future models for the NIFTE, it is important to carry out experiments on the NIFTE. Currently, experimental data is only available for one configuration of the NIFTE, using *n*-pentane as the working fluid, with two setups for the load. A larger set of data covering multiple configurations, loads and working fluids would aid increasing the confidence in the validity of the models, and any future models developed for the NIFTE.

6.1.2 Heat exchanger modelling

As previously mentioned, the heat exchangers and the heat-exchange process in the NIFTE is the most important component, however it is also the least understood. Modelling of the heat exchangers can improve the understanding of their behaviour and performance, and as such can aid in designing and obtaining an optimal configuration for the heat exchangers. In addition, incorporating a detailed heat exchanger model into the existing models for the NIFTE can improve the predictions, specifically the exergetic and thermal

efficiencies.

6.1.3 Working fluid design

The majority of the work carried out on the NIFTE, both experimentally and theoretically, is based on *n*-pentane as the working fluid. In Chapter 5, thirty one working fluids were investigated with the DHX_{TL} model and it was seen that the working fluid used in the NIFTE had a significant effect on the performance of the engine. It is important to note that the optimal working fluid for the NIFTE will depend on the application it is designed for, that is the temperature of the heat source and sink or a maximum operating pressure. Further work in this direction will help identify optimal configurations and would be of interest.

6.1.4 Optimisation

All the investigations carried out on the NIFTE models thus far have involved varying a single parameter to observe the effects on the performance indicators. However it is not known what effects are of varying multiple parameters simultaneously. Carrying out a multi-parametric study will help understand the behaviour of the NIFTE over the whole parameter space. In addition, developing an optimisation algorithm can aid with future design of the engine.

Bibliography

[1] Thermofluidics. http://youtu.be/mi7xO-PQtEU. online video clip, uploaded 9 Jun. 2010, accessed 17 Feb. 2012.

[2] T. C. B. Smith. *Thermally Driven Oscillations in Dynamic Applications*. PhD thesis, University of Cambridge, Cambridge, UK, 2006.

[3] S. Carnot. *Rèflexion sur la Puissance Mortice du feu sur le Machine a Dèvelopper cette Puissance*. Bachelier Libraire, Paris, 1824.

[4] E. Clapeyron. Puissance motrice de la chaleur. *Journal de l'Ecole Royale Polytechnique*, XIV:153–190, 1834.

[5] R. Clausius. *The Mechanical Theory of Heat: With Its Applications to the Steam-engine and to the Physical Properties of Bodies*. J. Van Voorst, 1867.

[6] J. R. Elliott and C. T. Lira. *Introductory Chemical Engineering Thermodynamics*. Prentice Hall, New Jersey, 2012.

[7] R. Sathre. Comparing the heat of combustion of fossil fuels to the heat accumulated by their lifecycle greenhouse gases. *Fuel*, 115:674–677, 2014.

[8] W. H. J. Graus and M. V. Worrell. International comparison of energy efficiency of fossil power generation. *Energy Policy*, 35:3936–3951, 2007.

[9] Kyoto protocol. http://unfccc.int/kyoto_protocol/items/2830.php.

[10] W. Graus and E. Worrell. Trend in efficiency and capacity of fossil power generation in the eu. *Energy Policy*, 37:2147–2160, 2009.

[11] S. Shafiee and E. Topal. When will fossil fuel reserves be diminished? *Energy Policy*, 37:181–189, 2009.

[12] Renewables 2011 global status report. http://www.ren21.net/Portals/0/documents/Resources/GSR2011_FINAL.pdf.

[13] Y. Ammar, S. Joyce, R. Norman, Y. Wang, and A. P. Roskilly. Low grade thermal energy sources and uses from the process industry in the uk. *Applied Energy*, 89:3–20, 2012.

[14] C. W. Chan, J. Ling-Chin, and A. P. Roskilly. Reprint of ä review of chemical heat pumps, thermodynamic cycles and thermal energy storage technologies for low grade heat utilisation. *Applied Thermal Engineering*, 53:160–176, 2013.

[15] G. Axelsson, E. Gunnlaugsson, T. Jónasson, and M. Ólafsson. Low-temperature geothermal utilization in iceland decades of experience. *Geothermics*, 39:329–338, 2010.

[16] P. E. Grohnheit and B. O. Gram Mortensen. Competition in the market for space heating. district heating as the infrastructure for competition among fuels and technologies. *Energy Policy*, 31:817–826, 2003.

[17] R. Z. Wang and R. G. Oliveira. Adsorption refrigeration - an efficient way to make good use of waste heat and solar energy. *Progress in Energy and Combustion Science*, 32:424–458, 2006.

[18] T. C. Hung, T. Y. Shai, and S. K. Wang. A review of organic Rankine cycles (ORCs) for the recovery of low-grade waste heat. *Energy*, 22:661–667, 1997.

[19] C. J. Winter. Energy efficiency, no: Its exergy efficiency! *International Journal of Hydrogen Energy*, 32:4109–4111, 2007.

[20] Electratherm. http://electratherm.com/docs/ElectraTherm_Electronic_Brochure.pdf. online brochure, accessed 4 Jul. 2012.

[21] Enerbasque. http://www.enerbasque.com/en/files/P25DSen.pdf. online brochure, accessed 4 Jul. 2012.

[22] G. W. Swift. Thermoacoustic engines. *Journal of the Acoustical Society of America*, 84:1148–1180, 1988.

[23] J. Wheatley, T. Hofler, G. W. Swift, and A. Migliori. An intrinsically irreversible thermoacoustic heat engine. *Journal of the Acoustical Society of America*, 74:153–170, 1983.

[24] J. Wheatley, T. Hofler, G. W. Swift, and A. Migliori. Experiments with an intrinsically irreversible acoustic heat engine. *Physical Review Letters*, 50:499–502, 1983.

[25] P. H. Ceperley. A pistonless Stirling engine - the traveling wave heat engine. *Journal of the Acoustical Society of America*, 66:1508–1513, 1979.

[26] C. West. The Fluidyne heat engine. Report AERE R6775, Atomic Energy Authority Research Group, 1971.

[27] C. D. West and R. B. Pandey. Laboratory prototype Fluidyne water pump. In *IECEC 1981: Proceedings of the 16th Intersociety Energy Conversion Engineering Conference*, pages 1916–1918, Atlanta (GA), USA, 1981.

[28] C. W. Stamers. The operation of the Fluidyne heat engine at low differential temperatures. *Journal of Sound and Vibration*, 63:507–516, 1979.

[29] R. W. Redlich and D. M. Berchowitz. Linear dynamics of free-piston Stirling engines. *Proceedings of the Institution of Mechanical Engineers - Part A: Power and Process Engineering*, 199:203–213, 1985.

[30] G. Walker and J. R. Senft. *Free Piston Stirling Engines*. Springer, Berlin, 1985.

[31] S. Moldenhauer, A. Thess, C. Holtmann, and C. Fernández-Aballí. Themodynamic analysis of a pulse tube engine. *Energy Conversion and Management*, 65:810–818, 2013.

[32] D. G. Thombare and S. K. Verma. Technological development in the Stirling cycle engines. *Renewable and Sustainable Energy Reviews*, 12:1–38, 2008.

[33] G. W. Swift. *Thermoacoustics: A Unifying Perspective for Some Engines and Refrigerators*. Acoustical Society of America, New York, 2002.

[34] T. C. B. Smith. Power dense thermofluidic oscillators for high load applications. In *IECEC 2004: Proceedings of the 2nd International Energy Conversion Engineering Conference*, pages 2004–5758, Providence (RI), USA, 2004.

[35] T. C. B. Smith. Asymmetric heat transfer in vapour cycle liquid-piston engines. In *ISEC 2005: Proceedings of the 12th International Stirling Engine Conference and Technology Exhibition*, pages 302–314, Durham, UK, 2005.

[36] C. Care. *Technology for Modelling: Electrical Analogies, Engineering Practice and Development of Analogue Computing*. Springer, London, 2010.

[37] N. D. Deveau, Y. H. Ma, and R. Datta. Beyond Sieverts law: A comprehensive microkinetic model of hydrogen permeation in dense metal membranes. *Journal of Membrane Science*, 437:298–311, 2013.

[38] S. Raël and M. Hinaje. Using electrical analogy to describe mass and charge transport in lithium-ion batteries. *Journal of Power Sources*, 222:112122, 2013.

[39] Q. S. Zhu, S. Y. Li, J. Liu, and L. Q. Zeng. Using l-systems for simulating virtual plant plasticity related to water status. *Journal of Computational and Theoretical Nanoscience*, 10:561–568, 2013.

[40] H. F. Olson. *Dynamical Analogies*. Van Nostrand, 1958.

[41] S. Backhaus and G. W. Swift. A thermoacoustic-Stirling heat engine: Detailed study. *Journal of the Acoustical Society of America*, 107:3148–3166, 2000.

[42] B. J. Huang and M. D. Chuang. System design of orifice pulse-tube refrigerator using linear flow network analysis. *Cryogenics*, 36:889–902, 1996.

[43] C. N. Markides and T. C. B. Smith. A dynamic model for the efficiency optimization of an oscillatory low grade heat engine. *Energy*, 36:6967–6980, 2011.

[44] K. M. Godshalk, C. Jin, Y. K. Kwong, G. W. Swift, and R. Radebaugh. Characterization of 350 hz thermoacoustic driven orifice pulse tube refrigerator with measurements of the phase of the mass flow and pressure. *Advances in Cryogenic Engineering*, 41:1411–1418, 1996.

[45] H. Chen, D. Y. Goswami, and E. K. Stefanakos. A review of thermodynamic cycles and working fluids for the conversion of low grade heat. *Renewable and Sustainable Energy Reviews*, 14:3059–3067, 2010.

[46] B. Saleh, G. Koglbaur, M. Wendland, and J. Fischer. Working fluids for low-temperature organic Rankine cycles. *Energy*, 32:1210–1221, 2007.

[47] U. Drescher and D. Brüggemann. Fluid selection for the Organic Rankine Cycle (ORC) in biomass power and heat plants. *Applied Thermal Engineering*, 27:223–228, 2007.

[48] H. D. Madhawa Hettiarachchi, M. Golubovic, W. M. Worek, and Y. Ikegami. Optimum design criteria for an organic Rankine cycle using low-temperature geothermal heat sources. *Energy*, 32:1698–1706, 2007.

[49] R. Solanki, A. Galindo, and C. N. Markides. Dynamic modelling of a two-phase thermofluidic oscillator for efficient low grade heat utilization: Effect of fluid inertia. *Applied Energy*, 89:156–163, 2012.

[50] R. Solanki, A. Galindo, and C. N. Markides. The role of heat exchange on the behaviour of a two-phase thermofluidic oscillator. *Applied Thermal Engineering*, 53:177–187, 2013.

[51] R. Solanki, R. Mathie, A. Galindo, and C. N. Markides. Modelling of a two-phase thermofluidic oscillator for low-grade heat tilisation: accounting for irreversible thermal losses. *Applied Energy*, 106:337–354, 2013.

[52] C. N. Markides, R. Solanki, and A. Galindo. Working fluid selection for a two-phase thermofluidic oscillator: Effect of thermodynamic properties. *Applied Energy*, 2014:167–185, 2014.

[53] D. F. Young, B. R. Munson, H. H. Okiishi, and W. W. Huebsch. *A Brief Introduction to Fluid Mechanics*. John Wiley and Sons, New Jersey, 2007.

[54] D. A. P. Jayasinghe, M. S. Letelier, and H. J. Leutheusser. Frequency-dependant friction is oscillatory laminar pipe flow. *International Journal of Mechanical Sciences*, 16:819–827, 1974.

[55] B. Ünsal, S. Ray, F. Durst, and Ö. Ertunç. Pulsating laminar pipe flows with sinusoidal mass flux variations. *Fluid Dynamics Research*, 37:317–333, 2005.

[56] J. P. Homon. *Heat Transfer*. McGraw-Hill, London, 1997.

[57] R. C. Dorf and R. H. Bishop. *Modern Control Systems*. Addison-Wesley, Harlow, 1997.

[58] R. G. Powell. *Introduction to Electric Circuits*. Arnold, London, 1995.

[59] R. Mathie and C. N. Markides. Heat transfer augmentation in unsteady conjugate thermal systems – Part i: Semi-analytical 1-d framework. *International Journal of Heat and Mass Transfer*, 56:802–818, 2013.

[60] R. Mathie, H. Nakamura, and C. N. Markides. Heat transfer augmentation in unsteady conjugate thermal systems – Part 2: Applications. *International Journal of Heat and Mass Transfer*, 56:819–833, 2013.

[61] T. C. B. Smith. Personal communication.

[62] H. R. Wallingford and D. I. Barr. *Tables for the Calculation of Resistance in Internal Flows*. Thomas Telford Ltd, London, 1995.

[63] P. J. Linstrom and W. G. Mallard. Nist chemistry webbook, 2012. http://webbook.nist.gov.